Two new installations for non-destructive sample analysis: PIXE and PGAA

Inaugural-Dissertation
zur Erlangung des Doktorgrades
der Mathematisch-Naturwissenschaftlichen Fakultät
der Universität zu Köln

vorgelegt von

Petra Kudějová

aus Příbram,
Tschechische Republik

Köln 2005

Berichterstatter:

Prof. Dr. Jan Jolie
Prof. Dr. Jürgen Stutzki

Tag der mündlichen Prüfung:

12.7.2005

to Lidmila Langerová

Abstract

A new Proton Induced X-Ray Emission (PIXE) set-up has been designed and built at the Tandem Accelerator of the University of Cologne. The PIXE installation is used for the determination of elemental composition of thin samples or sample surfaces. The set-up was calibrated and tested with various types of samples. The experiments have been automated and the standard analogue based acquisition system has been replaced by a digital one based on the XIA DGF-4C modules. A small Peltier-cooled XFlash detector has been generally in use and brings many advantages when compared with common Si(Li) detectors. A scanning device can be used for macro-scanning of the surface of PIXE samples and the 2D elemental distribution can be determined. The absolute analysis of the sample composition with a commercial program GUPIX is described. Representative analysis of various samples is presented and compared to literature values or to the results of the PGAA method. The PIXE installation is now ready for routine use.

A new Prompt Gamma-Ray Activation Analysis (PGAA) facility is now being designed for the research reactor FRM-II in Garching by Munich. The PGAA instrument at FRM-II will use a beam of cold neutrons for the determination of the elemental and isotopic composition of a sample bulk. A number of Monte Carlo simulations were performed to obtain the most convenient beam guide geometry for the cold neutrons; first to keep the neutron flux as high as possible and also to find out, how to focus the neutrons to a small spot of $1 \times 1\,\mathrm{mm}^2$. The divergence of the neutron beam was also part of the study. The challenging task is to make the PGAA facility flexible for four different instrumental set-ups: standard PGAA, Position-Sensitive PGAA, Cold Neutron Tomography and an Ge Array for nuclear structure experiments. The expected parameters of the PGAA facility at FRM-II are then compared to the former one at Paul Scherrer Institute (PSI) in Switzerland. In close cooperation with the PGAA group at the Budapest Neutron Centre (BNC) in Budapest, interesting geological samples were measured and analyzed. Small amounts of samples ($100-300\,\mathrm{mg}$) were analyzed to demonstrate the reliability of the PGAA analysis even for such cases. The results of the analysis for geological standards and meteorites, both either as stones or as homogeneous powders are presented and discussed. PIXE and PGAA analysis for the same samples were performed, the results were compared and conclusions about when PIXE and PGAA are competitive and when complementary are given. In case of PGAA, comparison with Instrumental Neutron Activation Analysis (INAA) is also discussed.

Kurzzusammenfassung

Am Institut für Kernphysik der Universität zu Köln wurde eine neue Messapparatur für Protonen-induzierte Röntgen-Strahlung PIXE (Proton Induced X-Ray Emission) entwickelt und am Tandem-Beschleuniger des Instituts aufgebaut. Die PIXE-Messapparatur dient der Bestimmung der elementaren Zusammensetzung von dünnen Materialproben oder Oberflächen von Proben verschiedener Art. Zum Test der geeichten Messapparatur wurde zunächst eine große Anzahl verschiedener Proben ausgemessen und analysiert. Die Experimente wurden dabei weitestgehend automatisiert durchgeführt. Das bisherige Aufnahmesystem auf analoger Basis wurde durch ein digital basiertes System mit XIA DGF-4C Modulen ersetzt. In den Messungen wurde ein kleiner Peltiergekühlter XFlash Detektor eingesetzt, der gegenüber einem Si(Li)-Detektor mehrere Vorteile bietet. Zum Abtasten der Oberflächenstruktur der PIXE-Proben kann ein Scanner eingesetzt werden und die 2D-Elementar-Verteilung mit 1 mm Auflösung bestimmt werden. In dieser Arbeit wurde eine repräsentative Analyse für verschiedene Proben durchgeführt und mit Literatur-Werten und Ergebnissen der PGAA-Methode verglichen. Die PIXE-Messapparatur steht nun für einen regulären Einsatz zur Verfügung.

Am Forschungsreaktor FRM-II in Garching bei München wurde ein neues Messinstrument zur Prompten Gamma-Strahl Aktivierungsanalyse (PGAA) entwickelt. Ein Strahl von kalten Neutronen wird am PGAA-Messsystem des FRM-II zur Analyse der Elementar- und Isotopen-Zusammensetzung von ganzen Proben-Volumen eingesetzt. Um eine optimale Geometrie für den Neutronenleiter zu ermitteln, wurde eine große Anzahl von Monte-Carlo-Simulationen durchgeführt. Dabei soll einerseits der Neutronenfluss so hoch wie möglich gehalten werden, andererseits sollen die Neutronen auf eine schmale Fläche von $1 \times 1\,\mathrm{mm}^2$ fokussiert werden können. Ein weiterer Bestandteil dieser Arbeit ist die Analyse der Divergenz des Neutronenstrahls. Eine sehr anspruchsvolle Aufgabe ist es dabei, das PGAA-Messsystem für vier verschiedene Messaufbauten flexibel einzusetzen: Das Standard-PGAA, das Positions-Sensitive PGAA, die Kalt-Neutronen Tomographie und ein Ge-Array für Experimente zur Kernstruktur. Die erwarteten Parameter für das PGAA-Messsystem am FRM-II wurden mit denen des Paul Scherrer Instituts (PSI) in der Schweiz verglichen. In enger Zusammenarbeit mit der PGAA-Gruppe am Budapest Neutron Centre (BNC) in Ungarn wurden mehrere geologische Proben ausgemessen und analysiert. Dabei wurden nur sehr geringe Mengen der Proben gemessen ($100-300\,\mathrm{mg}$), um die selbst in diesem Fall hohe Leistungsfähigkeit einer zuverlässigen Analyse der

PGAA-Methode zu demonstrieren. Die Ergebnisse von geologischen Standard-Proben und von Meteoriten – in Form von Steinen oder als homogenes Pulver – werden in dieser Arbeit beschrieben und diskutiert. Dabei wurden jeweils PIXE- und PGAA-Analysen für eine Auswahl gleicher Proben durchgeführt und die entsprechenden Ergebnisse miteinander verglichen. Rückschlüsse, in welchen Fällen die beiden Messmethoden in direkter Konkurrenz zueinander stehen oder sich gegenseitig ergänzen, wurden gezogen. Des Weiteren wurde die PGAA-Methode mit der Instrumentalen Neutronen Aktivierungsanalyse (INAA) verglichen und diskutiert.

Contents

List of Abbreviations

AMS	Atomic Mass Spectrometry
BNC	Budapest Neutron Centre, Hungary
BNCT	Boron Neutron Capture Therapy
BNCS	Boron Neutron Capture Synovectomy
ERDA	Elastic Recoil Detection Analysis
FC	Faraday Cup
FRM-II	research reactor II (Forschungsreaktor II) in Garching by Munich
HPGe	High Purity Germanium detector
IAEA	International Atomic Energy Agency
IBA	Ion Beam Analysis
ICP-MS	Inductively Coupled Plasma – Mass Spectrometry
ICP-OES	Inductively Coupled Plasma – Optical Emission Spectroscopy
IKP	Nuclear Physics Institute (Institut für Kernphysik) of the University of Cologne
IFNAA	Instrumental Fast Neutron Activation Analysis
INAA	Instrumental Neutron Activation Analysis
IPAA	Instrumental Photon Activation Analysis
LOD	Limit of detection
LOQ	Limit of quantification
NAA	Neutron Activation Analysis
NIST	National Institute of Standards and Technology
NL-hall	Neutron-guide hall (Neutronenleiterhalle) at the FRM-II
PGAA	Prompt Gamma-Ray Activation Analysis
PGAI	Prompt Gamma-Ray Activation Imaging
PS-PGAA	Position-Sensitive Prompt Gamma-Ray Activation Analysis
PIGE	Proton Induced Gamma-Ray Emission
PIXE	Proton Induced X-Ray Emission
PSI	Paul Scherrer Institute, Switzerland
Si(Li)	Lithium Drifted Silicon Detector
SRM	Standard Reference Materials
RBS	Rutherford Back Scattering
RNAA	Radiochemical Neutron Activation Analysis
XRF	X-Ray Fluorescence

Chapter 1

Introduction

A thorough elemental analysis of a sample is required in many diverse research fields including e.g. archeology, medicine, biology, geochemistry, material research and engineering, cosmochemistry, ecology and many more. Majority of *chemical methods* use dissolution or ashing of the sample material and thereby they are *destructive*. In particular cases it is essential to preserve the sample during exploration and then a *non-destructive* analysis is required. Many *nuclear methods* – using an interaction of a charged or a neutral particle with the sample – offer a non-destructive analysis, such as Instrumental Neutron Activation Analysis (INAA), Particle Induced X-ray Emission (PIXE) or Rutherford Back-Scattering (RBS). In this thesis, I will go into detail with two of the non-destructive nuclear methods: Prompt Gamma-Ray Activation Analysis (PGAA) and Particle Induced X-ray Emission (PIXE).

PGAA and PIXE are rather distinct from each other: while a cold neutron beam (with an average neutron energy of about 5 meV) has been used for the PGAA measurement, a proton beam of 2.5 MeV was chosen for our PIXE instrument at the Tandem Accelerator of the University of Cologne. Two different non-destructive analytical methods bring the benefit of having complementary results of the elemental composition of an identical sample. Since the neutrons of the PGAA method interact with the nucleus of the target elements, PGAA can distinguish between isotopes, while protons of the PIXE method interact with the atomic shells to create the characteristics X-rays and therefore PIXE technique is generally not able to see differences among isotopes. Since protons of 2.5 MeV penetrate only tens of μm into the material, PIXE is convenient for an analysis of the sample surfaces or of very thin layers (e.g. aerosols on a membrane for air pollution determination). On the contrary, cold neutrons can pass through a bulk object without great loss of the flux intensity (depending on the object composition). In case of a homogeneous sample with a flat surface, both methods must lead to the same results of the elemental composition of given sample – which verifies the reliability of used instruments and methods (this will be also one of the tasks of this thesis). Or, in case of different results, it gives an important information about different composition of the sample surface and bulk (e.g. enamel on archaeological objects, weathering processes in geology). Both PIXE and PGAA are analytical methods with overall limits of detection up to μg/g, that means they are convenient for a major, minor and trace element analysis. However, it must be noted, that the sensitivity of the PIXE technique is in the range of ng, because during irradiation by the proton beam, only very small amount of the sample (usually units of mg) is analyzed. Generally, for an ultra-trace analysis (ng/g and less), either INAA or mainly destructive methods like Induced Coupled Plasma - Mass Spectrometry (ICP-MS) are used.

1.1 Proton Induced X-Ray Emission

So far, Particle Induced X-Ray Emission (PIXE) belongs among the most used methods for a surface analysis. In fact, mostly proton beams with energy between 2 MeV and 4 MeV are used to hit the target, so the "PIXE" abbreviation can be also understood as Proton Induced X-Ray Emission.

At the end of the year 2000, it was decided to build a PIXE instrument at the 10 MV Tandem Accelerator of the University of Cologne, Germany. The PIXE chamber was carefully designed with the intention to add other non-destructive analytical techniques there later, like Rutherford Back Scattering (RBS), Proton Induced Gamma-Ray Emission (PIGE) or Forward Scattering analysis. The new PIXE beam line was assembled during the year 2001 and already in December 2001 we had the first and successful PIXE measurement on a testing material. Due to the high demand of beam time at the Tandem accelerator by other groups, the available beam time for PIXE experiments was rather scarce. During the years 2002 and 2003, many principal modifications were carried out:

- the data acquisition was changed from analogue to digital electronic system
- the PIXE instrument was thoroughly calibrated with a set of thin MicroMatter standards
- a scanning of the sample on the area of about 3 cm x 3 cm was put into operation
- the measurement was automated for 24 small-sized samples
- an absolute analysis of both thin and thick samples was made possible thanks to a commercially available program called GUPIX (Campbell et al., 2004)

In the middle of the year 2004, the charging belt of the Tandem Accelerator was removed and replaced by a Pelletron charging system. This modification of the accelerator operation resulted also as a major improvement for the PIXE measurement: The ion beams of lower energy have become very stable in intensity and space, what is a required condition for a reliable proton beam normalization and for scanning of the sample surface with satisfactory resolution. In the chapter 2, I will describe in detail the PIXE instrument of the Nuclear Physics Institute (IKP) of the University of Cologne, the detection system and the data acquisition with digital electronics, the system calibration and the data analysis. I will present some representative results of PIXE experiments with both thin and thick samples and of a scanning of the sample surface. The results of a standard reference material (with known composition) will be then compared with nominal values and with the results of the PGAA method described later in chapter 3.

1.2 Prompt Gamma-Ray Activation Analysis

Prompt Gamma-Ray Activation Analysis is a relatively young nuclear technique for the analysis of the sample bulk. PGAA uses the capture reaction of thermal or cold neutrons by the elements of the target material. For this thesis, PGAA experiments were performed at the cold neutron beam of the Swiss Spallation Source at the Paul Scherrer Institute (PSI), Switzerland during the years 2000 – 2001 and later with the cold neutron beam of the research reactor at the Budapest Neutron Centre (2003 and 2004). The PGAA instrument from PSI has been moved to the research reactor II (FRM-II) in Garching by Munich, Germany and now lots of effort is dedicated to its new design for an operation at FRM-II already at the beginning of 2006.

In chapter 3, I will explain the principle of the PGAA method and I will discuss some important effects and corrections for a reliable sample analysis. To show the strong and weak points of PGAA, I will compare PGAA with the closest analytical method – Instrumental Neutron Activation Analysis (INAA), which is also a well-established and most applied non-destructive technique for a sample bulk analysis. I will present some of our comparative results of standard reference materials and meteorites and compare them with the results of the new PIXE instrument at IKP, Cologne. Then, I will describe more in detail the new design of the PGAA instrument at the FRM-II, discuss our plans and expectations. Our endeavor is to assemble a flexible PGAA instrument with world-best limits of detection (for all measurable elements) in comparison to other PGAA facilities. Our interest is mainly concentrated to the most sensitive non-destructive analysis of boron.

1.3 Limits of non-destructive analysis

What to understand under the term *non-destructive*? Very simply said, if the people get the sample back after the analysis and there are no “visible” changes of it then the method is considered as non-destructive. Such a sample can be remeasured and the obtained results must agree with the previous one.

In another words, if the sample after the measurement is not damaged by the impinging radiation, delivered heat, charge build-up, by vacuum conditions and other effects, the measurement can be considered as non-destructive. So, the non-destructivity of the method depends inevitably on the sample characteristics, too. This is delicate mainly with charged particle beams in vacuum. Taking our PIXE as an example, the stopping range for 2.5 MeV protons is several tens of μm, the kinetic energy of the protons is transformed into heat in this thin layer and the proton charge (proton current of about 10 nA) is accumulating here as well. Therefore, electrically conducting samples (or samples with a conducting layer on the surface) will avoid the charge build-up and more, they will better conduct the heat and help to dissipate it. Insulating samples will, sooner or later, show burned spots at the position of the proton beam impact. To avoid this, usually a thin carbon[1] layer is evaporated on a surface of insulating samples. Or, the proton beam is swept over the sample surface to avoid creation of the burned spot. With biological samples even more attention is needed: e.g. dried tree fungus shows no visible damage directly after the irradiation. The spots burned by the proton beam will slowly appear within few weeks (Král, 2004).

The measurement with cold neutrons passing through the sample object can be stated as non-destructive in majority of the cases. Neutrons do not deliver any charge and they do not heat the sample (on the contrary, they are being 'warmed up' by the interaction with a sample of a room temperature!). I have experience with only one example, when PGAA is destructive for the sample: it is a case of meteorites, in which the exact isotopic ratio between elements is important for the basic research of the solar system (Englert et al., 1986). This ratio (which can differ from the ratios of terrestrial samples) could be notably altered after longer irradiation by neutrons.

When using a surface analysis, e.g. PIXE, the sample has to be often carefully prepared for the measurement: the surface must be cleaned, flattened or smoothed, a conductive carbon layer might be needed. Sometimes, the samples are powdered to have homogeneous mixture for the analysis. In case of a large object like a statue (e.g. to determine, if the hand of the statue is as old as the statue body) the measurement would be really challenging[2]. Then, a small piece of it is carefully cut and brought for a detailed analysis. This piece can be then returned to the original place, however, into some extent some damage of the object was made in order to make the analysis.

A conclusion of what is *non-destructive* in the language of experimental physicists: It is a (nuclear) method, that does not create any considerable damage to a sample caused by irradiation. It says nothing about the qualities of the irradiated sample itself, except, that after the irradiation the sample will be unchanged (though it might be activated).

1.4 Aim of this thesis

In this thesis, the new PIXE instrument of the IKP and the analysis of the acquired PIXE data will be described in detail in chapter 2. The results that outline some important features of the new PIXE instrument will be included (comparison of data analysis with reference values, analysis of a scanned sample, ...). The PIXE part of the thesis is written with the aim to make the PIXE set-up familiar for successors to overcome easier the first, introductory phase with the instrument, data acquisition

---

[1] Carbon is used for its characteristics lines are not visible in the PIXE spectra

[2] There are many small portable PIXE and RBS systems with a radioactive source employed. They are used for an analysis of large valuable objects in-situ, however, the analysis is never as sensitive and fast as PIXE or RBS using accelerators, see e.g. (Pappalardo et al., 2003).

and data analysis.

In chapter 3, the main task is to introduce a new PGAA instrument at the FRM-II research reactor. Because the PGAA instrument – at the time of writing this thesis – is not yet built at FRM-II, simulations, expectations and proposed design of the new instrument will be presented. The simulations are partially based on real parameters gained already from the operating FRM-II reactor and the expectations result also from 4 years experience, when basically the same PGAA instrument was successfully operating at PSI, Switzerland. Since the last experiment at PSI ran in November 2001, we have got very nice opportunity to stay in contact with a PGAA instrument and I have performed some experiments with the PGAA group at BNC, Budapest. As in case of PIXE, I will include interesting results stating some important features about the new PGAA instrument at FRM-II and about PGAA technique itself.

Chapter
2

PIXE

The PIXE technique belongs – together with the already mentioned Rutherford Backscattering (RBS) and Proton Induced Gamma-Ray Emission (PIGE) or Nuclear Reaction Analysis (NRA), Elastic Recoil Detection Analysis (ERDA) and other similar techniques – to a group of experiments using accelerated ion beams, generally called Ion Beam Analysis techniques (IBA). For PIXE, mostly proton beams of energy between 2 – 4 MeV are employed.

PIXE is an analytical method based on the X-ray spectrometry determining elemental composition of the sample surface. More precisely said, it is an analytical method of a thin surface layer of the sample, usually of several tens of μm because the protons of energies used for PIXE are stopped by the interaction with the sample material within this range and the evoked weak X-rays are also strongly attenuated.

PIXE can be used for an absolute analysis and is able to detect an amount less than ng of elements in irradiated samples. PIXE is a technique, which detects all elements between Na and U according to the correspondent characteristic X-rays and their intensity acquired during the sample irradiation by an accelerated proton beam. The resulting acquired data with the PIXE technique – which have adequate statistics and for common samples – can be obtained in order of 10 minutes, the analysis can be finished within one or a few hours – the PIXE method is prompt when compared to chemical methods or Neutron Activation Analysis.

PIXE is categorized to nuclear techniques although the required interaction does not include the target nucleus, but the electron shell of the target atom. On the contrary, nuclear reactions are undesirable because they cause higher background spectra and (p,n) reactions, whereby the emitted neutrons can cause damage to the thin silicon crystal of the PIXE detectors. However, since we are using accelerated proton beams, PIXE can be classified as a nuclear method, too. The PIXE technique was introduced at the Lund Institute of Technology by Johansson et al. (1970b) in 1970, where on the first occasion a proton beam was involved together with a Lithium-drifted Silicon Si(Li) detector.

A comprehensive description of PIXE technique is covered by two books dedicated only to PIXE (Johansson et al., 1970a; Johansson and Campbell, 1988) and well summarized details in a book dedicated to non-destructive elemental analysis (Alfassi, 2001).

During the years 2001 – 2004, the PIXE instrument of the IKP was designed as well as developed and then mounted at the L30 beam line at the Tandem Accelerator of our institute. Then we have been testing it with various sets of experimental parameters, configurations and samples. Because radiation protection does not permit to enter the experimental hall during the experiments with a proton beam, it led us to automatize the experiments as much as possible.

In the first section of the PIXE chapter, the necessary minimal theoretical background will be explained on the example of a thin sample and subsequently extended for thick samples as well as discussed for samples with an intermediate thickness. The next section will describe the PIXE instrument in detail. We will follow the PIXE technique from the source of the proton beam, through the detection of characteristics X-rays by the XFlash detector, up to the analysis of the acquired spectra by digital electronics and subsequent determination of the concentration for all detected elements. For that part, a commercial program for a sample analysis GUPIX and its functionality will be introduced. In the following section, results and discussion are presented. Finally, conclusions for the PIXE method at the IKP will be summarized.

2.1 Principles of PIXE analysis

The protons are accelerated to the requested energy, they hit the target and interact with the electron shells of the atoms in the target material. With some probability inner-shell electrons are ejected. By this inelastic proton scattering, the K-shell electrons will be ejected with the highest probability in comparison to other e^--shells, then follow L-shell, M-shell electrons and then others. By filling the arisen vacancies by outer-shell electrons to minimize the energy of the atom, either characteristic X-ray is emitted or concurrent process of emitting Auger electron takes place. Both concurrent processes are sketched in Figure 2.1.

When filling the K-shell vacancy, the emitted X-rays are called K X-rays , for L-shell vacancy, they are L X-rays. While by the detection of characteristic X-rays lines, the elements are identified, by the analysis of their intensity, the concentration of the elements in specimen is determined. Similarly, the lines in the detected spectrum of X-rays are called K-,L-, or M-lines of particular element.

Elements detected by PIXE The characteristics K-lines have energies in interval from 0.05 keV for Li up to more than 100 keV for U. The Lithium-drifted Silicon detectors Si(Li) employed for a typical PIXE experiment, are able to detect elements starting from Sodium to the end of the Periodic Table, e.g. to Uranium. The typical Si(Li) detects only energies between 1 keV and 40 keV – having an intrinsic efficiency close to one between 4 and 15 keV – therefore L-lines are employed for the detection of heavier elements: the Lα-line of Uranium is 13.61 keV only, while its Kα-line has energy of already 98.43 keV. The energy resolution of a Si(Li) detector varies between 135 eV and 180 eV. The minimum detectable energy/element of a Si(Li) detector depends on the protection window, consisting usually from Beryllium and absorbing foils in front of the detector, which restrains damage of the Silicon crystal by scattered

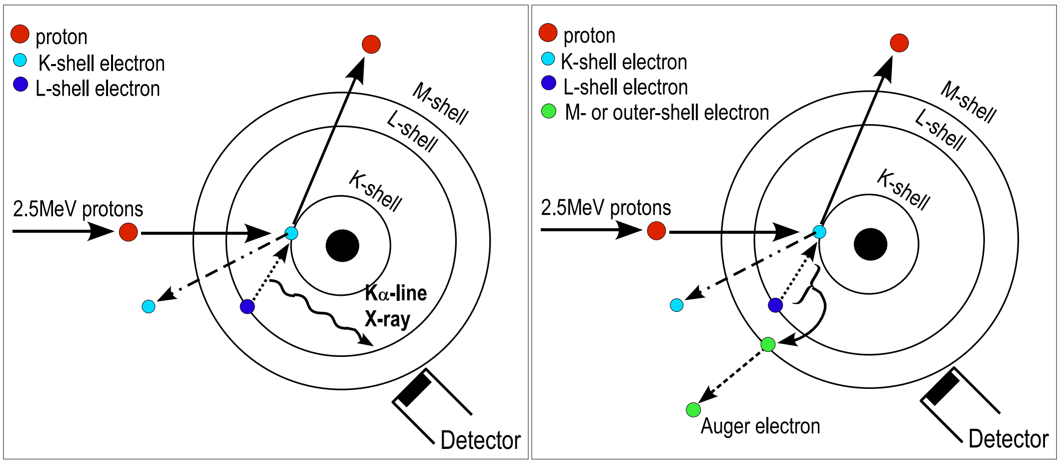

Figure 2.1: Schematic drawing of competitive processes of proton interaction with electron shell of a target atom producing either characteristic X-ray or Auger electron is emitted.

protons. These protecting foils also constrain the transmission of X-rays with very low energy (see Table 2.2).

Theoretical minimum For a successful determination of a concentration C_z of a given element Z in a measured sample, the characteristics and geometry of the given PIXE system, the energy of the proton beam and its interaction with the sample are required, which is calling for good knowledge of many parameters.

Two extreme cases of samples turn to be simple for the PIXE analysis: 1) very thin specimen, when we suppose that the proton beam travels through the sample without any appreciable loss of energy and intensity; 2) very thick sample that stops the proton beam entirely in its volume. We will discuss both cases and explain the required parameters. Lets take for simplicity *a thin sample* first.

2.1.1 Thin sample

When determining the relation between the yield Y_Z of characteristic K_α-line (or L_α-line) and the element mass m_Z in the sample we suppose to have a homogeneous proton beam with energy E_0 and a homogeneous thin and flat sample, which lets the full proton beam pass through without any loose in intensity and energy. If the sample is smaller than the proton beam dimension, the surface S of the sample is considered, if the proton beam is smaller than the sample dimensions, the proton beam surface S is considered for the calculations. Then we can write (Johansson and Campbell, 1988):

$$Y_Z(E_0) = \frac{N_p m_Z N_A}{S M_Z} \cdot \sigma_Z(E_0) \omega_Z b_Z^\alpha \epsilon_Z \tag{2.1}$$

Here N_p is the number of impinging protons on the surface S, N_A is Avogadro number and M_Z is the atomic mass of the element Z, $\sigma_Z(E_0)$ is the ionization cross-section of the atom Z by protons with energy E_0, ω_Z is the fluorescence yield for K- or L- line, b_Z^α is the branching ratio and gives the fraction of the K- or L- X-rays, which appear in only K_α or only in L_α line, ϵ_Z is the total detector efficiency at the particular K- or L- X-ray energy of the element Z.

The N_p can be easily determined by registration of the proton charge passing through the target to e.g. Faraday Cup or by some other means. The surface of the beam or of the sample is also known. The ionization cross-section $\sigma_Z(E_0)$ is tabularized, its behavior can be described so, that it increases with the proton energy E_0, decreases with the proton number of the element Z in the sample, it is highest for K-lines and lower for L-, then for M- lines … The graphical illustration of the $\sigma_Z(E_0)$ can be found e.g. in (Johansson and Campbell, 1988), in Figure 2.1, page 26.

The fluorescence yield ω_Z gives the probability of the decay of a given ionized state (K- L- M- shell vacancy) by emission of X-rays to the probability of Auger electron emission instead. The values are also tabularized as well as the branching ratio values b_Z^α.

The absolute detector efficiency ϵ_Z includes the intrinsic detector efficiency ϵ, which is usually close to one between 5 keV and 15 keV (for the XFlash detector it is between 5 keV and 11 keV – see Figure 2.9 of the XFlash detector intrinsic efficiency) and solid angle Ω of the detector crystal looking at the target.

If we want to calculate the detected intensity of particular X-ray peak with energy E_X of element Z expressed by a net area A_Z, we can use the equation (2.1) and write:

$$A_Z = N_p\ c_Z \sigma_Z(E_0) \omega_Z\ b_Z^\alpha \epsilon_Z \Omega T_{E_X} \tag{2.2}$$

where we use the concentration of the element c_Z:

$$c_Z = \frac{m_Z N_A}{S M_Z}$$

(in units: atoms/cm^2) and where Ω is the detector front face solid angle how the detector sees the target (in sr) and T_{E_X} is the transmission of the detected X-ray with particular energy E_X through all the absorbing foils and filters between the target and detector crystal. All other parameters have the same meaning as explained in relation (2.1). The detection limits for thin sample can generally reach 1 ng/cm^2. Some problems with the analysis can arise, if the thin sample is not ideally flat, what can alter the elemental concentration of few percent. This difficulty is connected with the short projected range of protons of few tens of μm (see Table 2.1) and therefore the sample surface with few μm thick roughness or grains can cause scattering of emitted X-rays out of their straight way to the detector window and change their intensity this way (Král, 2004).

2.1.2 Thick sample

A thick sample is any sample with thickness larger than is the projected range of protons with energy E_0 in the sample. For the 2.5 MeV protons we use, the Table 2.1 and Table 2.2 lists the length of the proton longitudinal path in different elements, compounds and materials according to SRIM calculations (Ziegler, 2004). In Table 2.2, there are included also absorber foil materials usually chosen to protect the detector before scattered protons. In our case, a Makrofol foil of 110 μm thickness is applied to stop all protons from entering the detector crystal. The tables show, that any solid material investigated by PIXE and thicker than 0.5 mm is already a thick sample.

For the relation between the intensity, or the net area A_Z of the characteristic X-ray line and the element concentration c_Z in the homogeneous thick sample of interest, again assuming a homogeneous proton beam with energy E_0, the formula (2.2) can be used with small changes and with a little different meaning of used parameters:

$$A_Z = N_p \, c_Z \omega_Z \, b_Z^{\alpha} \epsilon_Z \Omega \int_{E_0}^{0} \frac{\sigma_Z(E) T_{E_X}(E)}{S(E)} dE \tag{2.3}$$

where $\sigma_Z(E)$ is now dependent on the energy of the proton which is stopping in the target matrix, $S(E)$ is the stopping power of the target matrix and it is a function of the matrix composition. Since the X-rays are now attenuated in the sample itself, one contribution to the general transmission of the X-rays $T_{E_X}(E)$ is now the self-absorption of the X-rays in the sample itself. This part of $T_{E_X}(E)$ is now dependent on the depth, which were the protons with energy E_0 able to penetrate into the sample, therefore dependent on the stopping power $S(E)$ of the matrix, given by its composition. $T_{E_X}(E)$ is also function of the incident and exit angles of the proton and X-ray, (see description by Johansson and Campbell (1988), chapter 6). The detection limits in case of thick sample can generally go down to 1 μg/g. For thick samples, sometimes a relative method employing one element of the target as an internal standard is chosen for a reliable analysis. This approach is similar to the k_0 method employed so successfully by the PGAA analysis and described in the next chapter of this thesis (see 3.2.4).

Röntgen fluorescence The thick sample analysis is more difficult than the case of thin sample. It is caused not only by the parameters dependent on the energy of protons, which are slowing down in the sample. Also the emitted X-rays, when traveling out of the sample, can cause secondary X-ray fluorescence (so-called Röntgen fluorescence) of X-rays with lower energy then their own. This physical process can of course drastically change the yields and concentrations for different elements, depending on the particular target matrix. Thus, in precise programs for a sample analysis, also an iterative approach for the determination of factors, which evaluate the probability of creation of secondary X-rays fluorescence is involved.

Z	Element	density $[\mathrm{g \cdot cm^{-3}}]$	Projected Range $[\mu\mathrm{m}]$	Z	Element	density $[\mathrm{g \cdot cm^{-3}}]$	Projected Range $[\mu\mathrm{m}]$
13	Al	2.70	59.64	30	Zn	7.14	32.49
14	Si	2.32	68.32	34	Se	4.81	52.38
19	K	0.86	190.33	38	Sr	2.60	96.44
20	Ca	1.54	106.77	42	Mo	10.21	26.18
22	Ti	4.52	43.33	48	Cd	8.64	32.73
25	Mn	7.43	27.87	56	Ba	3.51	85.85
26	Fe	7.87	26.16	73	Ta	16.60	23.06
29	Cu	8.92	25.79	82	Pb	11.34	34.75

Table 2.1: Projected range of 2.5 MeV protons in different elements

Material	Elemental Composition	Material density $[\mathrm{g \cdot cm^{-3}}]$	Projected Range $[\mu\mathrm{m}]$
Water	H_2O	1.0	210.32
Salt-crystal	NaCl	2.17	113.62
Makrofol	$H_{14}C_{16}O_3$	1.20	94.72
Mylar	$H_8C_{10}O_4$	1.40	84.80
Kapton	$H_{10}C_{22}N_2O_5$	1.43	84.08
Marlex	H_4C_2	0.93	104.47
Air	N-75.5%, O-23.2%, Ar-1.3%	0.00125	103 700
Bronze	Cu-89%, Zn-9%, Pb-2%	8.82	26.79
Glass	O-59%, Si-24%, Pb-5%, Na-7%, K-4%	4.8	89.85

Table 2.2: Projected range of 2.5 MeV protons in diverse common compounds and absorber materials, which are used for protecting the detector crystal from protons scattered on the target. We apply a 110 μm thick Makrofol foil.

Charging of the thick sample Since the proton beam in entirely stopped in the thick sample surface, its entire charge is also deposited to the specimen. The PIXE measurement takes place in high vacuum and if the specimen is not conductive, the charge build-up will discharge by creating discharge, which attracts electrons from its surrounding, those create strong bremsstrahlung and this results in higher continuous background of the PIXE spectrum (see section 2.3.2). The consequence is then a generally lower sensitivity and detection limits for the determination of the sample composition. A solution is to cover the insulating sample by a thin conductive Carbon layer[1] or placing a hot-wire element close to the sample. The hot-wire element liberates electrons and compensates already weekly positively charged sample. Another solution of discharging the thick insulating sample is to put a thin carbon or metal foil to about 1-2 cm in front of the sample, because the protons passing through the foil strip electrons with them to the sample. This set-up can be additionally used for normalization of the proton charge impinging a thick specimen, which is also not a trivial task. In case of the carbon foil in front of the specimen, protons back-scattered can be registered by a surface barrier detector and normalized to the proton charge impinging the sample. Another way how to get rid of the specimen charging is possible, if the measurement proceed either in atmosphere (air) or in gases (N_2 or He) with pressure of units of Pa, which is sufficient to compensate already weekly charged specimen and hinder the creation of discharge.

Sample with intermediate thickness This is the most difficult case of a PIXE analysis, because many parameters, which are not always easy to determine, like sample matrix, density and thickness, proton intensity and energy spectrum when leaving the sample should be known. For the relation between the net peak area A_Z and concentration of given element c_Z in the sample, the formula (2.3) for thick sample can be used, assuming we integrate now over the proton beam energy from E_0 to E_p, what is the energy of the proton beam leaving the sample.

2.2 PIXE Instrument at IKP

To make a PIXE analysis of a sample, following chain of equipment is involved in case of the Nuclear Physics Institute (IKP) of the University of Cologne: Sputter source for protons (TiH_x), 10 MV Tandem Accelerator accelerating the proton beam to required energy (2.5 MeV), evacuated beam guide with elements focusing and bending the proton beam, measuring chamber for the samples, detectors of the characteristics X-rays, monitors of the proton current (or charge), digital electronics processing the signal from the X-ray detectors and a good acquisition software followed by a reliable program for the data analysis. For the detection of X-rays, mainly a small Peltier-cooled XFlash detector is used and it brings the advantage of its capability to acquire

---

[1] The advantage of carbon consist in its conductivity on one side and having its K_α-line energy of 0.28 keV on the other. Therefore, carbon X-rays are invisible for the PIXE detectors and they are not contributing to the PIXE spectrum in contrast to other conducting materials.

Figure 2.2: 10 MV Tandem Accelerator of the Nuclear Physics Institute (IKP) of the University of Cologne.

up to 300 kcps. The data acquisition is performed by digital electronics with a system based on DGF-4C modules from X-ray Instrumentation Associates (XIA, 2004) and with an in-house developed acquisition software (Materna, 2001). For the analysis of the spectra, the GUPIX program is used. The calibration of our PIXE instrument was first performed with thin MicroMatter standards and then homogeneous powders of Standard Reference Materials (SRM) were measured to check the reliability of the sample analysis.

2.2.1 Tandem Accelerator

The PIXE experiments are performed at the 10 MV Tandem Accelerator. An overview description of diverse experiments – dedicated mainly to nuclear structure studies, like excited level schemes, short life-time measurements, high spin measurements or nuclear reaction mechanisms – can be found in a detailed laboratory portrait of the Institute of Nuclear Physics of the University of Cologne published by Jolie et al. (2002). Until June 2004, the Tandem Accelerator had been using a conventional charging belt. Since the Tandem Accelerator is well-equipped for fine-tuning of ion beams of higher energy, the 2.5 MeV proton beam was actually at the lower limit of the terminal voltage (1.75 MV) possible to be hold by the accelerator – and therefore less controllable. This condition led to usually not very stable intensity of the proton beam, which was even oscillating in space of about (± 1 or 2 mm^2). Small Van de

Graaff accelerators dedicated to PIXE and other IBA methods (usually accelerators able to accelerate protons up to 4-5 MeV) produce much more stable beams and they are better controllable at lower energy range of accelerated ions. The intensity of the beam has sometimes changed so considerably, that in fact the measured count rate by the detector was an averaged one consisting of batch of very high count rates and very low count rates (like pulsing). This has caused the resolution of the detector to seem much worse than it would be in case of an ideal stable averaged count rate. In spite of the oscillations and instability of our proton beam intensity we were able to focus the proton beam to about $1 \times 1.5\,\mathrm{mm}^2$ with the help of a well aligned set of focusing elements. Beam focus of few mm^2 is also standard by small Van de Graaff accelerators and so it was very satisfactory for us to get as good focus, too. To obtain a smaller beam focus on the target, the beam has to be cut by the slits in both vertical and horizontal directions to obtain e.g. less than $1 \times 1\,\mathrm{mm}^2$ area. The minimum beam area, which we have obtained by cutting the proton beam and by having still satisfactory intensity on the target (current of few nA) was about $0.2 \times 0.2\,\mathrm{mm}^2$. Therefore we knew that the intended macro-scanning of the samples would be possible, if we manage to stabilize the oscillations of the proton beam.

2.2.2 Pelletron Accelerator

The irregular oscillations of the proton beam have come to an end and the situation has greatly improved when the charging belt of the accelerator was replaced by a Pelletron charging chain made of metallic cylinders. The advantages of the Pelletron charging chain in comparison to a charging belt are well described at the web-page of the National Electrostatics Corporation (2004). To list the most important merits of Pelletron, we have to mention 1) the stability of the induced terminal voltage, 2) insensitivity of the charging chain to moisture, 3) no damage caused by sparks and friction to the charge carrier (instead of friction – charge induction is used), and therefore 4) no need to open the Tandem tank so often e.g. because of the dust coming from the belt rubbed by the contact-brush (only to open and close the Tandem tank is an operation taking at least 4 days when no experiments are possible). After this change to the Pelletron system in 2004, we are able to focus the beam to $1 \times 1.5\,\mathrm{mm}^2$ much easily. We are able to have a proton beam with the current intensity in interval between 0 - 100 nA at the target position and vary it promptly according to the sample character.

2.2.3 PIXE Beam-line

In this section, we intend to describe the L30 beam guide – one of the seven splitting beam guides after the 90° analyzing magnet. Schematic view of the experimental hall at IKP is displayed in Figure 2.4. This L30 beam guide is deflected to -30° in relation to the straight direction and is dedicated to applied physics.

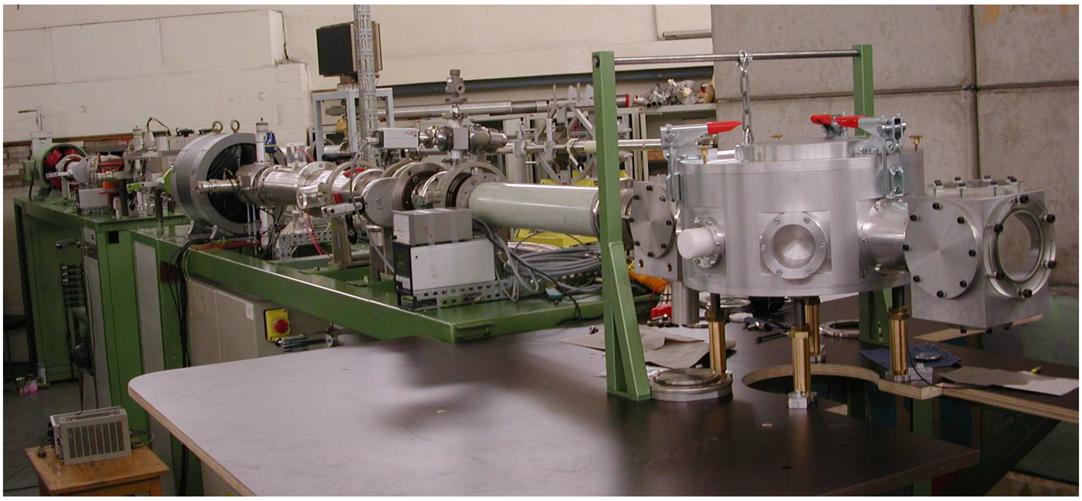

Figure 2.3: The PIXE beam guide before the first experiments.

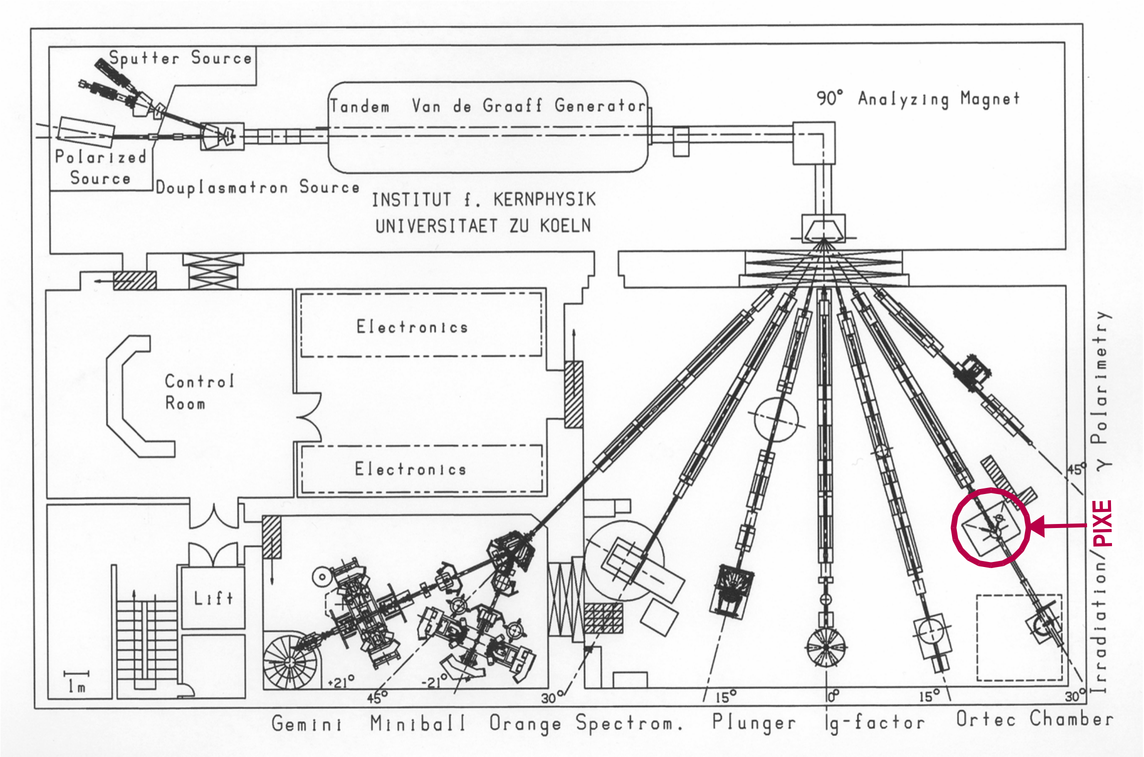

Figure 2.4: Schematic view of the experimental hall at the Tandem Accelerator at IKP. The PIXE beam guide L30 is deflected to $-30\,^\circ$ in relation to the straight direction and is dedicated to applied physics.

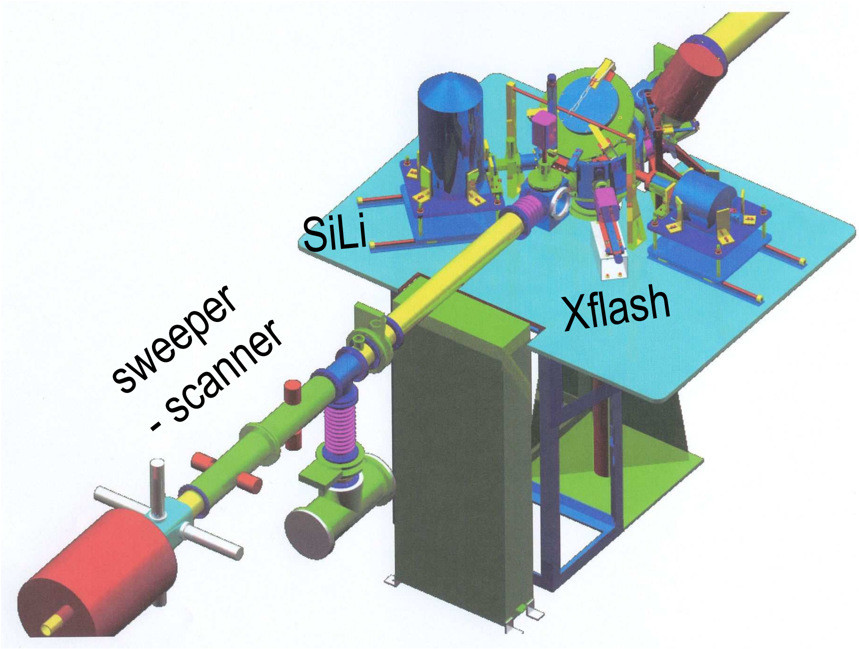

Figure 2.5: Schematic drawing of the PIXE beam guide including the third quadrupole focusing magnet, sweeper, small cube for collimation purposes and the PIXE chamber with many possible positions for the detectors. The PIXE chamber is intended not only for PIXE, but for more IBA applications, like PIGE, RBS or NRA

First part

The first part of the L30 consists in sequence of a main valve; quadrupole focusing magnet; turbomolecular pump; xy adjustable slits for cutting the beam; 3 cubes which can be used e.g. for normalization purposes; valve; quadrupole focusing magnet; xy adjustable slits; xy electrostatic sweeper; turbomolecular pump; closing valve. This part of the beam guide can be evacuated down to $8 \cdot 10^{-6}$ mbar.

Second part

The second part of the beam guide includes a cube used for normalization purposes and for collimation; the PIXE chamber and a cube for the Faraday Cup. This second part of the L30 is evacuated by one turbomolecular pump attached from downside to the chamber. After breaking the vacuum, it can be restored within 15 – 25 minutes. The chamber part is usually evacuated down to $2 \cdot 10^{-5}$ mbar, depending on the character of the samples and the air humidity. The start of the evacuation must proceed rather slowly (change of 0.1 bar/s) because of the very thin Beryllium windows of both the XFlash and Si(Li) detectors.

Sweeper or scanning device

The electrostatic sweeper was built in the beam guide about 2.5 m in front of the PIXE chamber and it can be used either for macroscanning with a beam focused to $1 \times 1\,\mathrm{mm}^2$ or to sweep the proton beam on a collimator placed 24 cm in front of the sample for normalization purposes. The sweeping frequency in the horizontal direction is 1 kHz, in the vertical direction it is 100 Hz. To shift the beam at the target position of 1 mm vertically, the corresponding change of the voltage on Y-condensators is 94 V. The change of 1 mm horizontally, the voltage on the X-condensators must be changed of 85 V. The maximum scanned as well as swept area at the target position is about $6 \times 6\,\mathrm{cm}^2$.

When we want to sweep the beam on a chosen area, the voltage on the X and Y condensators must be changed following way: First, when the sweeper is switched on, the position of the proton beam on the target gains a negative offset in vertical direction. The beam position must be corrected by a V_{off} controller by turning it to +350 V. Then we found a linear dependence between the voltage U on the sweeper X- and Y- condensators and the swept width x and y in mm on the target position :

$$x[mm] = 10 \cdot V_{Horizontal} + 1$$

$$y[mm] = 15 \cdot V_{Vertical} + 1$$

(to sweep $5 \times 5\,\mathrm{mm}^2$, we have to change the vertical controller to 267 V and horizontal controller to 400 V).

2.2.4 PIXE chamber

A 3D scheme of the PIXE chamber setup with some possible positions of the detectors is shown in Figure 2.6.

Chamber

The inner diameter of the chamber is 40 cm. The chamber has 6 symmetrical horizontal openings at 135 °, 90 ° and 45 ° to the proton beam direction. These entrance windows can be used for detectors of any IBA technique. The XFlash and Si(Li) detectors used for PIXE occupy both 135 ° windows during the experiments and they are dismounted after it. The Si(Li) detector can be exchanged with a HPGe detector for PIGE application and we can acquire both data for PIXE and PIGE at the same time[2]. A very nice description on PIGE written by Räisänen (2001) can be found in the book of "Non-destructive Elemental Analysis" edited by Alfassi (2001). Smaller detectors like Surface Barrier detector for RBS or a small video-camera can be mounted directly into the chamber. The chamber can be completely electrically isolated from

---

[2] Until now, we have employed a proton beam of 2.5 MeV energy to have consistent data for PIXE measurement. With a well shielded HPGe detector for PIGE situated at the same angle of 135 °, elements between Li (Z=3) and Cl (Z=17) can be determined by the same proton energy and the sample analysis by PIXE can be complemented by the PIGE results.

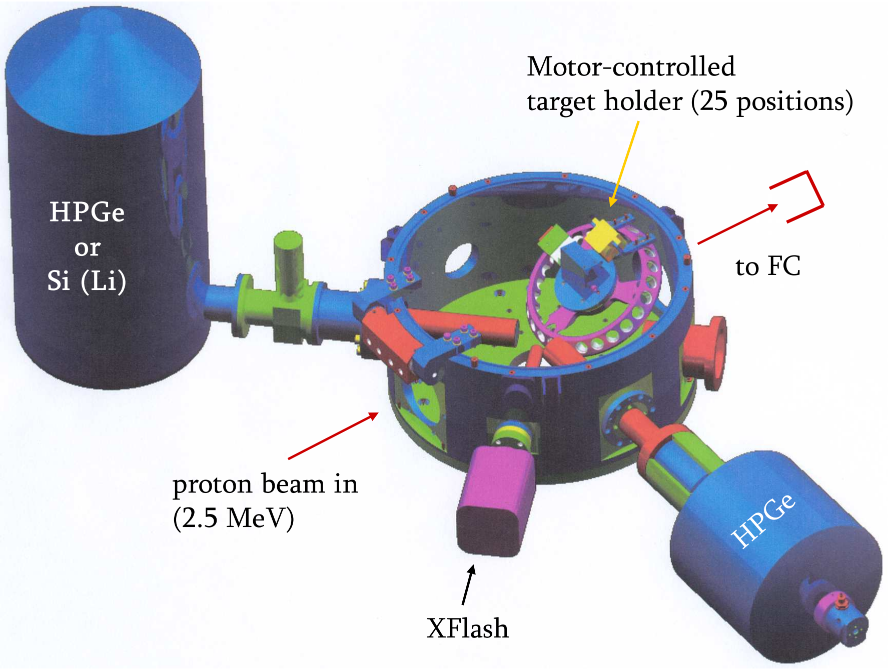

Figure 2.6: Schematic drawing of the PIXE chamber with the proton beam entering and leaving to Faraday Cup (FC). The XFlash detector and the Si(Li) detector are positioned at 135 ° to the proton beam direction. A HPGe detector can be used for the PIGE applications. The small samples are fixed on a wheel with 25 positions.

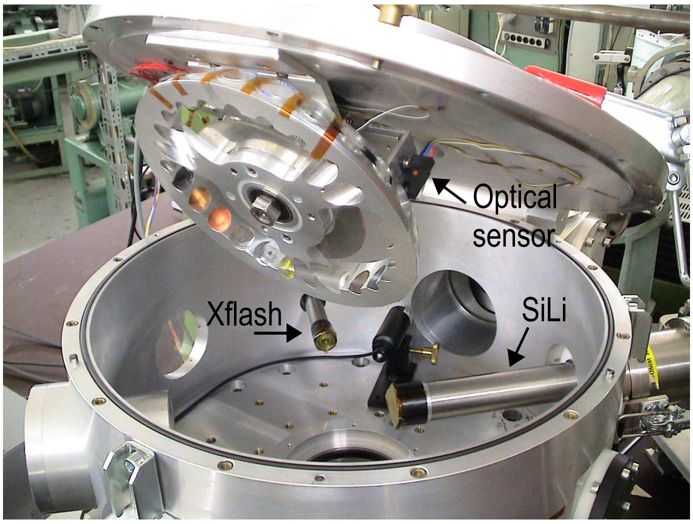

Figure 2.7: The wheel is driven by a small motor placed in the PIXE chamber and controlled remotely from a PC through a STP100 motor controller. The zero position of the wheel is set with the help of an optical sensor and a pin on the wheel which interrupts the optical signal. The movement of the wheel and the status of the sample is monitored by a small camera. On this picture, the XFlash detector with the Makrofol protecting foil is very far from the sample.

the surroundings and the charge can be collected for normalization purposes this way (see 2.3.4).

Wheel

The PIXE chamber is designed for an automatic analysis of a maximum of 24 samples within one run – the chamber does not have to be reopened before all of them are measured. The samples with a diameter not larger than 2 cm are mounted on a wheel driven remotely by an acquisition PC. The sample surface is perpendicular to the proton beam during irradiation. The correct position and a state of the sample are observed by a small camera. The wheel together with the driving motor is mounted to the chamber cover so that by opening the chamber, the wheel with samples is well accessible. The stepping motor with a smallest step of 0.9 ° is adapted to vacuum. The heat caused by its operation is dissipating through a contact with the Al cover of the chamber. The movement of the motor is controlled by the STP100 controller (PONTECH, 2001). The “zero position” of the wheel is set with an optical sensor, when a thin pin fixed to the wheel interrupts the optical signal, see Figure 2.7 for illustration. We align the middle of the target position by a theodolite fixed to a wall of the experimental hall.

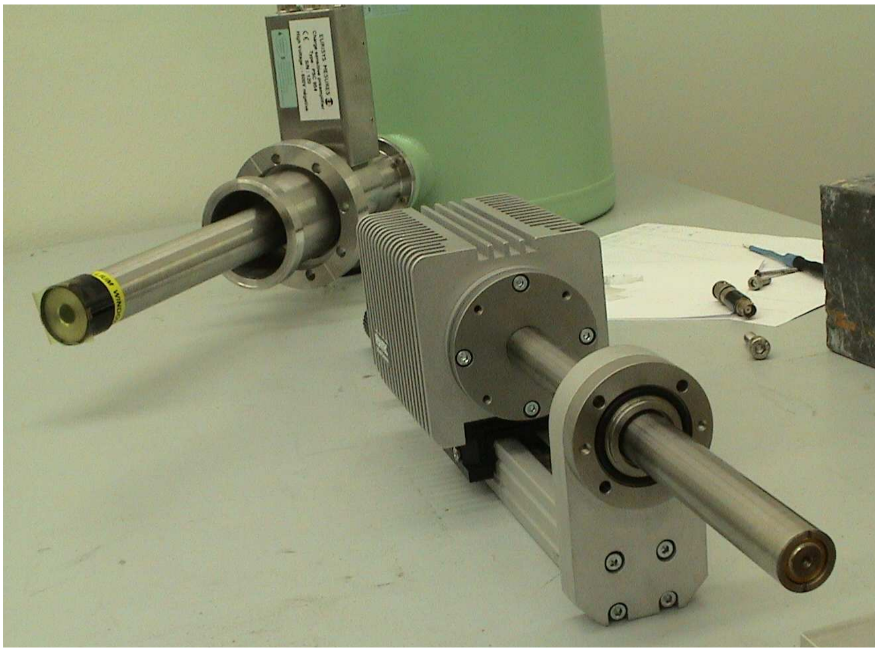

Figure 2.8: XFlash detector in front of the Si(Li) detector with a protecting Makrofol foil.

Visualization of the beam

The camera in the PIXE chamber is also used to view the size and shape of the proton beam during its focusing on the target position at the beginning of each PIXE experiment. It is convenient to check the beam size and shape also during the measurement. A scintillating YAG crystal is used for visualization of the proton beam (CRYTUR, 2005) and recently we have got also 2 quartz scintillators with a central hole of 1 mm and 3 mm in diameter to check at the same time the scintillations on the quartz crystal and the proton current on the Faraday Cup located ca. 18 cm behind the target. In spite of the fact that the scintillation of the quartz is much weaker than that of the YAG crystal, the true dimensions of the beam are better represented. The YAG crystal shows – due to the extremely high and good luminosity – also the halo effect of the beam and therefore larger beam dimensions are observed than they in reality are.

2.2.5 XFlash detector

For the majority of the PIXE tests and experiments we employ a small Peltier-cooled Silicon Drift Detector XFlash 2001 from the Röntec company (Röntec, 2001). The active surface area of the detector crystal is 10 mm^2 and its thickness is only 0.3 mm. The Silicon Drift Detector (SDD) differs considerably from a Si(Li) crystal: SDD is a chip with integrated on-chip electronics for a signal amplification and readout, well described at the web-page of Sampietro (2005) or by Lechner et al. (1996). Due to the unique characteristics of the SDD, the leakage current is minimized to typically $10\,\mathrm{pA} \cdot \mathrm{mm}^{-2}$ (Strüder et al., 1998; Sampietro, 2005) and the total thickness of the Silicon Drift Detector chip of $300\,\mu$m is sensitive to the absorption of ionizing radiation, that means, the SDD has no dead layer (Lechner et al., 1996). More details are summarized by Strüder et al. (1998). If we continue the comparison with a standard Si(Li) detector for X-rays measurement, we can find the following advantages: the XFlash detector is really compact, light and handy. Its working temperature is $-16\,°$C and no liquid nitrogen cooling is necessary. The throughput of the XFlash detector movable neck to the chamber is vacuum-tight and we can change the distance between the XFlash SDD crystal and the sample from outside without breaking the vacuum. The possibility to move the detector away from the sample is helpful during focusing of the proton beam or it can be used e.g. by very high count rates of individual samples. Another benefit is a small diameter of the neck – 19.2 mm which allows to work in a close geometry with the target. Last but not least, the best shaping time for the XFlash detector is between $0.25\,\mu$s and $1.0\,\mu$s when compared with the Si(Li) with convenient shaping time of $10-24\,\mu$s, what restricts the maximum input count rate of Si(Li) detectors to about 15 kcps with already more than 50 % dead time. Indeed, we have measured with the XFlash detector even by 300 kcps with a dead time of 60 %, the shaping time was $0.5\,\mu$s. The resolution of the XFlash detector is very satisfactory too: 152 eV by the analogue acquisition system and with a shaping time of $0.5\,\mu$s, while with the digital acqisition system and shaping time of $0.5\,\mu$s we get the best resolution of 156 eV.

The disadvantages are following:

1. Low efficiency compared with standard Si(Li) detectors. The reason why is explained by the detector surface of only $10\,\mathrm{mm}^2$ instead of typical surface of $50\,\mathrm{mm}^2$. This option can be improved by putting the XFlash detector as close to the sample as possible. Since the diameter of the detector neck is only 19.2 mm, this requirement can be well fulfilled. The closest distance we have used for measurements was 15 mm because of the geometry, see Figure 2.6 or 2.7. However, we measure usually at the distance of 2.75 cm or 3.75 cm from the sample because we sweep the beam by $5 \times 5\,\mathrm{mm}^2$ on the collimator: 1) for normalization purposes and 2) for homogenization of the proton beam. We can compensate the low efficiency of the XFlash detector by longer measurement or simply by increasing the proton current and thus the count rate – if the sample characteristics allows it and as long as the energy resolution is not much worsened.

2. High purchase cost.

The detector is situated at the standard angle for PIXE measurements of $135\,°$ in respect to the proton beam direction (see Figure 2.6). The XFlash detector is equipped by a Dura-Beryllium window of $8\,\mu$m thickness, with transmission curve for X-rays showed in Figure 2.11.

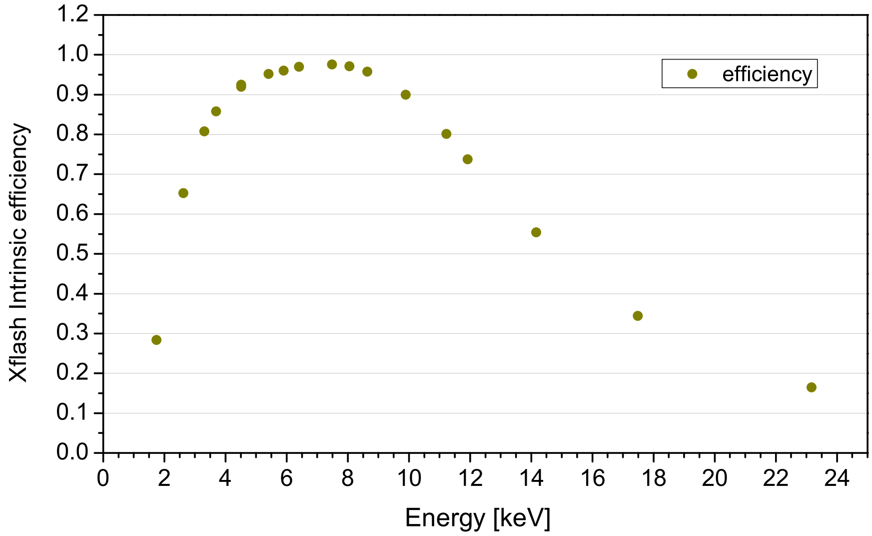

Figure 2.9: The intrinsic efficiency curve of the XFlash detector.

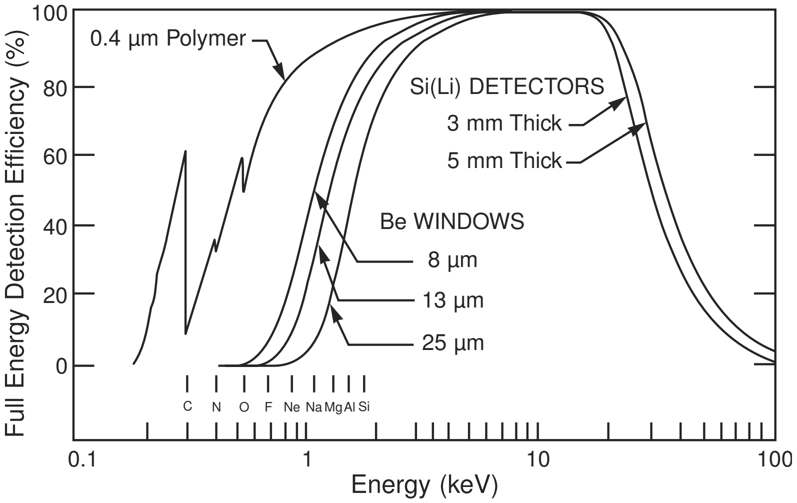

Figure 2.10: The Si(Li) detector efficiency curve from the Web site: http://www.canberra.com

The XFlash detects energies between $1.7 - 18\,\mathrm{keV}$ with still reasonable intrinsic efficiency higher than 30% (see Figure 2.9). However, with the inevitable protecting foil against the back-scattered protons – which would cause damage to the detector crystal – the detected X-rays energies have a lower limit at 2 keV threshold. We employ a protecting foil made of polycarbonate called Makrofol ($C_{16}H_{14}O_3$) with density $\rho = 1.2\,\mathrm{g}\cdot\mathrm{cm}^{-3}$. The present thickness of the foil was chosen as $110\,\mu$m however, we have determined by a measurement that the thickness is more likely $107\,\mu$m. According to TRIM calculations, the longitudinal projected range for 2.5 MeV protons in Makrofol is about $95\,\mu$m (Ziegler, 2004). With the help of XCOM calculations (Berger et al., 2004), we can see in Figure 2.12 the transmissivity of X-rays with different energies E_X through the $107\,\mu$m thin Makrofol foil.

2.2.6 Si(Li) detector

For the PIXE measurement, we have chosen also a Si(Li) detector, which has a larger surface area of $80\,\mathrm{mm}^2$ and a crystal thickness of 5 mm. The crystal is protected by a $25\,\mu$m Beryllium window. Thanks to these parameters, we have a supplemental X-ray detector eligible for higher energy X-rays. Indeed, the typical range of detectable energies for this Si(Li) detector is between 1.7 keV and 40 keV without the additional protecting foil in front of it. Having already the XFlash detector for lower energies $2 - 18\,\mathrm{keV}$, it is then very convenient to choose such a protecting foil for the Si(Li), which does not only stop the scattered protons but also cuts the low detectable energies. E.g. we would use a foil, which let pass through X-rays with energy ≥ 4 keV (resp. ≥ 10 keV – according to the sample matrix composition) to reduce the detection of low Z elements like Si, Cl, K or Ca (resp. up to elements with Z=30, by cutting Fe, Cu and Zn as well). These elements occur in many different sorts of samples in high concentrations (as major elements) and the large intensity of their characteristic X-rays evokes overloading of the detection and acquisition system, creates higher background continuum in the spectrum and increases the number as well as area of the pile-up peaks. Therefore, the protecting foil helps also to increase the sensitivity of the system for trace elements with $Z > 20$ (resp. $Z > 30$). Moreover, by the input count rate of about 15 kcps, the Si(Li) acquires with the maximum efficiency of 50 %. Therefore, the maximal reasonable input count rate is only about 5 kcps whith the efficiency of about 75 % and we usually try to acquire at 1 – 2 kcps. When the X-rays of major elements are suppressed, the detector is more sensitive to trace elements. The constrain of 5 kcps is caused by typically long shaping time necessary for a good energy resolution of Si(Li) detectors: we are using $10 - 12\,\mu$s, common is even to use $24\,\mu$s. The best energy resolution measured with the analogue electronics was obtained with the shaping time of $10\,\mu$s: by 1000 cps at 5.90 keV the resolution was about 168 eV. With the digital acquisition system and the same conditions we have obtained 178 eV of energy resolution.

The standard distance between the Be-window of the Si(Li) and the sample at the target position is 4.2 cm, and the minimal distance allowed by the geometry is 2.5 cm.

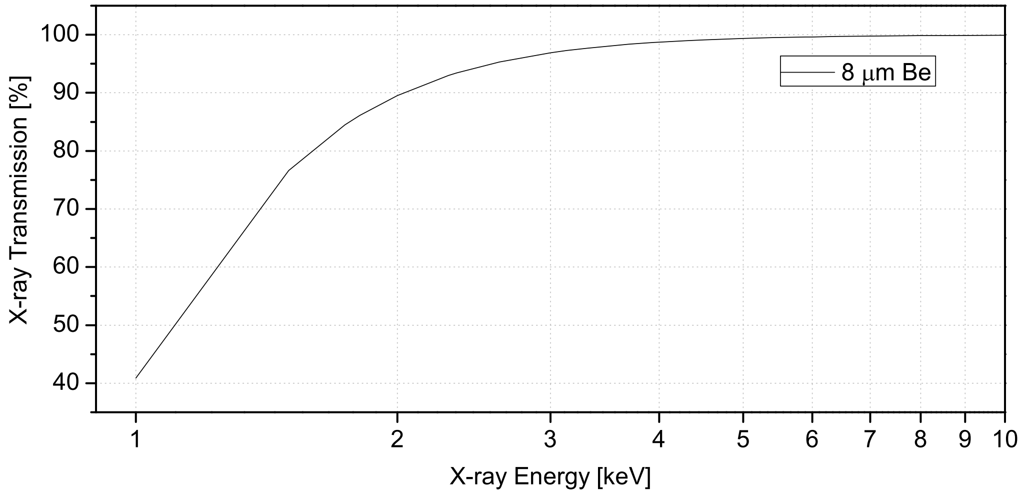

Figure 2.11: The transmission of X-rays with energy between 1 and 10 keV through a 8 μm thin Beryllium window of the XFlash detector.

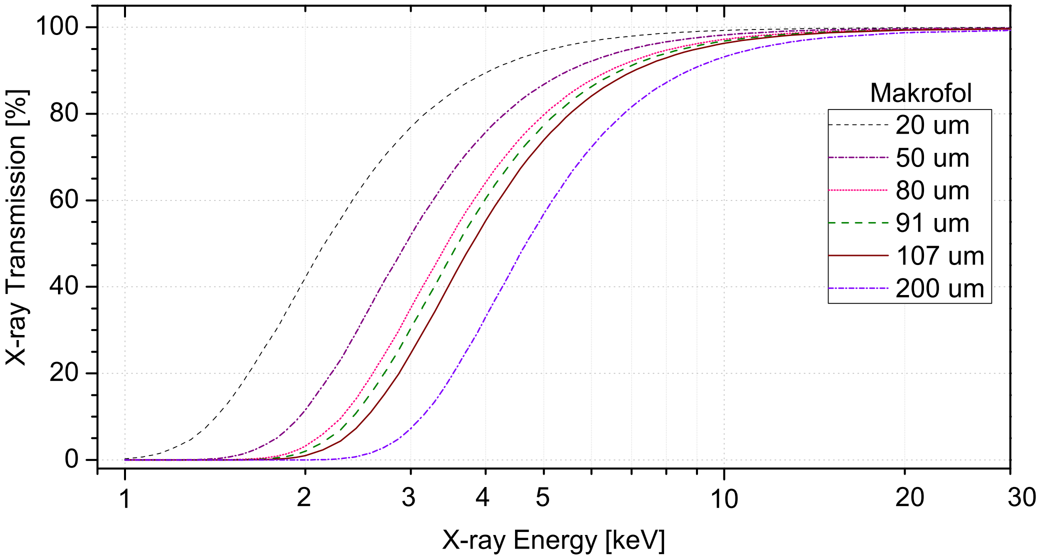

Figure 2.12: The transmission of X-rays with energy between 1 and 30 keV through a Makrofol foil ($C_{16}H_{14}O_3$) of different thickness.

The Si(Li) detector is situated at 135 ° with respect to the proton beam direction and it can be exchanged with a HPGe detector for Proton Induced Gamma-Ray Analysis (PIGE)[3].

2.3 Data analysis

For a reliable data analysis, we have to understand the characteristics of the spectrum acquired by the particular X-ray detector. As well, the detailed parameters of the detector are required.

To obtain absolute and true elemental concentrations of the explored specimen, we have to know all theoretical parameters from the relations (2.1) and (2.3) described in section 2.1, and we have to properly calibrate our PIXE instrument.

A well tested and adjusted acquisition system will contribute to the best achievable peak energy resolution e.g. in dependence on the input count rate. Very important is also to choose a reliable normalization of the proton charge delivered to the sample during the data acquisition and to convert it to some detectable value.

The PIXE spectrum is very complex and it contains – together with the required full energy characteristic X-ray peaks – also a background continuum arisen from many more or less well described effects like Auger escape electrons or from interfering peaks, like silicon escape peaks, pile-up peaks discussed e.g. by Campbell (1996). Therefore an analysing program, which includes all these parts of the spectra and contains large databases of necessary experimentally determined parameters is required for the analysis of difficult spectra. We have chosen and started to use a commercial program GUPIX developed by the PIXE group in Guelph, Canada (Campbell et al., 2004).

All these topics are important for a successful data analysis and the satisfactory results will be discussed in this section.

2.3.1 Detector response function

Although the natural width of the X-ray emission lines is only few units of eV described well by the Lorentzian function, the energy resolution of Si(Li) detectors is usually in range between 130–180 eV and Gaussian broadened, which is caused by different external factors described below. For small peaks, the Lorentzian shape of the natural peak width is not crucial for the analysis. However, larger peaks should be fitted by a Voigt function $V(x)$, that is simply a convolution of the Gauss and Lorentz functions:

$$V(E) = (G * L)(E) \tag{2.4}$$

where

---

[3] The HPGe detector (116 cm^3; resolution 2.05 keV at 1.33 MeV with analogue and 2.55 keV at 1.33 MeV with the digital system; max. count rate: 10 kcps; shaping time: 3 μs) is used for the detection of γ-rays induced by nuclear reactions of protons mainly with nuclei of light elements of the target material – complementary to PIXE

$$G(E) = \frac{A}{\sigma\sqrt{2\pi}}\, e^{-(E-E_0)^2/2\sigma^2} \tag{2.5}$$

is the Gauss function with E_0 the peak centre, A the peak area and σ the standard deviation of the peak with full width at half maximum $FWHM = 2\sigma\sqrt{2\ln 2}$ and

$$L(E) = \frac{2A}{\pi} \cdot \frac{w}{4(E-E_0)^2 + w^2} \tag{2.6}$$

is the Lorentz function with E_0 the peak energy, A the peak area and w is the full width at half maximum FWHM.

The energy resolution of the semi-conductor detectors is influenced by many internal as well as external factors:

- statistical fluctuations of the charge-carrier formation after the interaction of X-ray with the detector crystal
- leakage current
- drift of detection parameters
- electronics noise by the signal processing
- protons back-scattered to the detector
- external electromagnetic fields close to the detector (vacuum pumps)
- vibrations of the detector (vacuum pumps)

2.3.2 PIXE spectrum

The acquired PIXE spectrum is closely related to the detector response function explained above.

Shape of characteristic X-ray peaks Two main parts of the characteristic X-ray peak can be recognized in the spectrum: one is described by a Gauss function and caused by the above mentioned effects. If necessary (large and L- peaks), it can be convoluted with the intrinsic Lorentz peak width. The second part is the low energy tailing (visible mainly at the low energy peaks $<$ 10 keV). This tail is caused mainly by two effects. First is the incomplete charge collection (ICC) within the detector crystal together with the imperfections of the semiconductor crystal grid. ICC is a near-surface effect, therefore more pronounced by low energy X-rays and it results in a shape in the spectra empirically well described by an exponential tail and a flat shelf at the low energy part of the X-ray peak. Second contributor is the radiative Auger effect (RAE) (Campbell, 1996). RAE is caused by simultaneous emission of X-ray and Auger electron. In the PIXE spectrum, the most intense RAE originates from the KMM process contributing to the K_β peaks of higher intensity.

The intensity of the RAE reaches 1 – 5 % of the X-ray peak intensity and it can be fitted by an additional Gauss function at the low-energy part of particular X-ray peak. The good fitting of RAE is more important by the analysis of L-lines than of K-lines. Both effects decrease for increasing X-ray energy: above 15 keV the effects are already negligible. However at these energies, Compton scattering effect is more essential and creates typical Compton-background between E_0 and E_1, which is the energy of once Compton-scattered X-ray backwards at 180 °,

$$E_1 = E_0 \frac{m_e c^2}{m_e c^2 + 2E_0} \tag{2.7}$$

If the Compton-scattering appears more than once, the resulting minimum energy of the Compton-scattered photon will be lower than E_1.

A minor contribution to the high energy side of the X-ray peak can be caused by a double ionization when K-line X-ray is emitted simultaneously with the creation of L-line vacancy. This effect is more obvious for light elements K X-rays (Campbell, 1996).

Silicon-escape peaks Next peak appearing in the PIXE spectrum measured with a detector based on a silicon crystal, is so-called "silicon-escape peak". This peak is placed 1.74 keV bellow any strong peak in the spectrum, from which the escape peak originates, see Figure 2.13. For small peaks, the silicon-escape peak is not visible in the background continuum, because its surface is only in order of percent of the original X-ray peak area. The silicon-escape peak arises by the interaction of the original X-ray with energy E_X with the detecting Silicon crystal, this interaction give rise to a silicon X-ray with energy E_{Si} = 1.740 keV and this X-ray photon leaves the crystal. The energy left and also detected in the crystal in then $E_X - E_{Si}$.

Pile-up peaks Last important contributing peaks appear by high acquisition input count rates: then we will see pile-up peaks in the spectrum. These pile-up peaks appear in the spectrum when the electronics obtain two signals so fast next to each other, that those two energies E_1 and E_2 are detected as one peak with the sum energy $E_1 + E_2$. Usually, the pile-up peaks of the most intensive X-rays – $2\times E_{K\alpha}$ and $2\times E_{K\beta}$ can be clearly recognised in the spectrum as well as their combination $E_{K\alpha} + E_{K\beta}$. An example is presented in Figure 2.13. The area of pile-up peaks strongly depends on the detector and acquisition electronics. For the analogue electronics, a Pile-Up Rejection (PUR) circuit can be used to reduce the pile-ups. With digital electronics, the pile-up peaks are much better reduced than with an analogue system. It is mainly due to the very short shaping time of the XFlash detector that the pile-up peaks are strongly reduced in a typical spectrum of our PIXE measurements (see 2.2.5). Another possibility, how to reduce the pile-up peaks is the use of the so-called deflection system. This system with a condensator and a logical circuit deflects the proton beam for the length of the time when one X-ray signal is processed by the acquisition electronics, so the possibility of getting pile-up peaks is very reduced (Voltr et al., 2002).

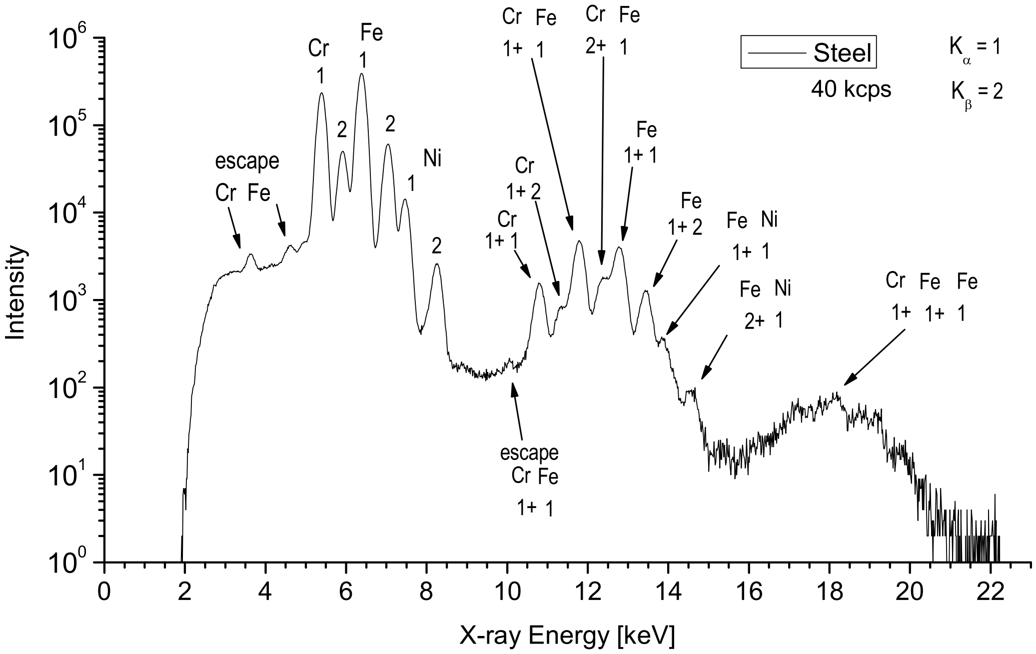

Figure 2.13: Example of the PIXE spectrum of a pure steel with complicated pile-up peaks of the first and even second order. The spectrum of steel is very pure, it contains only three matrix elements: Cr, Fe and Ni. Some combinations of the pile-up peaks are marked in the spectrum as well as escape peaks of the pile-up peaks. This spectrum is an example, why a good analysing software and a good understanding of all the effect is necessary for a successful analysis of the elemental concentration of particular samples.

Background continuum The overall background in the PIXE spectrum is the smooth continuous background with a high bump at the low energy part of the spectrum, displayed e.g. in Figure 2.18 or 2.27. Its main contribution is brought by the secondary electron bremsstrahlung (SEB). The SEB is caused by electrons ejected from the target atoms by the ionizing radiation – proton beam, and decelerating in the Coulomb field of other atoms. The scattered electrons prefer to emit bremsstrahlung anisotropically with highest probability to the 90 ° and decreasing more rapidly to the backward angles than to the forward directions with respect to the incoming proton beam. That is also the reason, why the PIXE detectors are placed mostly to angles around 135 °[4]. The secondary electrons can create bremsstrahlung with maximal energy E_{max}, which is obtained from the forward collision of the proton with electron:

$$E_{max} = E_p \frac{4m_e}{m_p} \tag{2.8}$$

where the m_e and m_p, E_p are masses and kinetic energy of electron and proton, respectively and the electron is assumed to be free and stationary. For 2.5 MeV protons it means that the maximum energy of bremsstrahlung created by secondary electrons is about 5.5 keV.

We have observed during the experiments, that the SEB background is very intense at low energies (between 1-7 keV) and then it rapidly decreases up to about 15 keV for the case of the XFlash detector (see e.g. Figure 2.27). The intense low-energy part is caused by the electrons from outer atomic shells while the weak higher-energy part of the continuum background comes from the inner ionized electrons, mostly from K- and L- shells (Johansson and Campbell, 1988).

Much smaller contribution to the continuous background is coming from the proton bremsstrahlung and various radiative processes not negligible for a proton beam with energy of 1 to 3 MeV involving e. g. the excitation and following deexcitation of bound electrons of the target atoms, joined into the term Atomic Bremsstrahlung (AB) and described by Ishii and Morita (1984) and Ishii and Morita (1987).

Nuclear reaction background The shape and the height of the background caused by proton induced nuclear reactions depends on the energy of the proton beam and the composition of the target. The energy of the protons determines the cross-section for a proton induced nuclear reaction with nuclei of particular elements within the target itself as well as in the surrounding material of the PIXE chamber after proton scattering on the target, if the material of the PIXE chamber and equipment was not well chosen. The most probable proton reactions are (p,γ), (p,p´ γ) and (p,$\alpha\gamma$) on light elements like Li, B, C, N, O, F, Na, Mg, Al, Si or P. These reactions

---

[4] The choice of the detector to the beam angle of 135 ° instead of 90 °C by common geometry of the detector neck has the consequence of larger minimal achievable distance between the detector crystal and the target, which can lead to significantly reduced efficiency for some trace elements in thin samples.

are then used for the complementary PIGE analysis of the sample surface, when a well shielded HPGe detector for more energetic γ-rays is involved (ca. from 100 keV to 6000 keV). This needs, however, a major modification of the set-up.

Reactions to avoid are the (p,n) reactions when the emitted neutron can cause damages to the detector crystal. This fact contributes to the choice of a low proton beam energy for PIXE – below 3.5 keV, where is the threshold for e.g. the C(p,n)N reaction.

2.3.3 Calibration of the system

For an absolute efficiency calibration of the PIXE detectors radionuclides are employed. These particular radionuclides emit γ-rays as well as X-rays in a well determined ratio and the calibration procedure was thoroughly described and discussed first by Campbell and McNelles (1975) and ten years later by Campbell and McGhee (1986). The efficiency calibration is very demanding and requires not only good knowledge of the set-up geometry, theoretical parameters describing the probability of the emission of a particular X-ray, but also requests many different radionuclides, which are not always at hand. Therefore, calibration of the detector at given geometry is usually performed with so-called calibration standards. Calibration of an instrument with some standards proceeds in the best case under the same conditions expected for the real samples: the geometry must be kept as well as the detector set-up, protecting foil of the detector, the calibration standards are preferably similar to the characteristics of the specimens. On the other hand, it is not always simple to find standards satisfying all requirements.

Thin standards We have calibrated our PIXE instrument with a set of thin calibration standards of elements and compounds made by the MicroMatter company (MicroMatter, 2002). The standards of the chosen elements are evaporated and deposited with the thickness of about $50\,\mu\text{g/cm}^2$ onto a $6.3\,\mu$m thin Mylar foil and mounted on acrylic rings with a diameter of 25 mm. The actual thickness of the standards is certified to $\pm 5\%$. We have chosen 20 elements, which cover more or less uniformly the X-ray energies from 1 keV up to 35 keV and additionally care was taken to choose elements occuring in nature as well – e.g. we have taken rather a standard of Zn (Z=30) instead of Ga (Z=31) or a standard of Sr (Z=38) instead of Y (Z=39). With the help of the thin standards and GUPIX program for the analysis of the PIXE data, a set of values, which calibrate our PIXE system in existing geometry is created. The values are called H values and in principle they represent the solid angle, how the detector sees the sample. The H values will be described in detail in section 2.4.2. The knowledge of the H values allows an absolute analysis of the PIXE samples.

Calibration procedure The thin standards were fixed on the wheel and measured while the beam was swept on $5 \times 5\,\text{mm}^2$ area at the collimator with a central hole of 3 mm in diameter. The intensity of the proton current measured on the Faraday

Cup was about 8 nA. The beam was swept mainly to preserve the standards for next measurements and to avoid burning them through. After each standard, an empty target holder was measured to check, if the proton current collected on the collimator and on the Faraday Cup stays in the same ratio. During 12 hours of measurement, this ratio was the same within 2.5 %. First calibration took place in May 2004 for both XFlash and Si(Li) detector (with a distance from the target 2.75 cm for the XFlash detector and 4.2 cm for the Si(Li)). In November 2004 we have remeasured standards for 20 elements with the XFlash detector at the distance 3.75 cm far from the target and followed with a few representative standards at different distances to obtain dependence of the detector efficiency as a function of the distance. These measurements and their results will be discussed in the part 2.4.2 of this chapter.

2.3.4 Normalization of the proton charge

Thin samples

For thin specimens, when practically the entire proton beam passes through the sample (e.g. air pollution deposits on few μm thin low-Z foils), the proton charge is captured by a Faraday Cup behind the target and it is sent to a digital charge integrator (10 nC = 1 pulse). The Faraday Cup (FC) is supplied with a front-end negative voltage V = -1000 V. First, to avoid the secondary electron cloud created in the FC by impinging protons to escape the FC and to be collected by its walls. And second, not to allow the delta electrons stripped from the sample by the proton beam to enter the FC. This high voltage can be switched on only if the chamber is evacuated. Sudden sparks in the PIXE chamber, which are at once displayed by the camera only point out that the FC voltage is still on although we have started to put air inside the chamber to change the samples.

Thick samples

Here is the situation more demanding and in our case it will be more usual to analyze thick samples. Therefore we have tested out many possibilities of normalization (current on a collimator, while sweeping the beam to an area of $5 \times 5\,\mathrm{mm}^2$; backscattered protons measured by solar cells; protons scattered on a thin gold foil measured by a scintillator; the current on this thin gold foil ...). Some of other methods are still waiting to be tested (e.g. a thin rotating wire periodically crossing upstream the proton beam).

One of the easiest normalizations for our set-up is to sweep the proton beam to a collimator placed in our case about 24 cm in front of the target. The collimator is made of carbon plates with a central hole of 3 mm in diameter. We take and register the current on the collimator and compare it to a Faraday Cup current when the target position is empty. A second effect of sweeping is homogeneous distribution of the proton beam on the specimen – which averages the measurement through larger area of the sample and reasonably reduces the damage caused by heat (mainly for insulating samples – see section 1.3). We have experienced, the best sweeping area is in our case about $5 \times 5\,\mathrm{mm}^2$. With such a swept area, the ratio of the charge collected on collimator and on FC[5] is stable during 24 hours within 1 – 2.5 %. At the same time we still do not loose too much beam current on the collimator in comparison to the current going onto the sample – so that we can keep the irradiation time reasonably short to obtain the required data statistics. For the present, we use this method for the normalization. Another method of normalization is already described on page 11 in section 2.1.2.

2.3.5 Analogue acquisition

At the beginning of the PIXE experiments, we were using a common analogue acquisition system: The signal from the XFlash detector (kept at the temperature of about $-16\,^{\circ}\mathrm{C}$) went through its preamplifier to the main amplifier, where the signal was shaped (with a shaping time of $0.5\,\mu$s and proceeded to the Analog-Digital Converter (ADC) and to the PC. The acquisition software was developed in LabView© environment by my colleague Dr. Materna (2001).

2.3.6 Digital acquisition

In 2002, the PIXE data acquisition was exchanged by a digital system based on DGF-4C (Digital Gamma Finder - 4C revision E) CAMAC modules from the X-ray Instrumentation Associates (XIA, 2004). The main reason for choosing a digital system was that our institute is systematically changing all the instruments to digital electronics. The XIA modules have been already successfully used in our institute with MINIBALL, a large array of segmented Ge-detectors. The digital acquisition software for MINIBALL was developed by N. Warr for our institute (Warr, 2003), and it was convenient to reuse part of that software for the PIXE acquisition, too. The modifications to the acquisition software for the purpose of the PIXE experiments were implemented by Dr. Materna again in LabView© environment (Materna, 2002). An illustration of the digital acquisition program "Pixe_acguisition_system" is presented in Figure 2.14.

Another advantage of using the digital acquisition also for PIXE is the fact that our more or less simple PIXE set-up is an useful testing field for the digital electronics characteristics before it would be implemented for other, much more complicated instruments (usually 6 and more HPGe detectors with the option of coincidence measurement).

The visible difference between common analogue and digital modules is the compactness of the DGF module. Indeed, the filtering, amplifying, digitizing and processing parts of DGF are wired on one board, see Figure 2.15. The acquisition parameters

---

[5] The charge collected in FC is real, what is not the case of collimator: some of the secondary electrons are ejected from the carbon plate and get lost for the charge collecting wire.

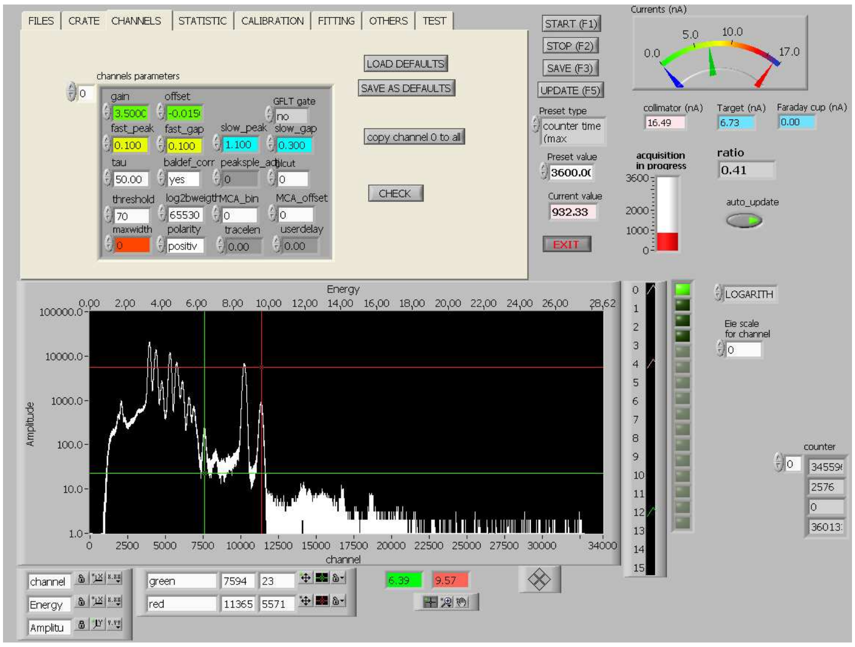

channels parameters 0
gain 3.5000
offset -0.015
GFLT gate no
fast_peak 0.100
fast_gap 0.100
slow_peak 1.100
slow_gap 0.300
tau 50.00
baldef_corr yes
peaksple_adj 0
blcut 0
threshold 70
log2bweigth 65530
MCA_bin 0
MCA_offset 0
maxwidth 0
polarity positiv
tracelen 0.00
userdelay 0.00
Preset type counter time (max
Preset value 3600.00
Current value 932.33
collimator (nA) 16.49
Target (nA) 6.73
Faraday cup (nA) 0.00
ratio 0.41
LOGARITH
Eie scale for channel 0
counter 0: 345596, 2576, 0, 36013
channel
Energy
Amplitu
green 7594 23
red 11365 5571
6.39 9.57

Figure 2.14: Illustrative picture of the digital acquisition program for PIXE written in Labview.

are set on PC and transferred to the DGF before the start of acquisition.

The option of controlling the digital acquisition by software makes scanning of the input parameters possible. The visualization of their dependences directly on the PC monitor allows one to find the best parameters for the acquisition. The spectra acquired during the PIXE measurement are then transferred from the DGF memory to the PC by SCSI bus (Jorway 73A controller) either at the end of the measurement or upon request. Since the acquisition process takes place in the DGF module itself, the acquisition PC is free to be used e.g. for data analysis. The digital acquisition is schematically illustrated in Figure 2.16. An example of parameters sent to the DGF module before the start of PIXE experiment is listed in Table 2.3.

The processing of the signal, which comes from the detector is different in the sequence for digital system and for the analogue system (Warr, 2004). Analogue electronics first filter the input signal. The smoothed signal is then converted to a digital value to find the height of the impulse, and this value is then proportional to the energy of the signal. Digital electronics sample the signal continuously, the data are then filtered by implemented numerical algorithms and the energy of the impulse is extracted after it. The digitizing of the signal at an earlier stage than with analogue electronics brings the advantage that no electronic noise is added to the processed signal.

In the near future, we want to implement an automatic adjustment of acquisition parameters for each particular set of samples according to the intensity of the proton

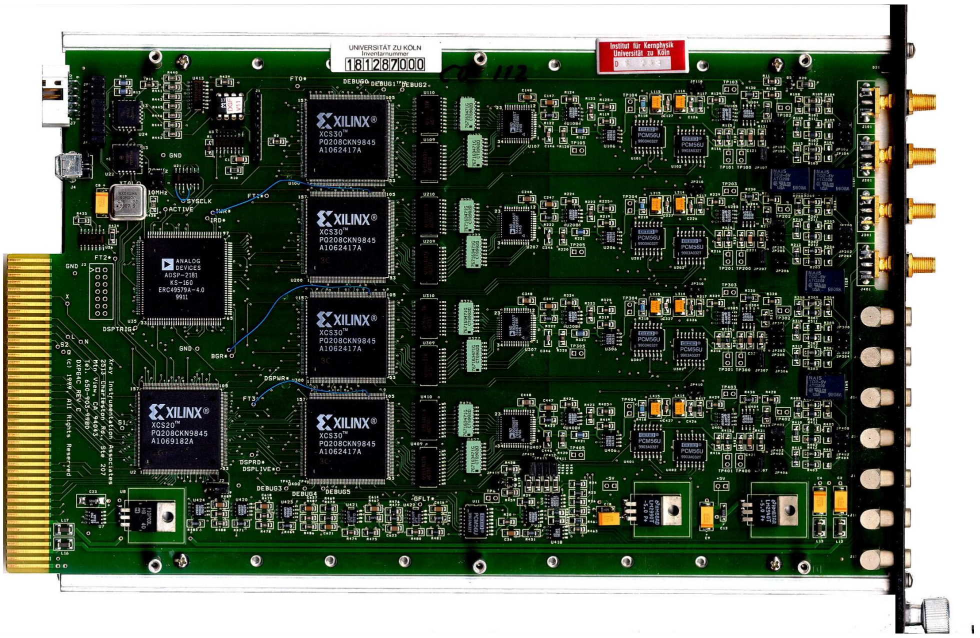

Figure 2.15: DGF module with four input channels (right). Data acquisition and signal processing for four detectors can be proceeded by one module.

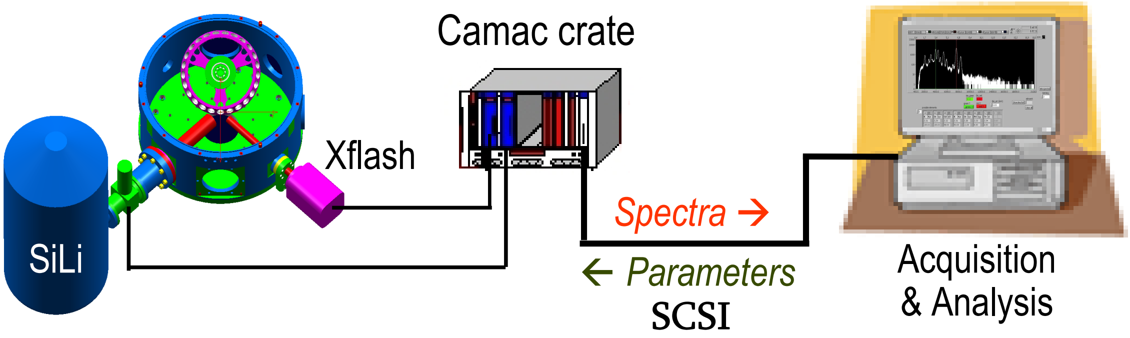

Figure 2.16: Schematic view of data acquisition from the PIXE detectors with DGF-4C modules in the CAMAC crate and the communication through the SCSI bus with the acquisition PC. Since the data are stored in the memory of the DGF modules, the acquisition PC can be used for data analysis at the same time of acquisition. Before the start of acquisition, the parameters for the digital acquisition are sent from the PC to the DGF modules.

gain = 3.50	offset = - 0.015
Fast Peak = 0.100	Fast Gap = 0.100
Slow Peak = 1.100	Slow Gap = 0.300
Tau = 50	Baldef corr. = Yes
Threshold = 70	GFLT Gate = no
MCA offset = 0	Log2bweight = 65530
Polarity = positive	other = 0

Table 2.3: Example of the DGF parameters used for the PIXE measurement with the XFlash detector.

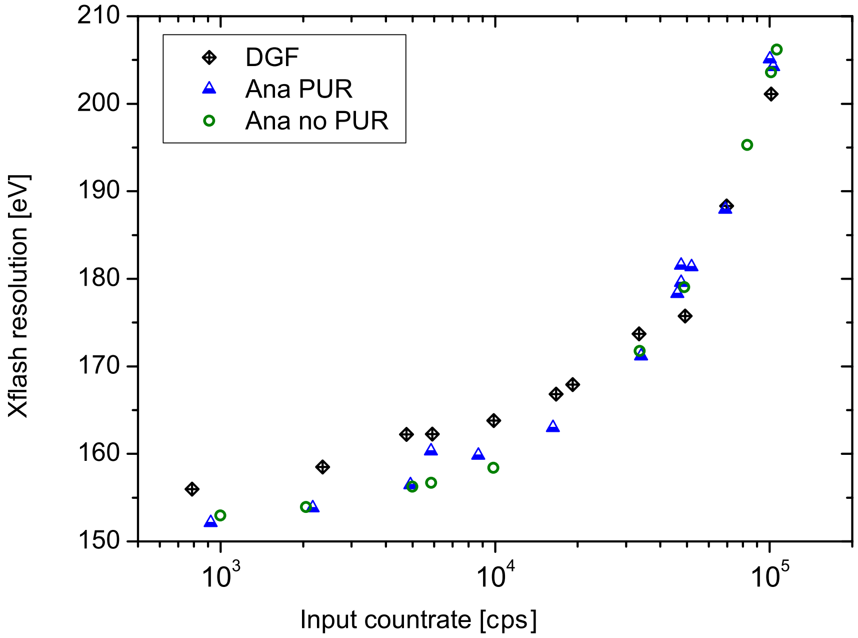

Figure 2.17: XFlash detector energy resolution at 5.90 keV in dependence on the acquisition system and input count rate. The analogue system, independently of usage of the Pile-Up Rejection (PUR) circuit is advantageous for low input count rate, while the digital DGF system takes advantage at high count rates.

beam, input to output count rate ratio and other parameters. During the PIXE experiments, we have compared the results of the digital acquisition with our standard analogue system. Still, the digital acquisition results in a generally slightly worse detector energy resolution (e.g. for the XFlash detector at 1000 cps for Mn line of 5.9 keV we obtain (151.5 ± 0.4) eV with the analogue system and (156.0 ± 0.4) eV with the digital system).

The comparison of the XFlash detector resolution for the Mn line of 5.9 keV in dependence on the input count rate is presented in Figure 2.17. In the Figure, the analogue system with Pile-Up Rejection circuit (PUR), without PUR circuit and the digital acquisition (by DGF-4C module) system are compared. By low count rates, the analogue system has better resolution, while with increasing count rate, the digital system is advantageous by its energy resolution.

2.3.7 GUPIX analysis

GUPIX is a program running under MS-DOS developed for precise fitting and automatic description of the PIXE spectrum. GUPIX is based on the fundamental physical processes occurring during the PIXE measurement described partially in sections 2.1 and 2.3. GUPIX contains also a large and regularly updated databases of the theoretical parameters from the relations (2.1) and (2.3) between the X-ray peak net area A_Z and the concentration c_Z of the element. GUPIX uses the databases for the determination of the sample composition. The program supports data acquisition with a common Si(Li) or a planar Ge detector. The XFlash detector is not completely supported by the built-in parametrization of GUPIX for the detectors, still we were able to parametrize the XFlash detector so, that we can perform a reliable sample analysis of its spectra with GUPIX, too. For the GUPIX analysis, first we have parametrized our two detectors according to the requirements given by the authors (Campbell et al., 2004) and we have written the values to the AP0DET.dat file in the GUPIX directory. This file is then loaded before the start of the GUPIX analysis. In Table 2.4, the parametrization of the XFlash and Si(Li) detectors from the AP0DET.dat file is listed.

2.4 Results and discussion

2.4.1 PIXE background measurement

Before we start the PIXE measurement and data acquisition, we have to know, which background is created by the protons in the PIXE chamber without any sample. This value is an important indicator, if the PIXE chamber was well constructed, if appropriate materials were chosen and if the protons do not create too much background counts while being scattered to the sample surrounding. The background spectrum measured for 500 s contains only 54 counts, that gives a count rate of 0.1 cps. This value is more than satisfactory. Therefore, in the case of thin samples, much more

AP0DET.DAT Parameter	XFlash	Si(Li)
Be window thickness (cm)	0.0008	0.0025
Au/Ni contact layer thickness (cm)[1]	$1 \cdot 10^{-9}$	$5 \cdot 10^{-6}$
Si crystal thickness (cm)	0.030	0.50
Target to crystal distance (cm)[2]	0	4.2
Ag/At cutoff energy (keV)[3]	1.84	1.84
maximum nominal det. res. at 5.9 keV (eV)	165	180
default τ (ns)[4]	500	500
Z values for window, electrode[5] and crystal	4 28 14	4 79 14
Pulse dead time (μs)[6]	50	78
Voigtian line shape switch with cutoff[7]	T 1000	T 1000
Min. background value for MDL calculation[8]	1	1
line shape parameters[9]	20 0 1.74 0 0 0	20 0 1.74 0 0 0

Table 2.4: Parameters of the XFlash and Si(Li) detectors as required by the GUPIX program:

[1] XFlash detector has no contact like Si(Li), so the thickness was reduced to minimum. We have checked the impact on the H values by changing the electrode thickness, and there were no significant differences.

[2] XFlash detector is collimated.

[3] Description of the incomplete charge collection.

[4] Describes the default pile-up τ value: this value is not of high importance.

[5] Here the electrode material of the XFlash detector is not well-defined for GUPIX. We have checked the impact, if the electrode was made of Ni or Au and the resulting H values did not change significantly but Ni electrode creates less background around 2 keV, so this was chosen for the XFlash detector.

[6] This value is only informative, not used for the analysis.

[7] T = true; for peaks higher than 1000 counts use the Voigtian shape fitting.

[8] The minimum background level for computation of the limits of detection (LOD or MDL).

[9] Procedure used to fit the peak (low-energy tail), the offset of the silicon escape peak and parameters describing the background.

More information to the parameters can be found in the Manual to GUPIX program, part named “GUDET.dat” (Campbell et al., 2004).

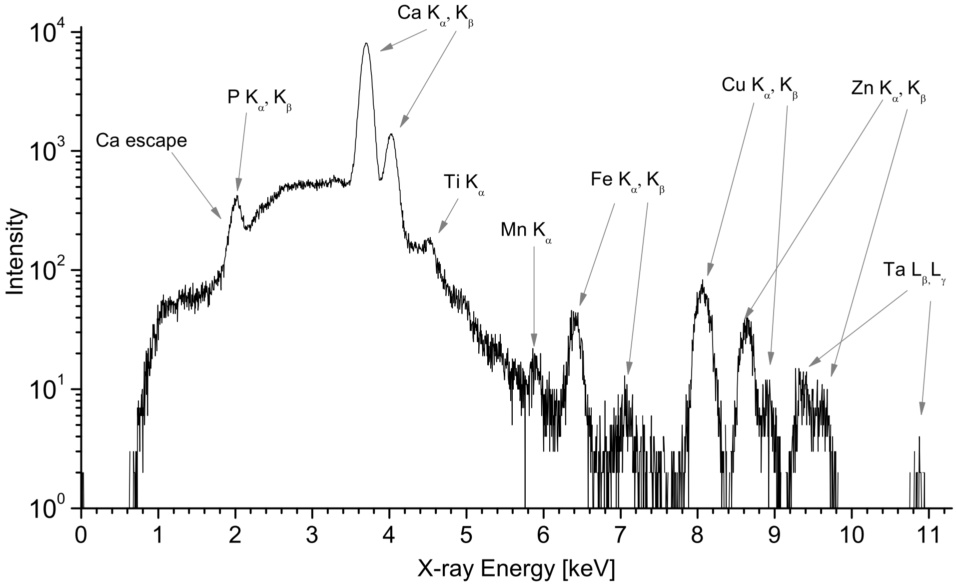

Figure 2.18: Spectrum of a blank Mylar foil, 6.3 μm thin. We have measured the Mylar foil for 3200 s, integrated charge at the foil was 20.38 μC, the data count rate detected by the XFlash detector was 164 cps.

important is the background created by the backing material, which causes the low energy bump, as shown for the case of 6.3 μm thin Mylar foil in Figure 2.18.

The 6.3 μm thin Mylar foil is a backing foil for the MicroMatter thin standards, which were used for the calibration of the PIXE set-up. The Mylar foil contains lots of elements that can affect the correctness of the concentration determination and of the system calibration for particular energies. On the other hand, the constant amount of Ca with stable concentration of about 2.1 μg/cm^2 was used as an internal control indicating, if the GUPIX analysis of the MicroMatter standards was performed successfully. We have measured the Mylar foil for 3200 s, the integrated charge at the foil was 20.38 μC, the data count rate detected by the XFlash detector was 164 cps. The Ta L-lines detected in the background spectrum come from the Faraday Cup (made of Ta), which have been eliminated afterwards by covering the FC with a thick carbon foil.

2.4.2 H values

The relation between the fitted net surface A_Z of the characteristics X-ray peak and concentration c_Z of the element Z in the sample (see also section 2.1.1) is given by:

$$A_Z = Y_t(Z) c_Z Q f \Omega \epsilon(E_X) T(E_X) \tag{2.9}$$

where $Y_t(Z)$ is the theoretical X-ray intensity per one μC of proton charge per unit concentration and per steradian $[counts{\cdot}\mu C^{-1}g{\cdot}cm^{-3}sr^{-1}]$ – these values are recorded in a database of GUPIX. Q is either the proton beam charge impinging the target in μC; then $f = 1$. Or, Q is some quantity proportional to the charge Q and when multiplied by the constant $f \neq 1$, it gives the correct charge in μC. Next, $\epsilon(E_X)$ is the intrinsic efficiency of the XFlash or Si(Li) detector for given energy E_X (see Figure 2.9 and 2.10 in section 2.2.5); $T(E_X)$ is the total transmission of the X-rays through any filters and absorbers between the specimen and the detector window.

If we know all other parameters in the equation (2.9), we can derive the concentration c_Z of the element of interest Z in the sample matrix. The equation (2.9) is valid only for a well described PIXE system, which is usually a very demanding task (Campbell and McGhee, 1986) and therefore another approach of calibrating the particular PIXE system and geometry was introduced by Campbell et al. (1993) with the use of H values measured experimentally with appropriate calibration standards. This H value combines the solid angle Ω (in sr) and factor f in equation 2.9.

For the explicit calibration of the PIXE installation at IKP, a set of H values dependent on the X-ray energy is used. Determination of the H values for the PIXE set-up in given geometry is performed with the MicroMatter thin standards. The calibration procedure of the PIXE instrument is shortly described in 2.3.3. From the part 2.3.7 we know that for a reliable GUPIX analysis, the parameters listed in Table 2.4, which properly describe the system must be well known (Campbell et al., 1993, 2004). A good calibration can be performed using this parametrization together with well determinated H values.

Understanding the H values In fact, we combine the solid angle Ω and f from the equation (2.9) into the H value, which is then usually dependent on the X-ray energy. However, here the correction factor f usually comprises not only the correction for the real proton charge but also other not well described features, including e.g. line shape parameters (which are different for K- and L- lines), fine tuning of the filter or absorber thickness, dead layer of the detector or thickness of the metal contacts at the silicon crystal. It is then only necessary to know the H values for different X-ray energies and we have the way free for determining the concentration c_Z of element Z in unknown samples:

$$c_Z = A_Z / Y_t(Z) Q H(E_X) \epsilon(E_X) T(E_X) \tag{2.10}$$

H values can be comfortably derived with the GUPIX program and those values are then used by the GUPIX for a subsequent analysis of the PIXE spectra. If the system was precisely enough described, we would obtain only one H value for the PIXE instrument. Unfortunately, this is usually not the case. The description of the system means a detailed description of the detector crystal (including the detector dead layer and contacts), protecting Be window and foil, line shape parameters and other.

GUPIX-derived H values for XFlash In the special case of the XFlash detector, the situation is even more challenging, because the GUPIX calculations are specialized for common lithium-drifted silicon detectors (or thin Ge detectors) and the XFlash detector has different construction and features when compared to Si(Li) (the XFlash detector has no dead layer, no real electrodes – for all details see section 2.2.5). Therefore, we can not expect the ideal case with H values, which would be independent of the X-ray energy.

H values: for the PIXE instrument at IKP

As already explained, for our PIXE set-up with the XFlash detector, we do not have a sufficiently well described system from the point of view of the GUPIX analysis requirements. Therefore, our H values will vary with energy and they will be different for K- and L- lines. A set of H values each for K- and L- lines was created and used for subsequent analysis of standard materials with complex composition to validate the correctness of these H value sets.

First, we have measured the H values for both the XFlash and the Si(Li) detector with the MicroMatter thin standards in May 2004. Already at that time we have analysed a Standard Reference Material (SRM) 1633b Coal Fly Ash and we have got very satisfactory results when compared with nominal values – they are listed in Table 2.5. The promising results are in press and will be published soon (Kudějová et al., 2005a). After the Tandem acceleration system was exchanged by the Pelletron (see 2.2.2), we wanted to remeasure the H values again as the beam stability was improved.

Therefore, we have repeated the calibration of the PIXE instrument with the XFlash detector in November 2004 (see section 2.3.3 for description of the calibration procedure). The measurement was performed with 20 MicroMatter thin standards at a distance of 3.75 cm between the detector and standards, the protecting Makrofol foil was 107 μm thin. The beam was focused to $1 \times 1.5\,\mathrm{mm}^2$ spot at the target position, the proton intensity during the full run of 20 calibration standards was constant at 27 nA at the Faraday Cup (FC) without sweeping. Again, the beam was then swept to an area of $5 \times 5\,\mathrm{mm}^2$ on the collimator with a central hole of 3 mm in diameter, so about 20 nA were measured on the collimator and 7 nA on the FC. The resulting set of H values, which have been used for the analysis of the PIXE data, is presented in Table 2.6.

For the analysis of the elements/energies without any determined H value, an interpolated H value is automatically created by the GUPIX program. For energies outside of the range with determined H values, the first or the last H values are adopted, see e.g. H values listed in Table 2.5 or 2.9.

Those H values measured both in May 2004 and in November 2004 at a distance of 2.75 cm under the same conditions are compared in Table 2.7. In the comparison, the H values measured in November 2004 are systematically higher for K-values by 2 – 3 %, which indicates that the distance was not totally identical, but the detector was slightly closer in November 2004.

Z	Element	H value	PIXE[1] [$\mu g/g$]	SRM 1633b[2] [$\mu g/g$]	PIXE to SRM[3]
14	Si	0.00925	299000 ± 25500	230200 ± 0	1.30
16	S	0.00925	2340 ± 170	2075 ± 21	1.13
19	K	0.00925	19690 ± 1010	19500 ± 390	1.01
20	Ca	0.00897	15300 ± 780	15100 ± 600	1.01
22	Ti	0.00835	8790 ± 580	7910 ± 160	1.11
23	V	0.00843	463 ± 34	295.7 ± 3.0	1.56
24	Cr	0.00851	258 ± 15	198.2 ± 4.0	1.30
25	Mn	0.00842	78.5 ± 9.3	131.8 ± 1.3	0.60
26	Fe	0.00846	77800	77800 ± 2300	1.00
28	Ni	0.00936	123.3 ± 8.0	120.6 ± 1.2	1.02
29	Cu	0.00856	171 ± 10	112.8 ± 2.3	1.52
30	Zn	0.00938	330 ± 20	210	1.57
34	Se	0.00801	15.8 ± 8.9	10.26 ± 0.21	1.54
37	Rb	0.00770	266 ± 31	140	1.90
38	Sr	0.00753	1382 ± 87	1041 ± 10	1.33
56	Ba(L_α)	0.00918	824 ± 320	709 ± 28	1.16
58	Ce(L_α)	0.00914	174 ± 80	190	0.92

Table 2.5: PIXE analysis of the SRM 1633b Coal Fly Ash measured in May 2004. The detector to target distance was 2.75 cm. The listed H values correspond to this geometry.

[1] The PIXE results were normalized to SRM nominal value for Fe concentration, therefore this value is given without any standard deviation.

[2] The SRM nominal values with given standard deviation are certified values, while those without any error are non-certified values.

[3] Ratio of the PIXE result to the SRM nominal values.

K-lines (3.75 cm)			**K-lines** (3.75 cm)		
Element	Energy [keV]	H value	Element	Energy [keV]	H value
Cl	2.62	0.0069354	Br	11.92	0.0038981
K	3.31	0.0052996	Mo	17.48	0.0040820
Ca	3.69	0.0053249	Cd	23.17	0.0044632
Ti	4.51	0.0048836			
Cr	5.41	0.0049835			
Mn	5.90	0.0049518	**L-lines** (3.75 cm)		
Fe	6.40	0.0049835	Element	Energy [keV]	H value
Ni	7.48	0.0054979	Mo	2.29	0.0073721
Cu	8.05	0.0050319	Cd	3.13	0.0059364
Zn	8.64	0.0055401	Te	3.77	0.0056896
Ge	9.89	0.0049162	Cs	4.29	0.0054701
Se	11.22	0.0041885	Pb	10.55	0.0051296

Table 2.6: H values determined for the XFlash detector, PIXE set-up and its geometry in November 2004. The distance between the XFlash detector and the sample was 3.75 cm, the protecting Makrofol foil in front of the detector window was 107 μm thick (however, for the GUPIX parametrization, virtual thickness of 91 μm was employed – see page 46).

Element	Energy [keV]	May 2004	Nov 2004
H value: K-lines (2.75 cm)			
Ti	4.51	0.008350	0.008530
Mn	5.90	0.008422	0.008604
Cu	8.05	0.008557	0.008828
Se	11.22	0.008007	0.008272
Sr	14.16	0.007569	0.007587
H value: L-lines (2.75 cm)			
Sr	1.81	0.017863	0.018851
Cd	3.13	0.010010	0.009840

Table 2.7: Comparison of H values determined for the XFlash detector and the PIXE set-up at IKP both in May 2004 and in November 2004. The distance between the XFlash detector and the sample was 2.75 cm, the protecting Makrofol foil in front of the detector window was 107 μm thick (however, for the GUPIX parametrization, virtual thickness of 91 μm was employed – see page 46).

Normalization of the proton charge

The proton charge collected on the FC and on the collimator “Coll” during the measurements of standards was used to control the stability of the proton beam intensity. After each thin standard sample, empty position was remeasured and the ratio “charge-on-collimator” Q_{Coll} to “charge-on-FC” Q_{FC} was determined and averaged for each set of standards measured under the same conditions.

The proton charge-on-FC Q_{FC} for measurement of standards was then corrected with the help of the corresponding charge-on-collimator Q_{Coll} by about 2 % because the standards are in reality not ideally thin samples and the registered charge-on-FC Q_{FC} was therefore a little bit decreased in contrast to the real charge impinging the sample.

Corrections to LT and OCR With the use of Q_{FC} or Q_{Coll} we measure the complete charge during the time of sample irradiation – real time RT. However, the signal from the detector acquired by the electronics is processed only during its lifetime LT. During one particular signal processing, the ADC rejects the signal from the amplifier – it causes a dead time $DT = RT - LT$. The counter of the proton charge – the digital charge integrator – works independently on the signal processing part and therefore it is not affected by its dead time DT and acquires the charge deposited to the sample in a real time RT. Therefore, we have to correct the measured charge to the LT of the acquisition system.

As well, we take into account the number of counts entering into the main amplifier and the number of counts processed by the amplifier. The amplifier does not process any next impulse from the detector before the shaping from the previous one was finished. Since we can measure the input count rate ICR into the amplifier and output count rate OCR of signals appearing in the sample spectrum we can make the following correction for the proton charge Q which gives rise to the measured PIXE spectrum:

$$Q_{corr} = Q_{measured} \cdot \frac{LT}{RT} \cdot \frac{OCR}{ICR} \tag{2.11}$$

We have performed a careful analysis of H values with the GUPIX program, while many parameters for the GUPIX analysis were fine-tuned (thickness of the filter, thickness of the crystal, thickness of the Be window, ...) to obtain the most constant set of H values. The resulting set is presented in Table 2.6.

Mylar foil correction Since all MicroMatter standards are elements in form of thin layers evaporated on a Mylar foil, the composition of the Mylar foil was determined by measuring of the blank Mylar foil and by an iterative process, the concentration of detected elements was determined (see section 2.4.1 and Figure 2.18 on page 39). Necessary corrections were made to the concentration of a few MicroMatter standards: Ca, Cu and Zn.

Trace elements in Mylar foil (6.3 μm thin):

P: (1.41 ± 0.11) μg·cm^{-2}
Cl: (0.02 ± 0.009) μg·cm^{-2}
K: (0.02 ± 0.005) μg·cm^{-2}
Ca: (2.06 ± 0.04) μg·cm^{-2}
Ti: (0.02 ± 0.002) μg·cm^{-2}
Mn: (0.005 ± 0.001) μg·cm^{-2}
Fe: (0.02 ± 0.002) μg·cm^{-2}
Cu: (0.09 ± 0.006) μg·cm^{-2}
Zn: (0.06 ± 0.005) μg·cm^{-2}

A significant contribution to the concentration of the MicroMatter standard elements on the Mylar foil concerns the Calcium standard, whose concentration was therefore corrected from 23.3 to 25.4 μg·cm^{-2}. We have also changed the concentration of Copper from 46.3 to 46.4 μg·cm^{-2}, but this change is much lower than the certified accuracy of 5 % of the element density given by the producer MicroMatter (2002). This large systematic error 5 % of the concentration of standards is the main contribution to the overall accuracy of the PIXE analysis results, which could be otherwise less than 1 % for large peaks.

Fine-tuning of the Makrofol thickness parameter When we were fine-tuning the input parameters for GUPIX (e.g. parameters in Table 2.4 or those discussed on page 40), a strong effect in the H values dependence on the X-ray energy was found, when the virtual thickness of the foil was changed from the real value of 107 μm to e.g. 91 μm or 80 μm. The alteration of the H values is significant only for low energies as displayed in Figure 2.19 for both K- and L-lines.

Since the concentration determination of elements with low energy X-rays is problematic and with lower accuracy because of the reduced transmissivity through the Makrofol, we have decided to test the GUPIX analysis and results of some standard materials with various sets of H values, which correspond to a modified virtual thickness of the Makrofol foil (Král, 2004). The input of a Makrofol thickness modified to 91 μm for the GUPIX analysis turned out to give the most satisfactory results. This modified virtual thickness of the Makrofol foil to 91 μm is used for every GUPIX analysis of PIXE samples described in this thesis.

H values: dependence on distance Since the majority of the PIXE measurements were performed with the XFlash detector, we were interested in the dependence of H values on the distance between the detector crystal and the sample surface. Therefore, we have measured standards of elements giving good energy distribution of the X-lines at several distances: 2.00 cm, 2.75 cm, 4.75 cm, 5.75 cm and 7.75 cm. The conditions of the measurement were kept the same with the main measurement at 3.75 cm – for details see above page 41. The dependences of the H values of K-lines and L-lines on distance for different energies are demonstrated in Figure 2.20. One can clearly see the same curve for each distance, only shifted in the y-axis. In the ideal case, the point for each distance would lie on a constant line. In our case, the H values for lower energies show an increase. H values below 2 keV are no more reliable. This observation is well correlated with the transmission of the protecting Makrofol foil: Its transmission for 2 keV X-rays is only 1% according to XCOM calculations (Berger et al., 2004) and it decreases steeply for lower energies (see Figure 2.12 in section 2.2.5). Therefore the measurement of important elements like Si (1.74 keV) and Al (1.49 keV) are in our case loaded with large systematic error or not registered at all. It would be very convenient to change the protecting foil by some other low-Z material, that still does not let protons enter the detector crystal, on the other hand, the transmissivity for X-rays $\geq$ 1.5 keV would be higher. For example, Marlex foil (C_2H_4, $\rho = 0.93\,\mathrm{g}\cdot\mathrm{cm}^3$ stops fully the 2.5 MeV protons by a thickness of 105 μm. By employing e.g. 115 μm thick Marlex foil, the transmission for 2 keV X-rays would increase to 6.3% and the transmission for 1.74 keV Silicium peak would be 1.5%, that means about 15× higher transmissivity than with the 107 μm thick Makrofol foil.

The Makrofol foil is parametrized for GUPIX calculations using weighted pure elements, giving in a sum the thickness of the foil. This approach can be also a source of a systematic error in the H values determination since the C, H and O elements are taken like three layers with corresponding transmissivity and not like molecules with combined transmissivity. In the next Figure 2.21, a quadratic dependence of

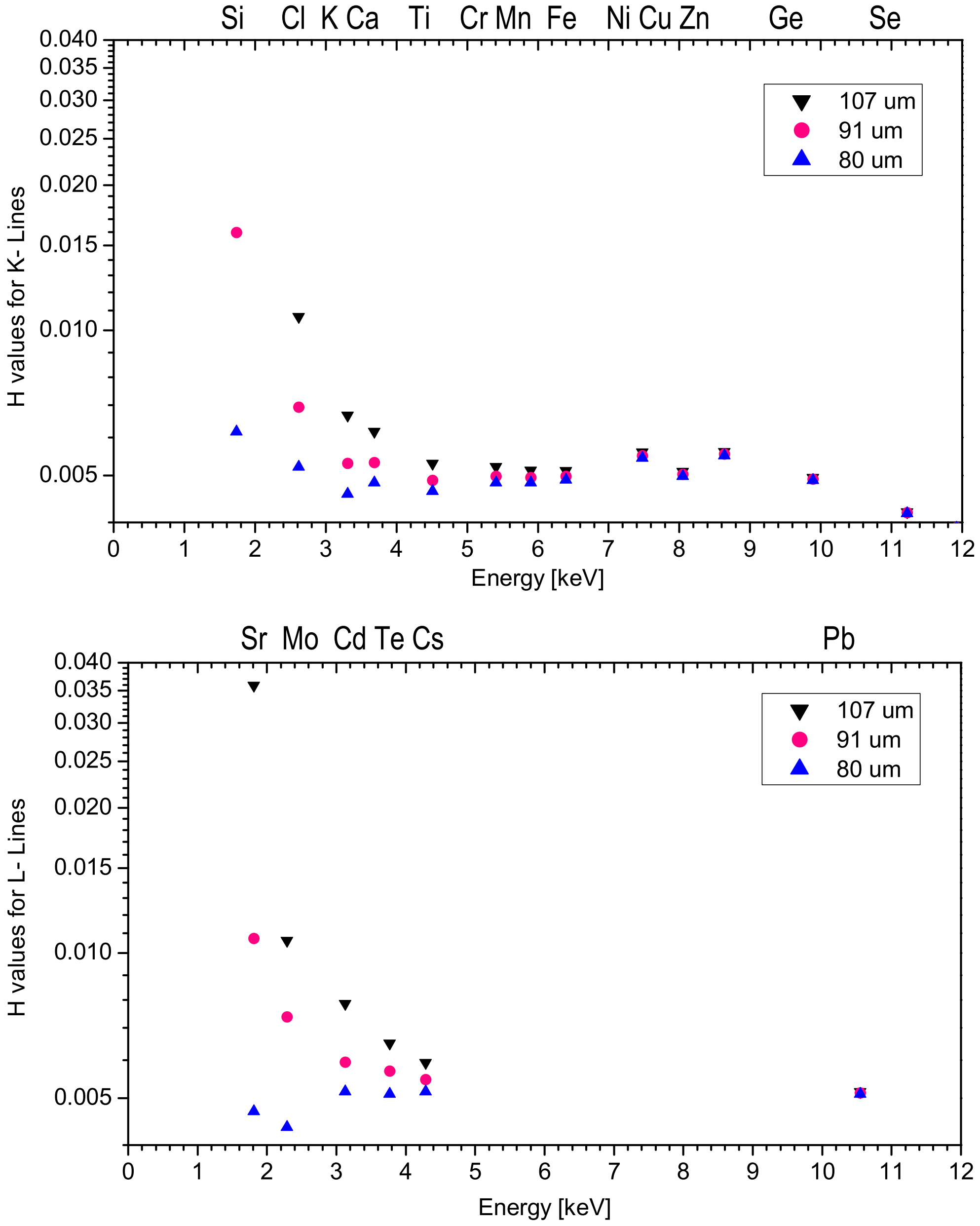

Figure 2.19: Modification of the H values by tuning the parameters describing the Makrofol thickness for the GUPIX analysis: upper graph for K-lines, lower for L-lines. After the analysis of SRM standards and of thick samples with all three sets of H values for each chosen thickness, the set with the virtual Makrofol thickness of 91 μm was selected as the one, which describes the PIXE instrument the best way.

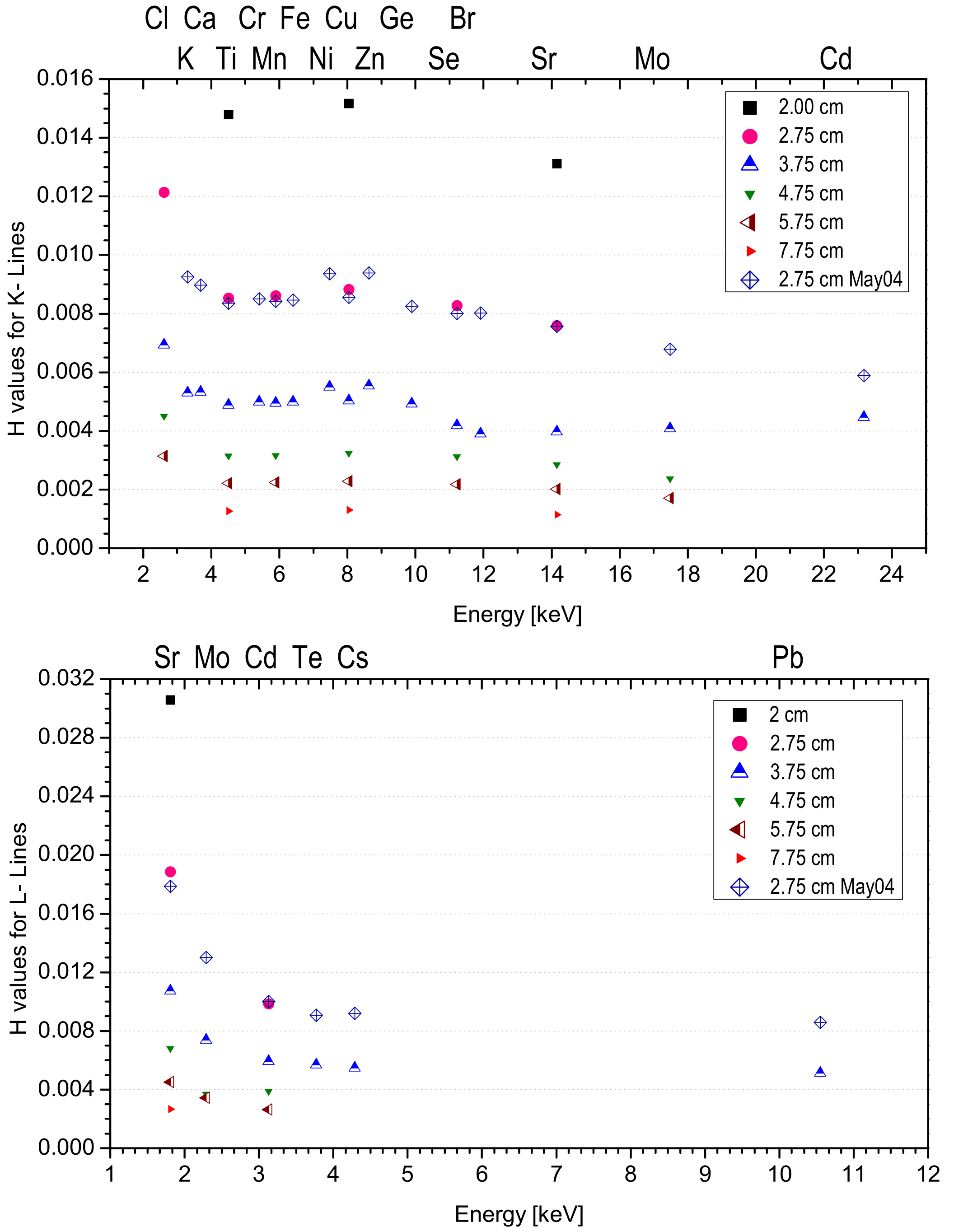

Figure 2.20: Dependence of the H values on energy for several distances: upper graph for K-lines, lower for L-lines.

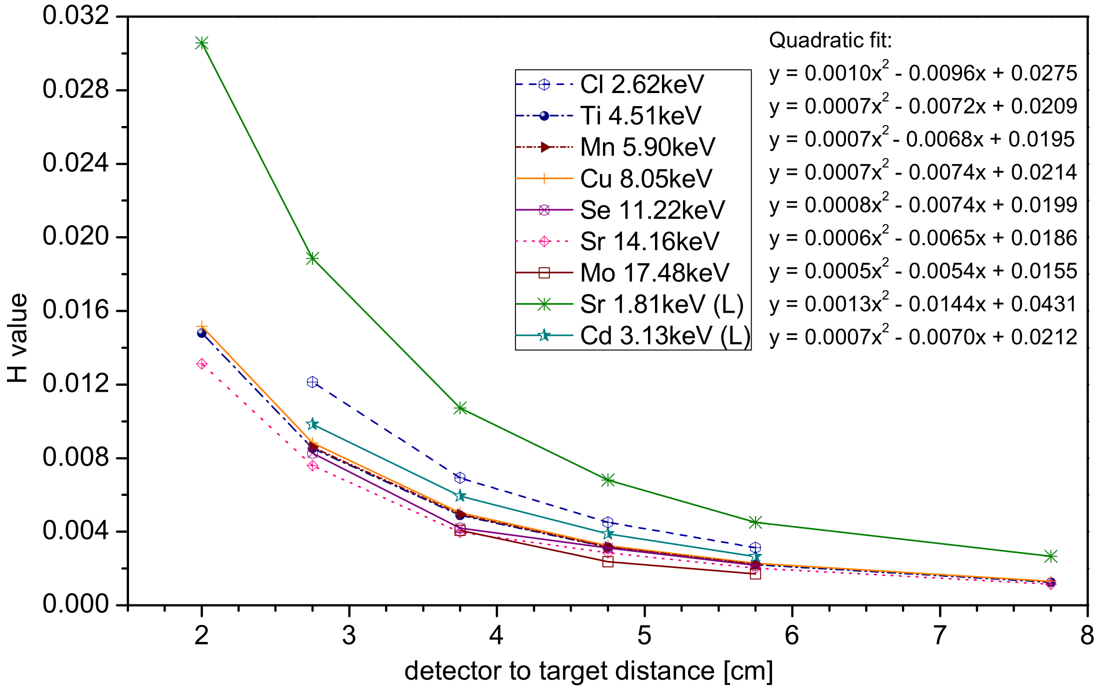

Figure 2.21: Dependence of the measured H values on distance between the XFlash detector and target for different X-ray energies. Quadratic fit for each set of H values measured for selected energy/element is included.

the H values on distance for selected energies is presented. Except for Sr L-line at 1.81 keV, Cl K-line at 2.62 keV and Mo K-line at 17.48 keV, the quadratic dependence is approximately given by a relation: $y = 0.0007x^2 + 0.007x + 0.02$, where the distance x is measured in [cm] and y represents the H value.

H values of the low energy X-rays While working on the best set of the H values describing the PIXE set-up, it was clear, that the H values around and below the 2 keV start to disturb the nearly constant line and increase rapidly.

It concerns K-lines of Si, Cl and L-line of Sr. The change of the Makrofol thickness for the GUPIX analysis from real 107 μm to virtual 91 μm helped to align the concerned H values better with the rest of them (see Figure 2.19). Based on the GUPIX results of the standard reference material analysis with selected sets of H values (with and without the K-lines of Si, Cl and L-line of Sr), we have chosen to exclude two of them: the H value of the K-line of Si and of the L-line of Sr. The following rule is kept by GUPIX for extrapolation of H values: GUPIX uses the first and last H value from the measured set and applies it for any energy out of the interpolated region. Therefore, for K-lines of elements with Z$\leq$ 17 we use the H value of Cl (Z=17, E_X = 2.62 keV) and for L-lines of elements with 38$\leq$Z$\leq$42 we use the H value of Mo (Z=42, E_X = 2.29 keV) .

H values of Zn and Ni In Figure 2.20 we can see, that the curve of H dependence on energy is very smooth, only the values for Zn and Ni are of about 11 % higher than the others in the region. Higher H values correspond to a little lower concentration of both standards than stated by MicroMatter. First we thought, that we made some error by the data evaluation and data fit of the Zn and Ni MicroMatter standards spectra, however, we got always the same H values for both elements. Then we decided, that the standards are maybe altered by our manipulation and the concentration of both elements is actually lower and we have put an interpolated H values for both elements using the H values of neighbour elements Fe, Cu and Ge. However, when we have analysed the SRM standards, we have got better agreement with the use of the original H values than with those interpolated. We have found out the same behaviour of the H values also by the calibration of the Si(Li) detector. Untill now, we do not know the correct explanation and we use the determined H values of Ni and Zn. An answer will come with a new set of the MicroMatter standards.

2.4.3 PIXE analysis of SRM standards

After a careful efficiency calibration of the PIXE detectors with the help of MicroMatter thin standards and the GUPIX program, thin samples with reproducible elemental composition were measured and analyzed also with GUPIX. As an example, four of the National Institute of Standards and Technology (NIST) Standard Reference Material (SRM) were chosen, see Table 2.8.

SRM Number	SRM Name	Time [s]	Charge [μC]	Backing
1547a	Peach Leaves	1800	10.93	Carbon tape
1570a	Spinach Leaves	4000	39.60	Carbon tape
1633b	Coal Fly Ash	5000	15.00	Carbon tape
1646a	Estuarine Sediment	5000	12.48	Carbon tape

Table 2.8: Parameters of the PIXE measurement for four SRM thin homogeneous powdered standards with a known composition: time of the measurement, integrated proton charge at the sample during the measurement and a backing material.

Conditions of the measurement 1547a Peach Leaves together with 1570a Spinach Leaves are standards for biological samples, while 1633b Coal Fly Ash is a standard for air pollution determination, and 1646a Estuarine Sediment is a standard for geological samples. All four standards are homogeneous powders and before the analysis, they were carefully glued as a thin layer onto a thin carbon tape of known composition:

Trace elements in the Carbon tape:

S:	(40 ± 25)	ng·cm^{-2}
Cl:	(328 ± 36)	ng·cm^{-2}
Ca:	(83 ± 9)	ng·cm^{-2}
Mn:	(16 ± 2)	ng·cm^{-2}
Fe:	(52 ± 5)	ng·cm^{-2}
Cu:	(43 ± 5)	ng·cm^{-2}
Zn:	(32 ± 4)	ng·cm^{-2}

The standards were irradiated during appropriate times (between 1800 s and 5000 s) to obtain reasonable statistics also for trace elements. A proton beam of 2.5 MeV focused to a $1.5 \times 2\,\mathrm{mm}^2$ spot at the target position was used to irradiate the samples. The proton beam was swept for normalization purposes to a $5 \times 5\,\mathrm{mm}^2$ area on a collimator with a circular hole of 3 mm in diameter and then the samples were irradiated by a proton current between 2.4 nA and 10 nA. An example of the PIXE spectrum of the SRM 1633b Coal Fly Ash sample acquired with the XFlash detector is presented and described in Figure 2.22. We can notice a Cl peak in the spectrum, which is not presented in the standard reference material but in the backing carbon tape. The Cl peak and the peak contributions for other elements due to the carbon tape were subtracted from the spectrum of the SRM samples for the final analysis. The results of the PIXE analysis in GUPIX and the derived H values described in previous section 2.4.2 were sorted into Tables 2.9, 2.10, 2.11, 2.12 and into Figures 2.23 and 2.24.

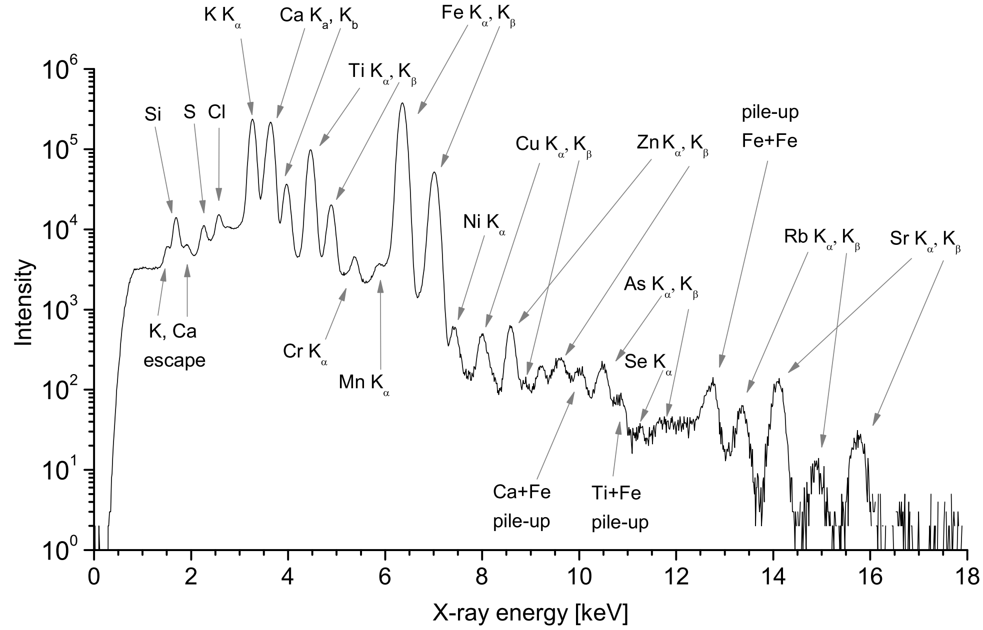

Figure 2.22: The PIXE spectrum of the SRM 1633b Coal Fly Ash sample acquired with the XFlash detector. The homogeneous powder of the Coal Fly Ash was deposited on a thin carbon tape.

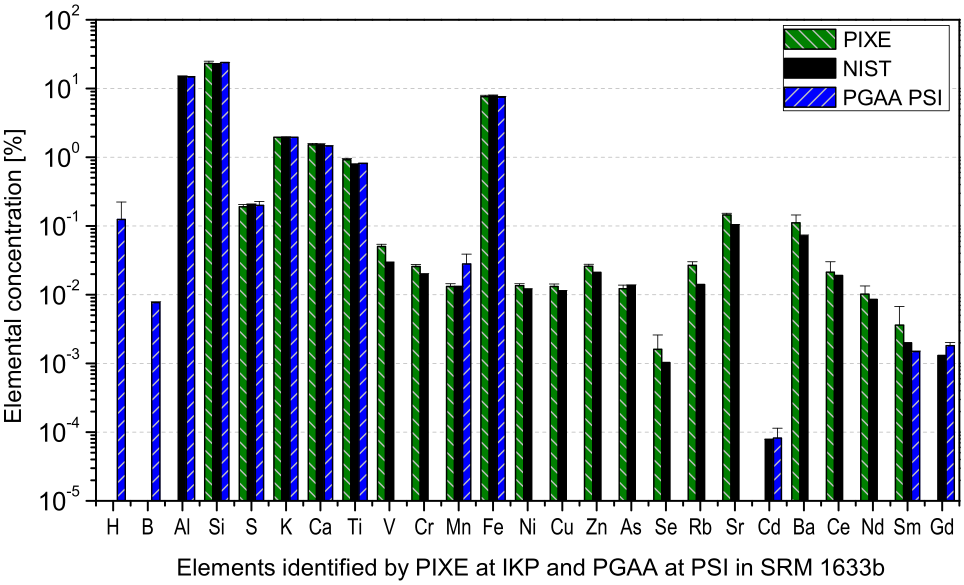

Figure 2.23: SRM 1633b Coal Fly Ash: results of the PIXE analysis of a thin sample compared to the nominal values given by NIST and to results of the PGAA analysis performed with the PGAA facility at PSI, 2001.

Z	Element	H value $\cdot 10^{-5}$	PIXE[1] $[\mu g/g]$	SRM 1633b[2] $[\mu g/g]$	PIXE to SRM[3]
14	Si	694	232300 ± 17800	230200 ± 0	1.01
16	S	694	1900 ± 150	2075 ± 21	0.91
19	K	530	19500	19500 ± 390	1.00
20	Ca	532	15110 ± 760	15100 ± 604	1.00
22	Ti	488	9190 ± 460	7910 ± 158	1.16
23	V	493	500 ± 40	295.7 ± 3	1.69
24	Cr	498	257 ± 17	198.2 ± 4	1.30
25	Mn	495	131 ± 14	131.8 ± 1	0.99
26	Fe	499	75990 ± 3810	77800 ± 2334	0.98
27	Co	523	183 ± 114	50	3.65
28	Ni	550	135 ± 9	120.6 ± 1	1.12
29	Cu	503	132 ± 11	112.8 ± 2	1.17
30	Zn	554	260 ± 16	210	1.24
33	As	456	122 ± 16	136.2 ± 3	0.89
34	Se	419	16 ± 10	10.26 ± 0	1.57
37	Rb	395	268 ± 35	140	1.91
38	Sr	397	1440 ± 90	1041 ± 10	1.38
56	Ba(L$_\alpha$)	546	1110 ± 340	709 ± 28	1.56
58	Ce(L$_\alpha$)	544	213 ± 89	190	1.12
60	Nd(L$_\alpha$)	542	102 ± 32	85	1.20
62	Sm(L$_\alpha$)	540	36 ± 31	20	1.82

Table 2.9: PIXE analysis of the SRM 1633b Coal Fly Ash, the detector to target distance was 3.75 cm. The listed H values correspond to this geometry.

[1] The PIXE results were normalized to SRM nominal value for K concentration, therefore this value is given without any standard deviation.

[2] The NIST SRM nominal values with given standard deviation are certified values, while those without any error are non-certified values.

[3] Ratio of the PIXE result to the SRM nominal values.

Z	Element	H value $\cdot 10^{-5}$	PIXE[1] $[\mu g/g]$	SRM 1646a[2] $[\mu g/g]$	PIXE to SRM[3]
14	Si	694	515000 ± 31600	400000 ± 0	1.29
15	P	694	230 ± 230	270 ± 11	0.84
16	S	694	2550 ± 170	3520 ± 35	0.73
19	K	530	8640	8640 ± 173	1.00
20	Ca	532	5600 ± 280	5190 ± 208	1.08
22	Ti	488	5870 ± 300	4560 ± 228	1.29
24	Cr	498	40.5 ± 5.5	40.9 ± 2	0.99
25	Mn	495	280 ± 16	234.5 ± 2	1.19
26	Fe	499	27470 ± 1380	20080 ± 402	1.37
27	Co	523	51 ± 45	5	10.23
28	Ni	550	29 ± 3	23	1.25
29	Cu	503	16 ± 4	10.01 ± 0	1.60
30	Zn	554	49.9 ± 6	48.9 ± 1.5	1.02
37	Rb	395	55.6 ± 15	38	1.46
38	Sr	397	79 ± 18	68	1.17
56	Ba(L_α)	546	264 ± 13	210	1.26
58	Ce(L_α)	544	73 ± 50	34	2.15
82	Pb(L_α)	513	37.0 ± 15	11.7	3.16

Table 2.10: PIXE analysis of the SRM 1646a Estuarine Sediment, the detector to target distance was 3.75 cm. Remarks to [1],[2],[3] are explained in Table 2.9.

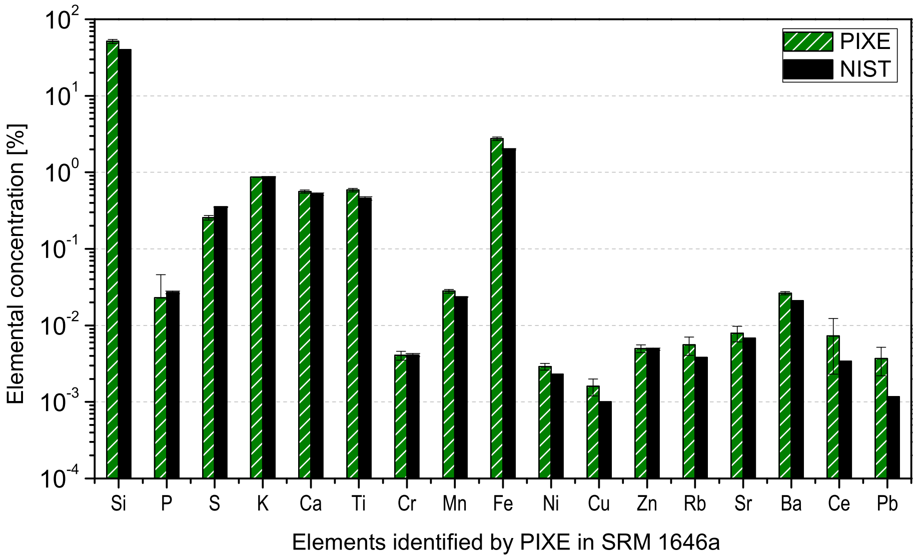

Figure 2.24: Results of the PIXE analysis of a thin sample compared to the nominal values given by NIST for the SRM 1646a Estuarine Sediment.

Z	Element	H value $\cdot 10^{-5}$	PIXE[1] $[\mu g/g]$			SRM 1547a[2] $[\mu g/g]$			PIXE to SRM[3]
16	S	694	1560	±	220	2 000			0.78
17	Cl	693	250	±	140	360	±	18	0.69
19	K	530	24300			24 300	±	243	1.00
20	Ca	532	14710	±	800	15 600	±	156	0.94
25	Mn	495	95	±	14	98	±	3	0.97
26	Fe	499	224	±	24	218	±	13	1.03
56	Ba(L_α)	546	220	±	40	124	±	4	1.79

Table 2.11: PIXE analysis of the SRM 1547a Peach Leaves, the distance between the detector and the target was 3.75 cm. Remarks to [1],[2],[3] are explained in Table 2.9.

Z	Element	H value $\cdot 10^{-5}$	PIXE[1] $[\mu g/g]$			SRM 1570a[2] $[\mu g/g]$			PIXE to SRM[3]
15	P	694	6040	±	680	5 180	±	104	1.17
16	S	694	4765	±	340	4 600			1.04
19	K	530	29030			29 030			1.00
20	Ca	532	14700	±	740	15 270	±	458	0.96
25	Mn	495	70	±	11	75.9	±	2.3	0.92
28	Ni	550	2.55	±	2.26	2.14	±	0.11	1.19
30	Zn	554	86	±	19	82	±	3	1.05
37	Rb	395	13.5	±	13.9	13			1.04
38	Sr	397	34	±	21	55.6	±	1	0.61

Table 2.12: PIXE analysis of the SRM 1570a Spinach Leaves, the distance between the detector and the target was 3.75 cm. Remarks to [1],[2],[3] are explained in Table 2.9.

Discussion of the PIXE analysis of the SRM thin samples

Because the samples were handled as thin, the GUPIX results of the analysis were given in $[ng/cm^2]$, while the SRM nominal values are listed in $[\mu g/g]$. Therefore, recalculation to the $[\mu g/g]$ units was performed with the help of potassium K concentration – we have chosen the element with high concentration in all four selected standards.

The concentration for many elements is very satisfactory when compared to the nominal values, even for those trace elements with very low concentration. However, the accuracy for many elements is not the best, the standard deviation reaches for some elements 100 %, those elements were discarded from the presented results. The standard deviation has increased mostly for elements contained in the backing carbon tape, see page 51. Although we were satisfied with the very low amounts of elements contained in the carbon tape, when compared e.g. to Mylar foil on page 45, it has turned out, that the elemental concentration of e.g. Mn, Fe, Cu, Zn in some of the standards is only a few times higher or comparable. That is why by the subtraction of the elemental concentrations of the carbon tape from the measured values, the precision of the results and their accuracy were deteriorated. Even though the concentration of the element in the sample as well as in the carbon tape were determined with an error smaller than 10 %, the subtraction of the element amount in the carbon tape brings then large error of 60 % and more. Therefore, another backing material must be found for next measurements of powder samples.

Another effect, which could influence the results, is the thickness of the carbon tape and therewith connected the need for handling the analysis as of an intermediately thick sample, which was mentioned in section 2.1.2 on page 13. Since this approach is very demanding, we have decided to analyze the samples as thin and see, if the results are in agreement with the SRM nominal values. Since the results are matching well the SRM values, we can conclude, that it was justifiable to handle the sample as thin.

Some features and characteristics of the PIXE analysis can be shown on the presented results. The PIXE results are not reliable for elements like Si, S, P because of the protecting foil, which stops more than 90 % of X-rays with energy lower than 2.5 keV, see Figure 2.12.

From this PIXE analysis of Spinach Leaves, we can also conclude, that there is indeed not even a trace amount of iron. In biological materials, which contain large amount of Ca, we can also expect some trace amount of Sr, because Sr has similar chemical characteristics as Ca and it can be bound the same way e.g. to bones or teeth (Williams et al., 2002).

From the experience with the GUPIX analysis it is known, how difficult it is to obtain correct amounts of trace elements with X-ray peaks close to some peak of a major element. As an example, Mn (Z=25) and Co (Z=27), close to a major amount of iron peak Fe (Z=26) in the sample can be described. The shape of the large X-ray peak of iron makes it difficult to distinguish between its low energy tail and the correct net area of Mn K_α and K_β peaks. The K_β peak of Mn (E_X = 6.49 keV) is covered by the Fe K$_\alpha$ peak (E$_X$ = 6.40 keV). The K$_\alpha$ of cobalt peak (E$_X$ = 6.93 keV) is overlapped by Fe K$_\beta$ (E$_X$ = 7.06 keV), so the net area of Co K$_\alpha$ peak is more or less impossible to determine, therefore Co K$_\beta$ net area is used instead. In Table 2.9 and 2.10, the cobalt amount is determined by PIXE incorrectly and with very large error. The determination of the Mn amount in all four SRM samples was satisfactory, however, the major amount of Fe does not agree with the nominal values in case of the SRM 1646a Estuarine Sediment (see Table 2.10).

All four SRM materials were measured also by the PGAA technique, which is described in chapter 3. As a comparative example, the results of PIXE and PGAA analysis of SRM Coal Fly Ash 1633b together with the nominal values given by NIST are listed in Table 4.1 and discussed in section 4.4. The Table 4.1 or its graphical demonstration in Figure 2.23 gives a brief example when PIXE and PGAA methods are competitive, and when they are complementary techniques. The PGAA analysis of the 1633b Coal Fly Ash sample, which was pressed to a pill of 0.5 g and measured for 6 hours, was performed by our group at PSI in 2001 (Baechler, Kudejova et al. (2003)).

2.4.4 Thick samples

For the analysis of thick samples by GUPIX, it is necessary to know the sample matrix composition. Therefore, first matrix analysis is performed by GUPIX: matrix density can be entered and the chemical compounds of matrix elements with elements invisible for PIXE like C, O, F are estimated. So, the matrix characteristics of the thick sample is created as an input to perform a trace analysis of the sample. The charge deposited to the sample is measured by sweeping the proton beam on the collimator and measuring the collimator to Faraday Cup ratio with an empty target position.

Salt crystals of different colours

As an example, three different NaCl crystals were measured, because the matrix composition and density of salt is well defined, and the surface of the crystals was very flat. All three pieces of salt crystals are coming from the Himalaya region and their colour was white, pink and red, what was indicating to different trace elements. The pink and white salt samples were cut from the same one larger salt stone. Starting with the pink salt, we have obtained the amount of Cl and invisible element Na with oxidation number +1 from the matrix calculation and then we have continued with the determination of the trace elements. This procedure was repeated for the next two salt samples.

The trace elements measured and analyzed in all three salt crystals are presented in Table 2.13 and also compared in Figure 2.25. The exact amount of Cl in a pure NaCl is 60.66 % of weight units (w.u.), Na has the rest of 39.34 %. As already discussed in the section 2.4.3, the Cl line is measured already with less precision because of the transmission of protecting Makrofol foil which lets through only about 17 % of the

Element	H-value $[10^{-5}]$	Pink salt $[\mu g/g]$	Red salt $[\mu g/g]$	White salt $[\mu g/g]$
S	694	-	2225 ± 882	-
Cl [%]	694	58.9 ± 3.0	54.8 ± 2.8	56.4 ± 2.9
K	530	2420 ± 130	994 ± 55	436 ± 31
Ca	532	1635 ± 84	125 ± 13	111 ± 13
Fe	495	11.9 ± 2.3	464 ± 24	318 ± 17
Zn	554	-	4.2 ± 1.7	-
Br	390	98 ± 9	106 ± 9	111 ± 10
Sr	397	47.9 ± 9.8	11.2 ± 6.2	-

Table 2.13: Comparison of trace elements in differently coloured salt crystals. The amount of matrix element chlorine determined by GUPIX is close to the expected 60.66 %.

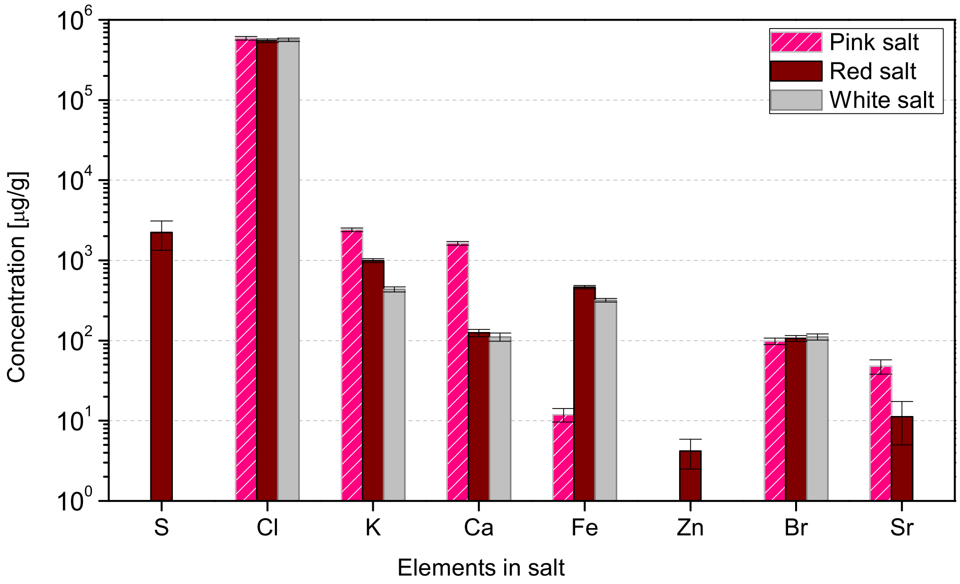

Figure 2.25: Comparison of matrix (chlorine) and trace elements in salt crystals of different colours.

Z	Element	H value $\cdot 10^{-5}$	PIXE [$\mu g/g$]	PGAA [$\mu g/g$]	PIXE to PGAA
1	H			2148 ± 41	
11	Na			973 ± 76	
12	Mg			127400 ± 6700	
13	Al			13040 ± 440	
14	Si	694	331800 ± 72300	136700 ± 3700	2.43
16	S	694	1400 ± 170	6110 ± 190	0.23
17	Cl	693	396 ± 75	94.8 ± 5.9	4.18
19	K	530	197 ± 22	170 ± 43	1.16
20	Ca	532	12260 ± 620	13400 ± 510	0.91
22	Ti	488	606 ± 33	759 ± 76	0.80
23	V	493	56.2 ± 8.7		
24	Cr	498	2850 ± 140	3337 ± 97	0.85
25	Mn	495	1315 ± 70	1362 ± 29	0.97
26	Fe	499	22600	22600 ± 4800	1.00
28	Ni	550	8680 ± 440	5070 ± 140	1.71
29	Cu	503	296 ± 24		
30	Zn	554	54 ± 12		
33	As	456	16 ± 12		
75	Re	523	330 ± 54		

Table 2.14: Comparison of the Allende 2 composition measured by the PIXE set-up at IKP and by the PGAA facility at BNC in Budapest. The PIXE results are normalized to the concentration of iron given by the PGAA measurement.

incoming Cl K_α X-rays. Therefore we did not obtain exactly the expected 60.66 % but little less.

Allende meteorite

The Allende meteorite is shortly described in section 3.4.2 and shown in Figure 3.11, since the main task was to analyse the heterogeneous grainy small piece of meteoritic stone, called Allende, by the PGAA method. One of the three pieces of Allende, marked Allende 2 was also measured by the PIXE method, the proton beam was again swept onto its surface, irradiating an area of about 5 mm in diameter. The aim of this PIXE experiment was to compare the results with the PGAA analysis of the sample bulk performed at the Budapest Neutron Centre, BNC. From the comparison, we wanted to draw conclusions, how reliable the PIXE measurement of a bulk heterogeneous sample with rough surface is.

The comparison between the PIXE analysis and the PGAA bulk analysis is shown in Table 2.14 and in Figure 2.26. We can see, that there is a larger disagreement for the determined concentration of many elements by the PIXE and by the PGAA

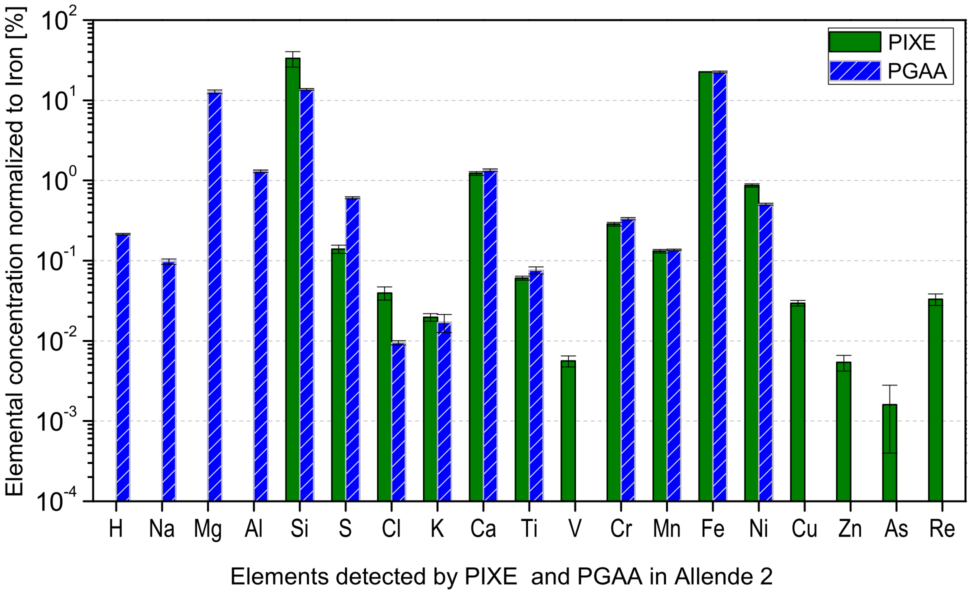

Figure 2.26: PIXE analysis of the surface of a thick sample Allende 2 compared to the PGAA analysis of the Allende 2 sample bulk performed in Budapest in 2003. The PIXE results are normalized to the concentration of iron given by the PGAA measurement.

analysis. We can deduce, that the irradiated surface of the Allene 2 by the proton current was too heterogeneous and the surface was too rough and coarse to obtain reliable results of the overall elemental concentration.

Green Glass

As a third example, a "Green Glass" sample made from coloured stained glass (Tiffany technique) with rather complicated spectrum was analysed as a thick sample, see Figure 2.27.

The density of the sample is not known. This Green Glass shred originates from the beginning of the 20^{th} century and it can give information, which elements were used to colour the glass at that time. Since the surface of the Green Glass is sufficiently flat, the sample is well suited for a thick sample analysis in ideal conditions. On the other hand, thanks to the visible change of colours on the surface from light green to dark green, it was apparent, that the sample is not ideally homogeneous. By sweeping the beam to an area of about $5\,\mathrm{mm}^2$ in diameter we have obtained an averaged elemental composition of the surface. Moreover, we have chosen this Green Glass sample as a good candidate for testing the scanning ability of the PIXE instrument and we have determined the 2D surface distribution of selected elements, see below in section 2.4.5.

This sample was also analysed for the bulk composition by the PGAA method

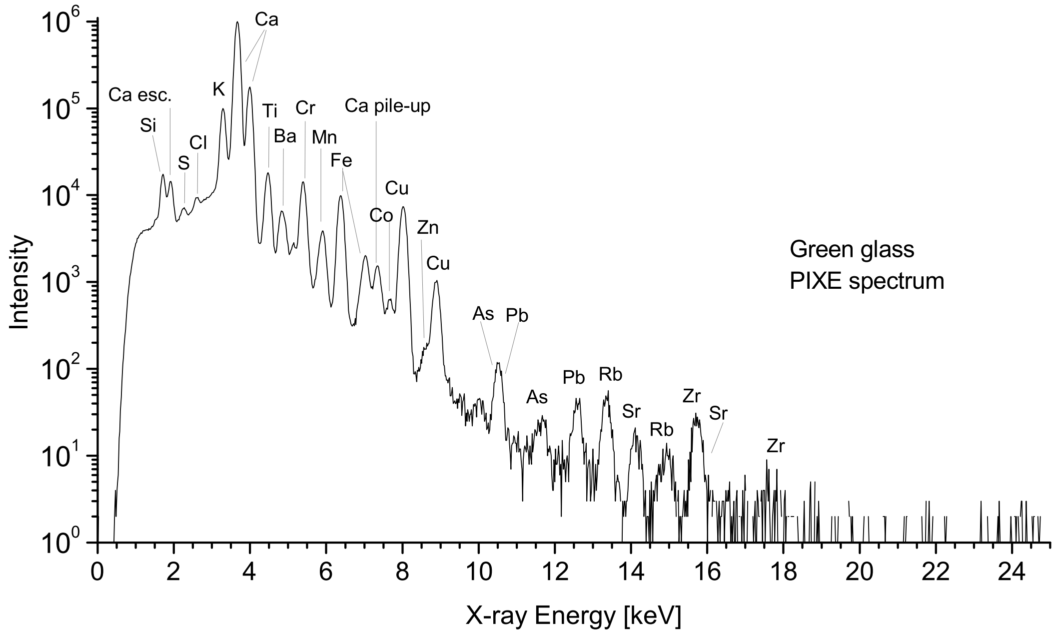

Figure 2.27: PIXE spectrum of the Green Glass sample.

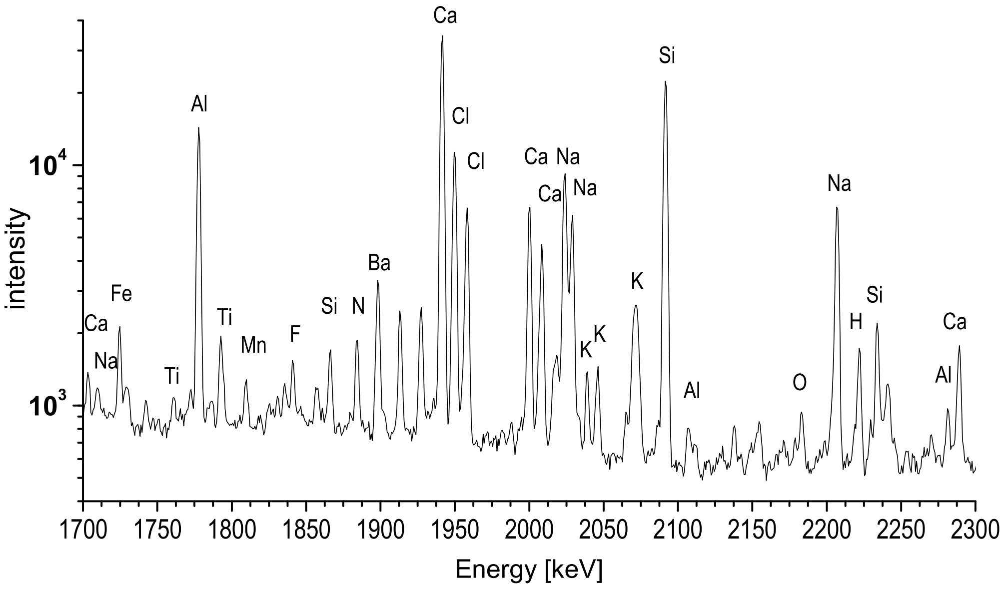

Figure 2.28: A part of a PGAA spectrum of the Green Glass sample measured with the PGAA facility at BNC, Budapest in 2004.

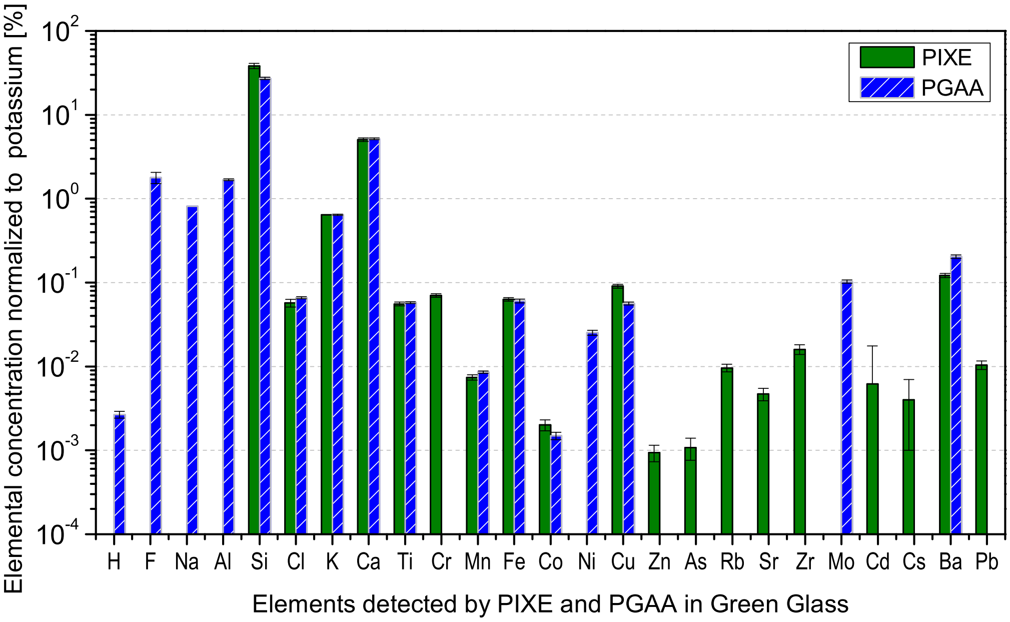

Figure 2.29: PIXE analysis of the surface of a thick sample Green Glass compared to PGAA analysis of the Green Glass sample bulk performed at BNC in Budapest in 2004.

in Budapest in 2004, therefore we can make a comparison of the surface and volume analysis of the same sample. The results are listed in Table 2.15 and in Figure 2.29.

When the matrix of the sample was determined, we have used the PGAA analysis from Budapest to include the invisible elements: O[6], F, Al. Since the major component of glass is Si, which is not reliably analysed by our PIXE instrument, we will not rely on the determined amount of Si in the sample. After the matrix was defined, the trace analysis was performed with the results, listed in Table 2.15 and compared to PGAA results from Budapest, 2004. For comparison with the PGAA results from Budapest, we have normalized the results to the elemental concentration of potassium, since we have used this element also for the normalization of the SRM standards. Elements Cl, K, Ca, Ti, Mn, Fe and Co give approximately the same concentration by both methods, elements Cu, Cd and Ba are very different. This could be mainly caused by the heterogeneous surface of the green glass sample, because as we will see later, the dark green colour is linked to higher amount of e.g. Cu and Cr. We have not found Ni by the GUPIX analysis of the PIXE spectrum, which could be caused by the overlap of a small Ni peak (K_α-line $E_X = 7.48$ keV) with a larger pile-up peak of Ca ($E_{PU} = 3.69$ keV $+$ 3.69 keV $= 7.38$ keV).

---

[6] The amount of Oxygen in the PGAA samples at BNC is usually determined by the evaluation of oxides of the visible elements – Na, Al, Si, S, K, Ca, Fe, …

Z	Element	Pixe[1] $[\mu g/g]$			PGAA[2] $[\mu g/g]$			PIXE to PGAA
1	H	-			26.7	±	2.5	
9	F	-			17860	±	2700	
11	Na	-			81200	±	1400	
13	Al	-			16830	±	360	
14	Si	383200	±	29100	271900	±	8500	1.41
17	Cl	572	±	59	659	±	20	0.87
19	K	6426			6426	±	128	1.00
20	Ca	50600	±	2530	51870	±	1360	0.98
22	Ti	555	±	29	577	±	12	0.96
24	Cr	701	±	35	-			
25	Mn	73.9	±	5.3	85.6	±	2.9	0.86
26	Fe	632	±	32	604	±	32	1.05
27	Co	20.1	±	3.0	14.9	±	1.5	1.35
28	Ni	-			253	±	17	
29	Cu	904	±	46	563	±	24	1.61
30	Zn	9.4	±	2.1	-			
33	As	10.8	±	3.2	-			
37	Rb	96	±	10	-			
38	Sr	47	±	8	-			
40	Zr	160	±	21	-			
42	Mo	-			1027	±	47	
48	Cd	-			0.09	±	0.01	
55	Cs	40	±	30	-			
56	Ba	1218	±	69	2037	±	102	0.60
82	Pb	104	±	12	-			

Table 2.15: Green Glass surface composition analysed by the PIXE analysis and compared to the sample bulk analysis determined by the PGAA technique at Budapest in 2004.

[1] The concentrations determined by PIXE were normalized to the potassium concentration determined by the PGAA analysis in Budapest.

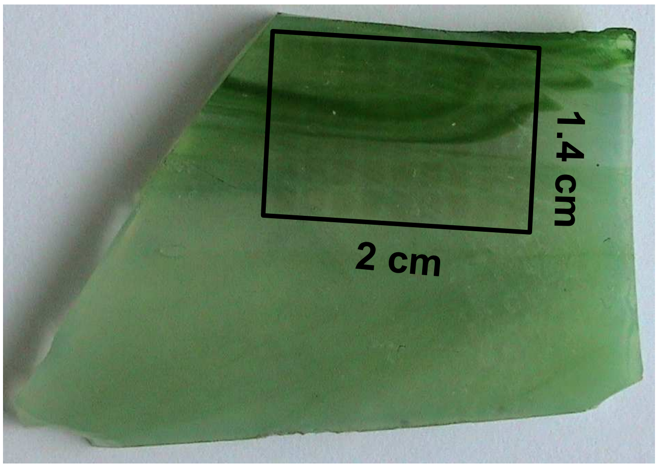

Figure 2.30: Green Glass sample picture with visible dark green colour distribution. On the sample, the scanned area is marked with the rectangle. The surface of the proton beam by scanning was $1 \times 1\,\mathrm{mm}^2$, 54 positions were measured for 20 times 1 second.

2.4.5 Scanned sample

The Green Glass analysed as a thick sample by PIXE and by the PGAA method in Budapest, forms a very interesting sample for the scanning of its surface. We can see on the picture in Figure 2.30 that the surface of the Green Glass in not homogeneously coloured and we wanted to find out, if the colour distribution corresponds to some elemental distribution. The sample area, which was scanned is also marked in Figure 2.30.

We have chosen a rectangular part of $20 \times 14\,\mathrm{mm}^2$, on which the proton beam (focused to $1 \times 1\,\mathrm{mm}^2$) scanned the surface by 9 steps in the horizontal and 6 steps in the vertical direction. Each position was measured twenty times for 1 s to compensate for a possible proton beam instability. For the analysis, we have chosen these elements of interest: K, Ca, Ti, Cr, Fe and Cu. During the measurement, the detector was at 55 mm from the centre of the sample, looking from 45 ° at the target in the horizontal direction. Concerning the vertical direction, the detector was on the vertical axis passing through the sample middle (0 ° in vertical direction), see e.g. Figure 2.6 or 2.7.

For each element Z, we have obtained a 2D matrix of intensities at each measured position $A_Z[x, y]$. These $A_Z[x, y]$ were then corrected for the detector efficiency ϵ (E_γ), fluorescence yield for each energy ω_Z, b_Z^α branching ratio for K_α-line and transmission T_X through the 107 μm thin Makrofol foil. Finally, the values were corrected to the geometry between the detector and sample and normalized to the [0,0] position, which corresponds to the middle of the sample. The obtained values can then be compared to each other and the geometrical factor is eliminated. Because we were interested

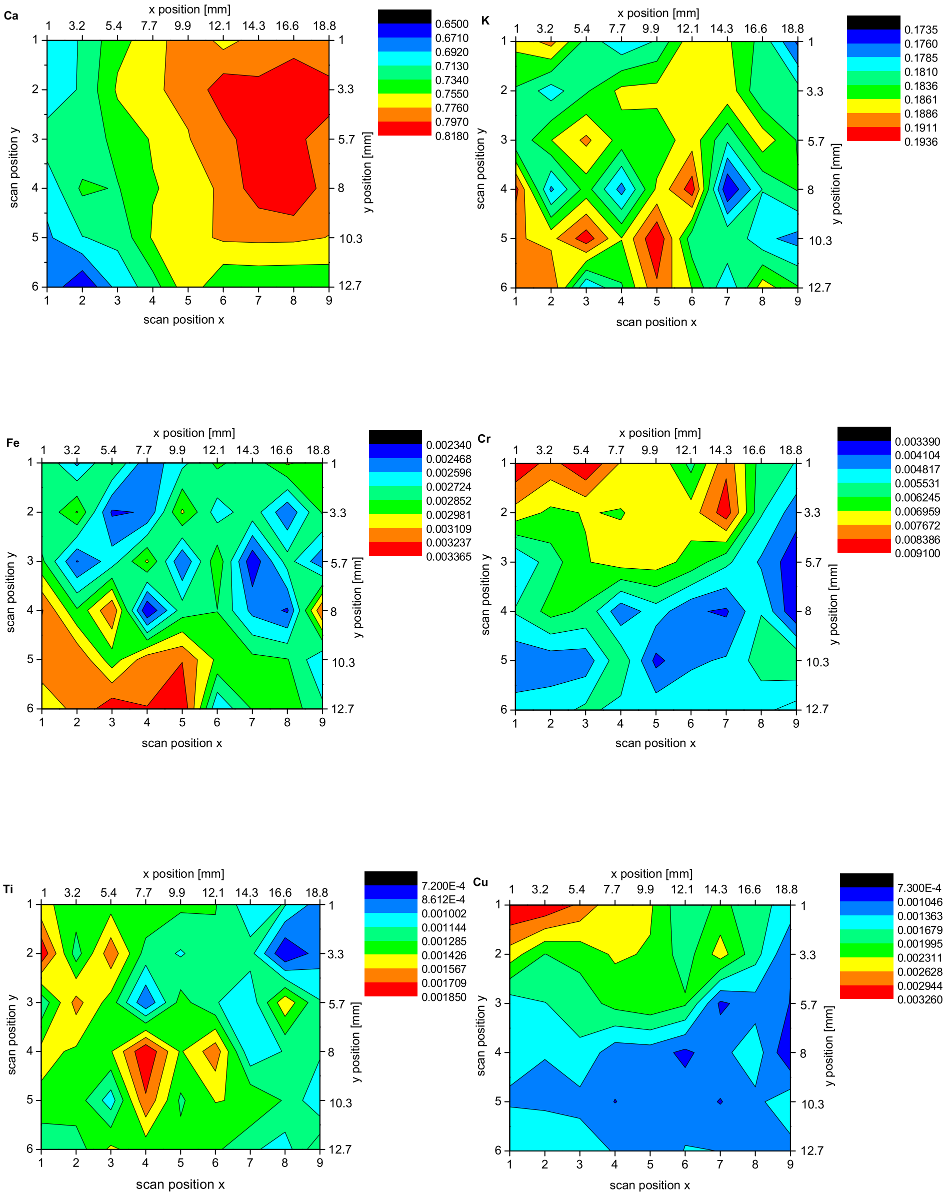

Figure 2.31: Scan of the green glass. Elements K, Ti, Cr, Fe and Cu are normalized to the concentration of Ca at each measured position. When compared to the photo of the scanned part of the Green Glass, the higher intensity of Cr and Cu correspond to the darker green stripe at the Green Glass shred.

in the relative intensity of the chosen elements, we have taken the very stable Ca intensity distribution as a base and normalized all other elements to it (that means the intensity $A_Z[x, y]$ of Z = K, Ti, Cr, Fe and Cu was divided in each point $[x, y]$ of the scanned matrix by the corresponding intensity of Ca at that point – $A_{Ca}[x, y]$). In Figure 2.31, these relative concentrations of K, Ti, Cr, Fe and Cu are presented and the determined Ca intensity taken as a base is shown for comparison.

If we compare the photo and the intensity distribution of the elements in the scanned part of Green Glass, we can see correlation between the dark green colour and Cr as well as Cu distribution. Cu is usually connected with the green colour, so this correlation is not a surprise.

2.5 PIXE Conclusions

We have built a new reliable PIXE installation at the Pelletron Accelerator of the IKP, University of Cologne. The PIXE set-up is automated for a measurement of a set of 24 samples in one run. For thin samples, the proton current is normalized by the Faraday cup and collimator, for thick samples, the current on the collimator is employed and the reliability is checked by the measurement of empty targets. With the scanning device, we can perform macro-scanning of sample surface up to $6 \times 6\,\mathrm{cm}^2$ with a beam collimated to $1 \times 1\,\mathrm{mm}^2$. Because we can perform the PIXE experiments only in vacuum, our PIXE set-up is not arranged for sample larger than a cube of $20 \times 15 \times 10\,\mathrm{cm}^3$. Our PIXE installation is well prepared also for thin aerosol samples for air pollution measurement. The PIXE chamber is arranged very flexibly so we can perform at the same time PIXE and PIGE analysis, and in the near future, the RBS surface barrier detector will be mounted and all three techniques will run in parallel.

For the detection of X-rays, mainly a small Peltier-cooled XFlash detector is used, which has the advantage of its counting capability up to 300 kcps. The data acquisition is performed using digital electronics with a system based on DGF-4C modules from X-ray Instrumentation Associates (XIA) and an in-house developed acquisition software. The digital electronics brings an advantage for parallel acquisition of more signals at the same time – only one DGF-4C module can be employed for data acquisition of 4 different detectors. The calibration of our PIXE instrument was performed with 20 thin MicroMatter standards and with the analysis by the GUPIX program, a set of H values for both K- and L-lines and different distances were derived and employed for the sample analysis. The reliability of the absolute analysis is constrained by the lower threshold at about 2 keV, caused by the transmission of X-rays through the 107 μm Makrofol foil, which allows only 1% of X-rays with 2 keV energy to pass through the foil. The analysis of the PIXE spectra is then processed with the GUPIX program.

The analysis of the PIXE data was initially tested with homogeneous powders of Standard Reference Materials with known and certified composition prepared as thin samples. For many elements, the analysis is satisfactory and agrees within the standard deviation with the certified values, however, there is still some work to be done on characterization of the detectors to get better agreement also for other elements. One possibility of the improvement consist in a careful fitting of pure element spectra, which employs also the low-energy tailing functions and then to build the parameters into the description of the XFlash and Si(Li) detectors in the GUPIX program. Another improvement can be to change the detector parameters given by the manufacturer slightly and see, if the H values tend to align themselves to a constant line as a function of energy. We have performed such lengthy tests of changing the detector parameters and we have observed significant difference in the H values only when the thickness of the protecting foil was virtually decreased to about 91 μm.

The Si(Li) detector is fixed at a distance of 4.2 cm from the target position and when compared to the Xflash detector, it brings the advantage of good efficiency for detection of X-rays with higher energy (up to 40 keV).

Future work at the IKP of the University of Cologne has to be now directed toward improving the accuracy of the PIXE measurement and of the data analysis. Our aim is to obtain a better agreement of the PIXE results with standard reference materials of diverse matrices for thin as well as for thick samples. Then we plan to design a new chamber for PIXE applications filled with helium or at low vacuum for bigger samples or samples, which can not be analyzed in high vacuum. In the near future, we intend to extend the PIXE chamber set-up by the RBS detector and take advantage of our 10 MV pelletron accelerator, which can accelerate heavy ions, too. With heavy ions we could perform interesting RBS experiments, which are not possible with the small accelerators used for standard IBA experiments.

Chapter

3

PGAA

For many samples of interest in e.g. archeology, geochemistry or material science, it is necessary to make not (only) the surface analysis of a given sample but an analysis of the bulk. For non-destructive bulk measurements, usually Instrumental Neutron Activation Analysis (INAA) is taken as a standard method. Another very efficient method for a bulk analysis is Prompt Gamma-Ray Activation Analysis, which uses – as well as INAA – neutrons to determine the isotopic, elemental or chemical composition of the sample. We will explain and discuss the PGAA method, its benefits and weaker points. Since the INAA method is already well-established, we will compare the PGAA to INAA and make some decisions, when it is better to use PGAA instead of INAA. We will show some convincing results of the analysis of meteorites and geological samples and standards measured with the PGAA facility at the BNC, Budapest. Some of the sample analysis have been already compared in last chapter with the results obtained with our PIXE installation at the Nuclear Physics Institute (IKP), Cologne. We will dedicate one part of this chapter to the design and construction of the new PGAA station at the new research reactor FRM-II at Garching by Munich, Germany. We will outline our plans and simulations of important parameters for the PGAA at FRM-II. Then, we will discuss our results and draw some important conclusions.

3.1 Introduction

Neutrons are particles with no electric charge and therefore they can travel easily through matter. Since they undergo no Coulomb interaction, they are not stopped already in the material surface layer like electrons or protons (e.g. PIXE analysis) and other charged particles and therefore they can be used for the analysis of the sample bulk. Slow neutrons ($E_n \leq 1$ eV) interact with most elements by the (n,γ) reaction, in which the neutron is captured by the nucleus of the target material. As the newly formed nucleus is usually in an excited state, γ-rays which are characteristic to the newly formed nucleus are emitted. The measurement of those γ-rays then allows to identify the elements and isotopes in the sample. This is the principle of the Prompt Gamma-Ray Activation Analysis.

From the experimental point of view, PGAA is a multi-elemental non-destructive method for determination of major, minor and trace elements in the entire volume of the sample. The sample can be not only solid, but also liquid or gas in a vial from appropriate material (mostly Teflon). Usually no special chemical preparation of samples is needed.

In general, PGAA is an effective nuclear technique for the quantitative determination of H, B, Na, Cl, K, Sc, Ti, V, Cr, Mn, Fe, Co, Ni, Cu, As, Se, Br, Sr, Mo, Ag, Cd, In, Xe, Cs, Hf, Ta, Re, Os, Pt, Au, Hg, Nd, Sm, Eu, Gd, Dy, Er and U. The limits of detection for these elements vary between 1 ng/g for Gd and 100 μg/g for Ti. PGAA can also detect practically all the other elements, but with limits of detection already of the order of hundreds of μg/g up to percent (e.g. for C, N, O, F, Sn, Pb and Bi).

Solid samples for the PGAA measurement have usually masses in the range of 0.5 g up to 20 g. Depending on the amount of the investigated sample, sample matrix and the elements of interest, the limit of detection (LOD) for a good quality PGAA installation can reach 10 ng/g (e.g for B, Sm, Gd). PGAA is an eligible complementary method to Instrumental Neutron Activation Analysis (INAA) for detection of light elements like H, Li, B, C, N, O, F or P and competitive for S and heavy elements like Cd, Gd, Tl, Pb and Bi. It is a powerful tool for archaeological and geological investigations, helpful in nuclear industry, material science, biology, medicine and in other research fields.

PGAA is a sole and very sensitive non-destructive technique for determination of small amounts of boron in solid and liquid samples (units of ng/g), therefore lots of effort is put to keep the surroundings of the PGAA instrument boron-free and enable the lowest possible limit of detection for boron. Another unquestionable eligibility of the PGAA is the very easy detection of hydrogen in the sample bulk (units of μg/g).

3.2 PGAA principle

cold and thermal neutrons

The neutron spectrum is usually divided – not very strictly – into three intervals: fast neutrons with the energy $\mathrm{E}_n \geq 1$ MeV; neutrons with an intermediate energy E_n between 1 eV and 1 MeV and slow neutrons with energy $\mathrm{E}_n \leq$ 1eV. The slow neutrons are then subdivided to epithermal neutrons (100 keV $\geq \mathrm{E}_n \geq$ 0.025 eV); thermal neutrons E_n=0.025 eV; cold neutrons (25 meV $\geq \mathrm{E}_n \geq$ 0.05meV); very cold neutrons (0.05 meV $\geq \mathrm{E}_n \geq$ 0.0002 meV) and ultra cold neutrons with $\mathrm{E}_n \leq 2\cdot10^{-4}$ meV. This division of neutrons according to their energy is graphically displayed in Figure 3.1.

cold neutron energy vs. wavelength

For cold neutrons the non-relativistic approximation of the de Broglie equation can be used:

$$\lambda = \frac{hc}{pc} = \frac{hc}{\sqrt{2E_{kin}m_0c^2}} \tag{3.1}$$

If we take $hc = 1239.84\,\mathrm{eV}\cdot\mathrm{nm}$ and the neutron kinetic energy E_{kin} in [eV] as well as the neutron mass $m_0c^2 = 939.6\cdot10^6\,\mathrm{eV}$, then the wavelength λ will be directly

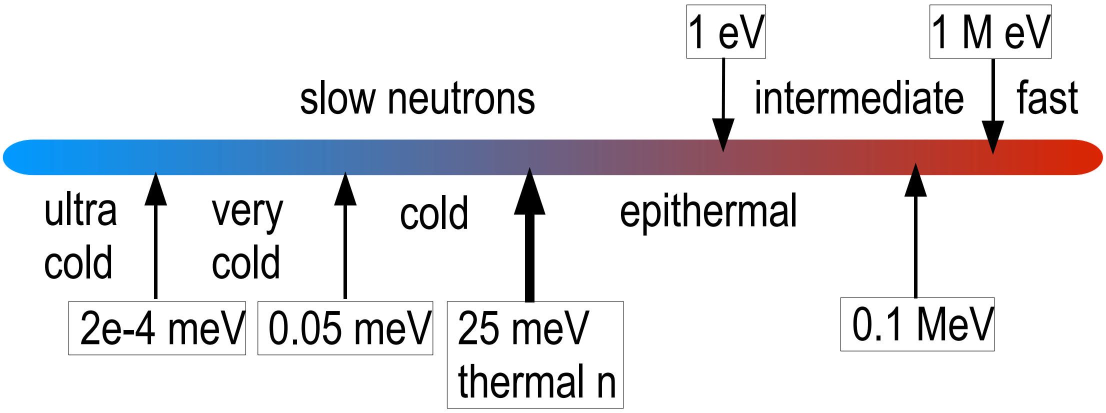

Figure 3.1: The neutrons are divided into three main intervals according to their energy. The interval of slow neutrons is then subdivided into five intervals, where the thermal neutrons have defined energy of 25 meV, which is a mean energy of a neutron in thermal equilibrium with its surroundings at 20 °C (Byrne, 1995).

expressed in [nm]. Table 3.1 shows some examples of kinetic energy and corresponding wavelength and velocity of a slow neutron.

3.2.1 Description of the PGAA technique

In principle, PGAA is based on the capture of thermal or, in better cases, of cold neutrons by a target material, as outlined in Figure 3.2. The capturing nucleus ^{A}Z forms a compound nucleus mostly in excited state $^{A+1}$Z* and de-excites promptly (withing 10^{-14}s) by emitting prompt γ-rays. These γ-rays, characteristic to the particular isotope $^{A+1}$Z, are then detected by a Compton suppressed γ-ray spectrometer. Therefore, the PGAA analysis is performed online during the sample irradiation. If the prompt γ-rays are ignored for the analysis (see Figure 3.2) the formed nucleus $^{A+1}$Z is usually not stable and decays by emitting β^-, β^+ or α particle with a half-life characteristic for the formed nucleus $^{A+1}$Z followed by consequent de-exciting γ-rays. These γ-rays, electrons or positrons are measured by so-called delayed neutron activation analysis, shortened to standard Neutron Activation Analysis, NAA.

NAA, in contrast to PGAA, takes place after the sample irradiation, which strongly improves the background conditions and sensitivity of the method. If the sample is measured after the irradiation without any chemical manipulation, the particular NAA method is non-destructive and called Instrumental Neutron Activation Analysis (INAA). To achieve better sensitivity for some particular elements, they must be chemically separated from the irradiated sample before the measurement, this method is then called Radiochemical Neutron Activation Analysis (RNAA) and is destructive.

energy		wavelength		velocity
0.5 meV	~	12.7 Å	~	$308\ \mathrm{ms}^{-1}$
1 meV	~	9.0 Å	~	$436\ \mathrm{ms}^{-1}$
2 meV	~	6.1 Å	~	$616\ \mathrm{ms}^{-1}$
3 meV	~	5.2 Å	~	$755\ \mathrm{ms}^{-1}$
4 meV	~	4.5 Å	~	$872\ \mathrm{ms}^{-1}$
5 meV	~	4.0 Å	~	$975\ \mathrm{ms}^{-1}$
7 meV	~	3.4 Å	~	$1150\ \mathrm{ms}^{-1}$
25 meV	~	1.8 Å	~	$2200\ \mathrm{ms}^{-1}$
50 meV	~	1.3 Å	~	$3080\ \mathrm{ms}^{-1}$
100 meV	~	0.9 Å	~	$4360\ \mathrm{ms}^{-1}$

Table 3.1: Examples of the kinetic energy, corresponding wavelength and velocity of a slow neutron.

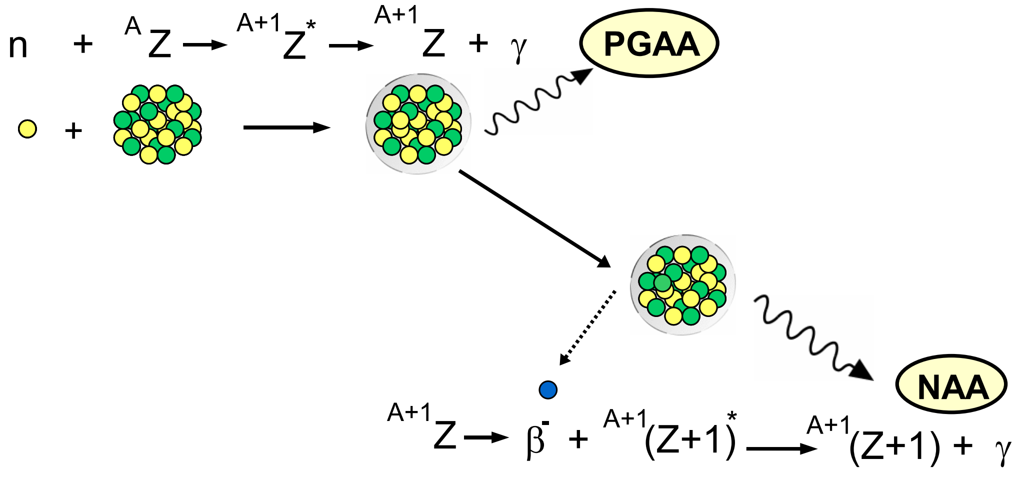

Figure 3.2: Schematic representation of the neutron capture reaction and subsequent detection of prompt γ-rays for PGAA as well as delayed γ-rays for NAA analysis.

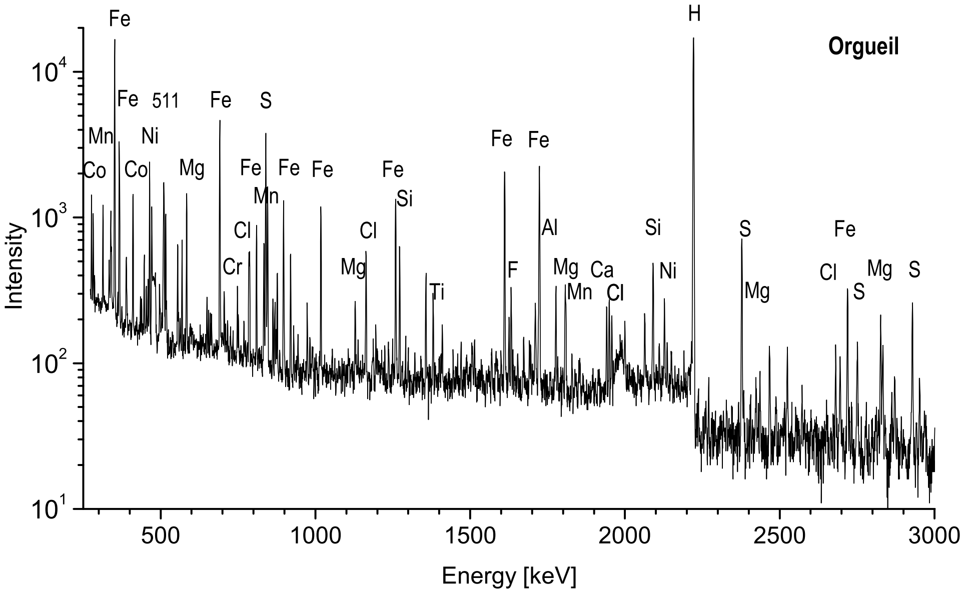

Figure 3.3: A part of a PGAA spectrum of the Orgueil meteorite (232 mg) acquired with a Compton suppressed γ-ray spectrometer. The sample was measured for 16500 s at the PGAA facility in Budapest in 2003.

In the thermal and lower neutron energy range the probability of neutron capture increases almost linearly with decreasing velocity v of the neutron:

$$v \cdot \sigma = v_0 \cdot \sigma_0 \tag{3.2}$$

where σ is the neutron capture cross-section at the velocity v and σ_0 is the thermal neutron capture cross-section at the velocity $v_0 = 2200\,\mathrm{ms}^{-1}$ or at neutron energy of 25 meV.

This rule is valid for nearly all elements; exceptions are e.g. Cd, Sm, Eu and Gd, so-called “strong non-1/v elements” with first neutron resonances in the epithermal neutron energy region close to the thermal energy (Mughabghab et al., 1981, 1984).

After neutron capture the promptly emitted γ-rays are detected by a Compton-suppressed spectrometer. The Compton-suppression provides a considerable reduction of the background in the acquired spectrum by rejecting those events, in which a Compton scattered γ-ray escape the HPGe detector. The effort to keep the background at minimum is intensified by a proper shielding of the whole PGAA instrument. The PGAA spectrum usually ranges from 50 keV up to 11 MeV and is very complex – the number of characteristics γ-peaks of all included elements can go to thousands. Usually 2 – 5 most intensive peaks for each identified element are chosen for a subsequent quantitative analysis. Figure 3.3 presents a part of the PGAA spectrum of a homogeneous powder of the Orgueil meteorite acquired by a Compton suppressed spectrometer at the PGAA facility at Budapest, 2003. The sample was measured for

16500 s and its mass was 232 mg.

3.2.2 PGAA data analysis

For each element Z, the net area A_{z,E_γ} of the particular peak E_γ (after subtraction of the proper background contribution from the spectrum) is proportional to the mass of the element m_z in the sample, the neutron flux Φ_n in neutrons/cm$^2 s$, the length of measurement t, the neutron capture cross-section $\sigma_z(E_n)$ considering the $1/v$ law (see formula (3.2) above), the isotopic abundance Θ_z of the particular γ-ray emitter, the counting efficiency of the detector $\epsilon_{ef}(E_\gamma, \Omega)$ at the corresponding γ-ray energy E_γ and the probability Γ_{γ,E_γ} of emitting particular γ-ray for one neutron capture by particular isotope of the element Z. This all assuming a constant geometry (the solid angle Ω is kept), no self-shielding of the neutron flux and γ-rays and a homogeneous neutron flux. Then we can write:

$$A_{z,E_\gamma} = \frac{N_A m_z}{M_z} \Phi_n \sigma_z(E_n) \Theta_z \Gamma_{\gamma,E_\gamma} \epsilon_{ef}(E_\gamma, \Omega) t \tag{3.3}$$

where N_A is Avogadro's number and M_z is the atomic weight. This approach allows to determine absolutely the mass m_z of the particular element in the sample under the assumption of ideal measuring conditions and a good knowledge of all the theoretical constants in (3.3). Unfortunately, this is not the real case, as mostly the relevant constants are not given with sufficient accuracy. Therefore, the PGAA laboratories prefer relative methods. In that case, a standard material with known composition and matrix characteristics similar to that of the samples of interest is chosen. The net-peak areas A_{z,E_γ} of elements in the measured samples are then compared to those corresponding of the standard material and particular masses m_z (or concentrations c_z) of elements Z are determined in this way. This method is also demanding and time consuming, moreover, it is not always easy to find proper standardized material. Therefore, the so-called k_0 method was developed for the PGAA analysis, following the example of INAA, where the k_0 method is used already for a long time and simplifies considerably the sample analysis. The k_0 method is now accepted and applied by the majority of the PGAA groups. Although, the precise detector efficiency calibration of each particular PGAA detector for given geometry is necessary, once this demanding procedure was made, the inquired elemental concentration in the unknown sample can be determined by the use of so-called k_0 values. The advantage of the k_0 values is their independence on the PGAA set-up, where they were determined. Because the k_0 method is so advantageous for the PGAA analysis, it will be explained in more detail later in section 3.2.4.

3.2.3 Correction effects for the PGAA analysis

In the ideal case, the explored sample can be treated as homogeneous and transparent for the incoming neutrons as well as for outgoing γ-rays. This is the situation, when the neutron flux density Φ_n does not appreciably change while passing through the sample and the number of γ-rays attenuated in the sample is negligible. This ideal case does never happen and so one needs to care about:

neutron self-absorption

The real situation is a little more difficult, if the sample matrix contains larger concentrations of elements with high neutron absorption cross-section; e.g. B, Cd, Eu or Gd. Then, a correction for neutron self-absorption in the sample must be taken into account and the neutron flux $\Phi(x)$ decreases exponentially while traveling through the homogeneous sample matrix of the thickness d:

$$\Phi = \Phi_0 e^{-\Sigma_a d} \tag{3.4}$$

where Φ_0 is the neutron flux before entering the sample and Σ_a is the total macroscopic neutron absorption cross-section.

neutron scattering

Another effect influencing the results of the PGAA analysis is the neutron scattering. Neutrons scatter with increasing probability – expressed by a macroscopic cross-section for neutron scattering Σ_s – on elements with decreasing proton number. Therefore, this effect is most relevant for neutron scattering on hydrogen, that means mostly neutrons scattered in liquids. Depending on the geometry of the sample, neutron scattering can either increase or decrease the sensitivity of the measurement. As an example, one can imagine a thin and a thick cylinder (bigger and smaller radius) of the same length put into the neutron flux along the z-axis. In case of the thin cylinder, neutrons can easily scatter out of the sample and the sensitivity decreases this way. Neutrons scattered the same way in the cylinder with larger radius are scattered into other parts of the cylinder, and the probability of the neutron capture is therefore increased by scattering in comparison with simple neutron passing through the sample without scattering (neutron transmission). The effects of neutron scattering in samples of different shapes and geometries were studied in detail e.g. by Copley and Stone (1989); Copley (1991); Mackey et al. (1991, 1992) or Paul and Mackey (1994).

neutron self-shielding

Both above mentioned effects are treated together as the neutron self-shielding effect. The self-shielding factor f is defined as the ratio of the average neutron flux in the sample $\overline{\Phi}$ to the incident neutron flux before entering the sample Φ_0 (Fleming, 1982):

$$f \equiv \overline{\Phi}/\Phi_0 \tag{3.5}$$

If we assume a monoenergetic parallel neutron beam and a small sample, where each neutron undergo either absorption (with Σ_a the macroscopic cross-section for neutron absorption) or scattering (with Σ_s the macroscopic cross-section for neutron scattering – the scattered neutron can not be absorbed in the sample any more), then the total cross-section for neutrons $\Sigma_t = \Sigma_a + \Sigma_s$ is relevant for the total self-shielding effect including also the neutron scattering. As an example of a self-shielding factor f for a slab of a thickness d with the help of the equations (3.4) and (3.5), we get:

$$f = \frac{1 - e^{-\Sigma_t d}}{\Sigma_t d} \tag{3.6}$$

The self-shielding factors for sphere and cylinder calculated with the same assumptions were also derived and discussed by Fleming (1982). The self-shielding factors f for different sample matrices can be also experimentally derived from the measurement of the neutron flux Φ transmission through the sample ($\Phi/\Phi_0 = \exp(-\Sigma_t d)$).

If the neutron self-shielding in the sample occurs, the sensitivity for element detection decreases. The effect of the neutron self-shielding in hydrogenous samples was studied e.g. by Blaauw and Mackey (1997).

gamma-ray self-absorption

If the sample consists of a dense material with a density ρ, then the created γ-rays are attenuated in the sample. The corresponding intensity of γ-rays I_0 is exponentially decreasing to intensity I depending on the energy E_γ and the length x, which the γ-rays must travel within the sample before reaching the detector:

$$I = I_0 e^{-\mu_x x} \tag{3.7}$$

where $\mu_x = \mu\rho$ is the attenuation coefficient (in cm^{-1}), ρ is the material density and μ is the tabularized mass attenuation coefficient (in $\mathrm{cm}^2\mathrm{g}^{-1}$) for various elements and materials. We have to make the correction for this γ-ray attenuation if necessary and since the path x between the γ-ray origin and the detector depends on the full volume of the sample part seen by the neutrons, we have to make an integration over it.

If both neutron self-absorption and γ-ray attenuation in the sample take place, we have to combine both effects, integrate over the full volume of the sample and find the corresponding correction coefficient.

In reality, the sample must not be homogeneous and some corrections for the matrix structure must be sometimes considered to correct the resulting concentrations of the elements. The problems bring heterogeneous samples with distributed grains of strong neutron-absorbers, like B, Cd, Gd or scatterers, like H. If the neutron flux Φ is not homogeneous, it can also contribute to a wrong analysis of elemental concentrations in heterogeneous samples.

All mentioned effect are more pronounced when using cold neutrons in comparison to thermal neutrons, as the absorption and scattering cross-sections increase with decreasing energy of the neutrons. Another effect influencing the analysis of the cold neutron PGAA is the temperature of the sample. It can affect the results of elemental concentrations, if the analysis was performed by absolute means (not comparison to an inner standard). Indeed, if the sample has a room temperature, the cold neutrons are warmed up by the scattering in the sample (the neutron spectrum is thermalized) and therefore the neutron capture cross-section decreases.

To reduce all the effects, which can make the analysis of non-ideal samples very difficult with respect to the above mentioned corrections as well as to the dependence on the fluctuations of the neutron flux, the comparative approach for the determination of the elemental concentrations is preferred by most of the PGAA laboratories. For special samples, corrections for neutron self-shielding and gamma self-absorption cannot be neglected also by the comparative approach (e.g. layered sample, heterogeneous sample with strongly absorbing parts) and therefore they must be taken into account for an accurate analysis, too.

3.2.4 k_0 method for the PGAA analysis

As discussed in the previous section 3.2.2, the analysis of the PGAA spectrum can be performed either absolutely or relatively. In relative approach it can be either with the help of a standard sample for comparison or as a ratio to an “inner comparator”, in which case only concentrations c_z of elements detected in the sample can be given (no total masses m_z). The determination of absolute masses m_z of elements Z in the sample analyzed by the comparative method can then follow in case, if mass of one of the detected elements was determined by other method absolutely or if all the elements of the sample were detected and quantified by the PGAA method and the sample mass is known. As discussed in 3.2.2, for the absolute PGAA analysis of a homogeneous sample (without an inner comparator), all the parameters in the equation (3.3) must be known.

For heterogeneous samples or for samples with high scattering cross-section for neutrons or for samples, which strongly absorb either neutrons or prompt γ-rays the situation is more complicated – as discussed in 3.2.3 – and some demanding corrections for the sample matrix should be included to obtain a correct elemental sample analysis. Therefore, the comparative k_0 method employing one chosen element from the sample itself as the inner comparator is preferred. The main advantage for this internal method is the fact, that the determination of the comparator mass m_c is affected by the same corrections-requiring effects in the sample as the other elements request and the matrix effects disappear by considering ratios. Another advantage of the comparative method should be mentioned: in case of the heterogeneous samples a larger bulk can be measured and a representative average of the elemental concentration will be obtained. Also in our case, the analysis of the PGAA experimental data is performed by the k_0 method. The comparative technique for the PGAA analysis was introduced by Lindstrom et al. (1992), well described and in detail discussed by Paul (1995) and Molnár et al. (1998), where the k_0 approach was experimentally developed and comparison of k_0 values between two laboratories (Budapest and NIST) was presented.

For two elements from one sample, element x and c - comparator, we will normalize the net-peak area A_x of the element x to the area A_c of the comparator. By employing the equation (3.3) and the assumption of equation (3.2) $\sigma = v_0 \cdot \sigma_0 / v$ for cold neutron energy E_n we obtain

$$k_{x,c} = \frac{A_x/m_x}{A_c/m_c} = \frac{\Theta_x \sigma_{0,x} \Gamma_{E_\gamma,x} \epsilon_{E_\gamma,x}/M_x}{\Theta_c \sigma_{0,c} \Gamma_{E_\gamma,c} \epsilon_{E_\gamma,c}/M_c} \tag{3.8}$$

By the $1/v$ assumption we can also expect, that the ratio σ_x/σ_c stays unaffected by the matrix conditions and geometry of the sample. In such a case, $k_{x,c}$ is simply the experimentally measured ratio of sensitivity S_x for element x to the sensitivity S_c of element c and it is independent of the sample composition as well as of its geometry. In other words, although the sensitivities

$$S_x = A_x/m_x = \frac{N_x/t}{m_x} \tag{3.9}$$

in counts$\cdot$s$^{-1}\cdot$g^{-1} for each particular element differ strongly with the sample matrix (due to different scattering and absorption properties of the sample matrix), the biases disappear when ratios of sensitivities $k_{x,c} = S_x/S_c$ are taken into account (Molnár et al., 1998).

Usually either H (E_γ = 2223 keV) or Cl (E_γ = 1951 keV) are chosen as the inner comparator, because of their frequent occurrence in common chemical compounds and the environment. The results of the PGAA analysis are then usually presented as a ratio with respect to the element with the highest abundance in the particular sample (major elements – e.g. Si, K, Ca, Fe, ...). The complete composition of the sample can also be given when assuming that all the elements appear in the spectrum (Révay, 2004). An illustrative example of particular use of the k_0 approach and determination of the k_0 values for given laboratory with a Cl as an inner comparator was presented by Acharya et al. (2001).

The determined sensitivities from (3.9) S_x are characteristic for each particular PGAA instrument but the values are very stable and independent of the sample matrix and geometry, if taken in ratio $k_{x,c} = S_x/S_c$ (Molnár et al., 1998). Therefore, the $k_{x,c}$ values can be generalized and the k_0 method can become laboratory independent procedure, if the PGAA detector efficiency $\epsilon_{ef}(E_\gamma)$ is eliminated:

$$k_{0,c}(x) = \frac{S_x/\epsilon_{E_\gamma,x}}{S_c/\epsilon_{E_\gamma,c}} = \frac{\Theta_x \sigma_{0,x} \Gamma_{E_\gamma,x}/M_x}{\Theta_c \sigma_{0,c} \Gamma_{E_\gamma,c}/M_c} \tag{3.10}$$

That means, the k_0 values are in this approximation independent even of the energy E_n of the cold neutrons for all elements without resonances in the region close to E_n. This includes the majority of elements, exceptions are the already mentioned Cd, Sm, Eu and Gd, so-called strong non-$1/v$ elements. These elements have their first resonances already in epithermal energy region close to thermal neutron energy of 25 meV. Since the cold neutron spectrum has wavelength distribution close to a Maxwellian shape as shown in Figure 3.19, some part of the spectrum falls into the epithermal energy region, where the neutron resonances can occur and so they can affect the total neutron-capture cross-section σ_c. Recently, a study was published by Sun et al. (2003), which deals with these strong non-$1/v$ elements (Cd, Sm, Eu and Gd) and presents in detail, how to calculate their k_0 values. If we disregard the non-$1/v$ elements, the k_0 values are comparable among all PGAA laboratories and one database can be used for all of them. For relative concentration $\rho(x/y)$ of element x relative to element y in any examined sample the following formula can be therefore used with the help of (3.9) and (3.10):

$$\rho(x/y) = \frac{A_x/\epsilon_{\gamma,x}k_{0,c}(x)}{A_y/\epsilon_{\gamma,y}k_{0,c}(y)} = \frac{m_x}{m_y} \propto \frac{n_x}{n_y} \tag{3.11}$$

This formula (3.11) shows the proportionality of the concentration of particular elements x and y with their relative masses and the relative number of atoms n of both elements x and y in the sample. This explains, why by knowing the absolute concentration of one element, all other can be determined absolutely, too.

3.2.5 Special case: Boron

The detection of boron in samples by the PGAA technique is based on a particular nuclear reaction that differs from the (n,γ) reaction. Boron ^{10}B has very high thermal neutron absorption cross-section σ_a=3837 barn for the (n,α) reaction:

$$^{10}\text{B} + n \overset{93{,}5\%}{\longrightarrow} \alpha + {}^{7}\text{Li}^{\,*} \longrightarrow \alpha + {}^{7}\text{Li} + \gamma\ (477.6keV) \tag{3.12}$$

The thermal/cold neutron capture follows reaction ^{10}B(n,α)^{7}Li*, where ^{7}Li* is initially in an excited state (93.5 %). During its recoil which is comparable with the half-life of the excited state (10.5 ps), ^{7}Li* deexcites into the ground state by emitting a 477.6 keV γ-ray. This gamma peak is therefore Doppler-broadened and it is used for the boron in sample qualification and quantification. ^{10}B abundance in natural boron is 18.4 % of weight units. Limit of detection for boron in liquid samples for thermal neutrons is in order of 1 ppm[1].

Using a cold neutron beam, the analytical sensitivity of boron is increased due to the $1/v$ dependence of neutron capture cross-section, where v is the neutron velocity (see section 3.2.1). In the region of interest, 2 other elements always occur: sodium with the capture reaction of ^{23}Na(n,γ)^{24}Na, with E$_{\gamma}$=472 keV and lithium: ^{6}Li(n,γ)^{7}Li, with E$_{\gamma}$=477.6 keV. Na is contained in the NaI(Tl) scintillator crystal of the Compton suppressed spectrometer and ^{6}Li is present in the shielding material against scattered neutrons – ^{6}LiF polymer – in the measuring chamber. For water samples, neutrons are strongly scattered on H out of the sample, they interact more with the surrounding material and increase considerably the background of the acquired spectra when compared with solid samples, which contain mostly low amount of scattering elements.

---

[1] Parts per million, usually units of μg/g are meant, but also units of μl/l are used by chemists.

composition and fitting of the Doppler-broadened ^{10}B peak region

For the fitting of the Doppler-broadened ^{10}B peak, we use the approach of Magara and Yonezawa (1998). The region with the Doppler-broadened ^{10}B peak fitted this way is very satisfactory for liquid samples, however, for boron in solid samples, we use another function, which better describes the shape of the boron peak in solid samples (Genilloud, 2000).

boron in liquids

For boron in liquids, the region of interest (between 468 keV and 486 keV) is divided according to Magara and Yonezawa (1998) to functions of independent overlapping peaks (usually only Na and Li, but it could be also Co or Br); Together with the Doppler-broadened ^{10}B peak and background contribution in this region of interest we can write:

$$F(E) = \sum F_Z(E) + F_B(E) + F_{Bgr}(E) \tag{3.13}$$

Here we can understand under $F_Z(E)$ e.g. $F_{Na}(E)$ and $F_{Li}(E)$, and they are common Gaussian shape functions for description of the overlapping Na (472keV) and Li (478keV) peaks, $F_B(E)$ describes the Doppler-broadened ^{10}B shape and finally $F_{Bgr}(E)$ approximates the background contribution. The Gaussian shape function for Na, Li or for other elements in the region follows as:

$$F_Z(E) = N_Z \exp\{-\frac{(E-E_Z)^2}{2\sigma^2(E)}\} \tag{3.14}$$

Here E_Z is the position of the E_γ peak centre of the element Z, N_Z and $\sigma(E)$ represent the peak height and width, respectively. After fitting, the net-area of these Gaussian peaks is given by $Area_Z = \sqrt{2\pi} N_Z \sigma(E)$. Its shape is sometimes slightly modified, usually by adding a low energy exponential tail.

The line-shape function for the Doppler-broadened boron peak introduced by Magara and Yonezawa (1998) is obtained as the following integral:

$$F_B(E) = N \int_0^\pi \exp\{-\frac{(E-E_0+k\cos\Theta)^2}{2\sigma^2}\} \sin\Theta \, d\Theta \tag{3.15}$$

where E_0 is the position of the peak centre, N and σ represent the peak height and width, respectively (σ fulfills the well known relation: $FWHM = 2\sqrt{2\ln 2\sigma}$) and the relation $k \cdot \cos\Theta$ gives the Doppler energy shift. The F$_B$(E) integral function has no analytical solution nevertheless after integrating and some adjustments it can be written as following:

$$F_B(E) = \frac{Area}{4k}[erf(\frac{(E-E_0+k)}{\sqrt{2}\sigma}) - erf(\frac{(E-E_0-k)}{\sqrt{2}\sigma})] \tag{3.16}$$

where the new parameter $Area$ gives directly the searched Doppler-broadened boron peak area.

The background contribution in the region of interest can be fitted by a linear function of energy with parameters a, b:

$$F_3(E) = aE + b \tag{3.17}$$

or another possibility is to use more complicated function according to Magara and Yonezawa (1998):

$$F_{3'}(E) = A \arctan\{b\,(E - E_2)\} + C \tag{3.18}$$

where A, b, E_2 and C are free parameters. This latter function is convenient mainly for more intense Doppler-broadened ^{10}B peaks (i.e. for concentration higher than 10 ppm) because it includes a low energy step caused by low angle Compton scattering of the γ-rays from the surrounding material back to the detector. According to the experience with the fitting procedure, the E_2 parameter of the equation (3.18) can be set equal to E_0 of the boron peak from equation (3.15). This makes easier the fitting process and avoids number of divergences during the iteration procedure. The fitting procedure is based on non-linear least square method based on the Levenberg-Marquardt algorithm. The equation (3.17) is adequate and can be accordingly used without significant influence on the fitted boron area only for lower concentrations of the boron in the sample (less than 10 ppm). An example of a fitted Doppler-broadened boron peak (20 ppm water solution of H_3BO_3, which corresponds to 3.5 ppm of ^{nat}B) overlapped with Na and Li peaks is presented in Figure 3.4. The sample was prepared at PSI and measured with the PGAA facility at PSI in 2001.

boron in solid samples

The slowing down of the ^{7}Li* in a solid sample is usually much lower than in liquids and therefore another fitting function for the Doppler-broadened boron peak was used, which better describe the shape of the boron peak in that case. The fitting function is based on the integral of Doppler-broadened Lorentzian function described by Jolie et al. (1988):

$$I(E) = \frac{Area}{2E_0\pi\beta}\left\{\arctan\left[\frac{2}{\Gamma}(E - E_0(1-\beta))\right] - \arctan\left[\frac{2}{\Gamma}(E - E_0(1+\beta))\right]\right\} \tag{3.19}$$

where Γ means the natural width (FWHM) of the unbroadened peak, β is v/c ratio with the velocity v of ^{7}Li* when emitting the γ-ray. E_0 is the centre of the Doppler-broadened peak at 477.6 keV and $Area$ is the total net area of the Doppler-broadened peak.

According to the experience with the fitting function it was found out, that the second power of this (3.19) function – $I^2(E)$ better describes the boron peak than the function $I(E)$ and therefore the $I^2(E)$ was implemented to the automated fitting program PEGASE (Genilloud, 2000) for the analysis of the PGAA data at the PSI. An example of a boron fit by the $I^2(E)$ function is presented in Figure 3.5. The boron concentration in the sample of a homogeneous powder of SRM 1570a Spinach

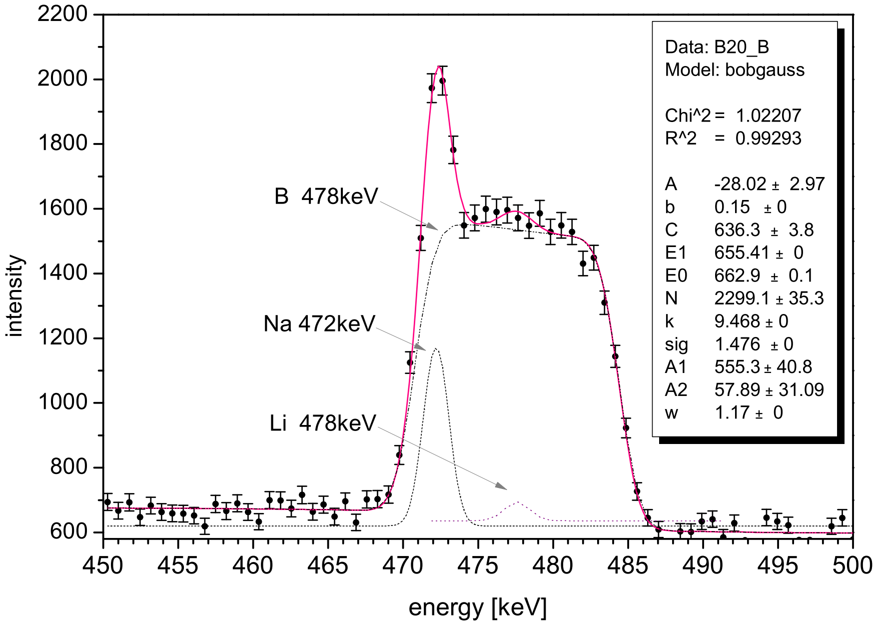

Figure 3.4: A fit of a Doppler-broadened boron peak in liquid performed according to Magara and Yonezawa (1998). The boron concentration in water was 3.5 ppm. The interfering sodium peak at 472 keV originates from the NaI(Tl) scintillator used for the Compton-suppressed spectrometer.

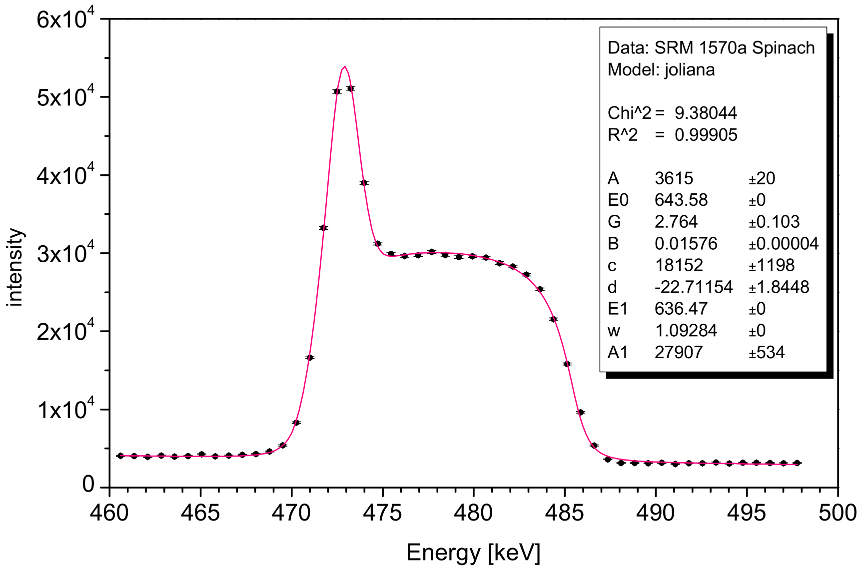

Figure 3.5: A boron peak fit performed with the squared Lorentzian Doppler-broadened function $I^2(E)$, where $I(E)$ is described by the equation (3.19).

Leaves pressed into a pill was 37.6 ppm, the sodium concentration in the sample was 1.81 %, the sample was measured with the PGAA facility at PSI in 2001. To study the applicability of the $I^2(E)$ function described by the squared Lorentz-broadened function (3.19) and the Gauss-broadened function described by the formula (3.15), both functions were implemented into a nonlinear fitting procedure of the Origin© 6.0 and systematically compared. The results achieved by the fitting procedure agree with the expectations: formula (3.19) fits better the Doppler-broadened boron peak in solid samples, formula (3.15) better describes the Doppler-broadened boron peak in liquid samples.

boron in both solid and liquid samples approach

In the year 2000, another very interesting and sophisticated approach for the decomposition and fitting of the Doppler-broadened boron peak was introduced by Kubo and Sakai (2000). Their approach in the mentioned article uses a parameter D which is so-called "degradation constant characterizing the deceleration process of ^{7}Li* in the material" while emitting the 477.6 keV γ-ray within the maximal deceleration time t_E after the neutron capture. With the approach of Kubo and Sakai (2000), not only the Doppler-broadened boron peak can be skilfully fitted but also the averaged stopping power of the environment of sub-micrometer vicinity of the boron atoms represented by the degradation constant D can be determined. This approach is equally convenient for liquid as well as for solid samples. Therefore, we intend to try using this fitting procedure for the future PGAA experiments at FRM-II instead of the two functions used each for boron in liquids and solid samples.

Application: Boron Neutron Capture Therapy in medicine PGAA is a very convenient method for the measurement of boron in solutions – once the sample is prepared it does not need any additional manipulation. That is not a case of e. g. very sensitive chemical technique of Inductively Coupled Plasma (ICP) where the risk of contamination by boron is thus much higher. Measuring of boron in liquids is of interest e.g. for medical applications like Boron Neutron Capture Therapy (BNCT)[2], Boron Neutron Capture Synovectomy (BNCS) (Yanch et al., 1999) or similar treatments by neutron capture on ^{10}B transported to the tumor cells of the organ with carcinomas (for example a new treatment of an organ with a tumor, taken outside of the patient's body, with subsequent irradiation and following auto-transplantation of the organ after the treatment).

In the connection with medical applications, another advantage of PGAA compared to ICP is the promptness of the results and no destruction of the sample, which can be remeasured if needed.

---

[2] introduction to BNCT e.g. by Sauerwein and Garbe (2005) and Harling (2005) or full report about BNCT by IAEA (2001).

3.2.6 PGAA compared with INAA and PIXE

Compared with INAA[3] , PGAA has generally worse limits of detection for many elements but it is a complementary method for important light elements like H, Li, Be, B, C, N, O, F and P[4]. For some elements, PGAA is a competitive technique to INAA (e.g. S, Cd, Gd, Tl, Pb and Bi). One can conclude that it is better to use PGAA instead of INAA depending on the combination of elements of interest and their expected amounts in the particular sample (PGAA is not an eligible method for an ultra-trace analysis, in contrast to INAA). Another criterion for choosing PGAA can sometimes be long-term activation of the sample by INAA, which does not allow direct manipulation of the sample after irradiation. With PGAA, the cold neutron flux is orders of magnitude lower than with INAA[5] and even for longer times of sample irradiation/measurement usually only short-time activation of the sample is caused or the activity is much faster below the allowed limit. Although the INAA can reach much lower limits of detection for lots of the detectable elements (well summarized and compared among three laboratories by Alfassi (2001) in Chapter 1), the irradiation of the sample at the reactor core can take days or weeks for elements with long half-life products. Also subsequent measurement and counting of the decay γ-rays of the irradiated sample can take weeks (the general procedure is well described by Alfassi (2001), page 39-42). In case of PGAA, the maximal irradiation time takes maximally 24 hours and is usually dedicated to these elements: O, C, Pb and Bi. And the irradiation time is at the same time the PGAA acquisition time. Therefore, the great advantage of PGAA in comparison to INAA is the promptness of the results. One study comparing PGAA and NAA have appeared few years ago by Yonezawa and Matsue (2000).

As for INAA, PGAA is for low Z elements (like H, B, C, N and similar) a complementary method to PIXE, although the PGAA limits of detection for C, N and O are generally only in units of percents. A motivation to choose PGAA instead of PIXE can arise for samples with high content of e.g. Ca or Fe, which in PIXE easily overlap with some important trace elements (e.g. Cd, In, Co, Gd ...). Another good reason for using PGAA together with PIXE is to find out, if the matrix of the sample

---

[3] Instrumental Neutron Activation Analysis is like PGAA a non-destructive method for element determination in the sample bulk. The Radiochemical Neutron Activation Analysis (RNAA) uses chemical separation of elements of interest after the irradiation and thereby it is a destructive method. For its destructivity, we do not use the RNAA method for comparison with PGAA.

[4] Isotope ^{32}P from the ^{31}P(n,γ)^{32}P capture reaction is a pure β^- emitter and therefore INAA can not be used for its determination. For its detection, the ^{32}P must be chemically separated from the sample and its concentration is determined by the detection of β^- (Lin, 2005)

[5] e.g. PGAA at PSI had used cold neutron flux of units of 10^8 n/cm^{2}s instead of units of 10^{14} n/cm^{2}s of reactor neutrons – mostly thermal and epithermal neutrons are utilized by INAA.

bulk is consistent with the matrix of the sample surface. Such a complementary bulk and surface analysis can contribute to the research by very important information: e.g. for the archaeological samples with an enamel or a patina on the surface or, in geology, for samples with the surface altered by erosion and weathering.

3.3 PGAA at PSI – short history

The PGAA facility at the Swiss Spallation Source at Paul Scherrer Institute (PSI), Switzerland, was successfully operated by the University of Fribourg during the years 1997 – 2002. The measuring place at the end of the curved cold neutron beam guide 1RNR12 was shared with a cold-neutron tomography set-up for small samples (Crittin et al., 2000b; Baechler et al., 2002b). The cold neutron beam had dimensions $2 \times 5\,\mathrm{cm}^2$ and a focusing Khumakov lens with the same entrance dimensions was occasionally utilized to focus the neutrons to a spot smaller than $1\,\mathrm{mm}^2$. After the move of Prof. J. Jolie to the University of Cologne (October 2000), the installation was operated by the University of Cologne. At that time, I have performed with S. Baechler several PGAA measurements, see below in part 3.3.1.

At the beginning of the year 2002, the PGAA instrument as well as the tomography set-up were dismounted and moved all-inclusive to be installed at the new reactor FRM-II at Garching by Munich, Germany. Several delays to get permission to operate the FRM-II have considerably delayed the PGAA installation there. Therefore, we will report also on PGAA experiments performed at BNC, Budapest.

During the last experiments at PSI, the neutron flux was about $1.4 \cdot 10^8\,\mathrm{n/cm^2s}$. The limits of detection (LOD) reached with this PGAA instrument were very convincing. Some of the limits of detection are inserted into the Table 3.2. The Table 3.2 will be published soon in (Kudějová et al., 2005b).

Very sensitive measurements of boron concentration in samples were envisaged from the very beginning with the PGAA installation at PSI and the complete PGAA instrument – including also the neutron guide – was adapted to it and specially designed with a great effort to minimize the presence of boron in the surrounding material. The limits of detection that we have achieved for boron in water solution in 2001 were $0.08\,\mu\mathrm{g/g}$ (Baechler, Kudejova et al. (2002)) and $0.0038\,\mu\mathrm{g/g}$ for boron in solid geological samples (Crittin et al., 2000a). The limit of detection for hydrogen that was obtained with the same PGAA facility was $0.69\,\mu\mathrm{g/g}$. Since the neutron flux at FRM-II will be at least of order of magnitude higher, our expectations are to get more than 3 – 5 times better limits of detection at FRM-II than at PSI. However, the success of this plan will depend not only on the much higher neutron flux, but also on the feasibility to keep the γ-background at the target position as low as at PSI. A detailed description of the PGAA facility at PSI was presented by Crittin et al. (2000b), the experiments are by now mostly published by Baechler, Kudejova et al. (2002) and Baechler, Kudejova et al. (2003) and therefore we give here just an overview.

Element	E_γ [keV]	Sensitivity[1] [cps/mg]	LOD [$\mu g/g$]
H	2223	4.22 ± 0.14	0.69
B	478	2237 ± 53	0.00387
C	4945	0.00138 ± 0.00008	1070
N	1885	0.0148 ± 0.0007	235
Na	472	0.704 ± 0.017	8.07
Al	1779	0.130 ± 0.004	26.8
Si	3539	0.0320 ± 0.0011	63
P	637	0.0283 ± 0.0007	189
S	841	0.250 ± 0.006	23.8
Cl	1165	5.0 ± 0.1	1.02
K	770	0.604 ± 0.016	7.8
Ca	1942	0.123 ± 0.004	26.7
Ti	1381	1.820 ± 0.054	2.05
Cr	834	0.625 ± 0.018	11.0
Mn	314	1.18 ± 0.03	6.04
Fe	7631	0.033 ± 0.002	27.9
Co	230	5.94 ± 0.15	1.29
Ni	465	0.474 ± 0.012	12.1
Cu	278	0.629 ± 0.016	16.1
Zn	1077	0.1100 ± 0.0039	37.2
Cd	558	395.3 ± 9.8	0.0142
Sn	1293	0.0177 ± 0.0006	214
Sm	334	1159 ± 28	0.00604
Gd	182	2288 ± 56	0.00346
Hg	368	48.1 ± 1.2	0.143
Pb	7368	0.0021 ± 0.0001	331

Table 3.2: The limits of detection LOD and corresponding sensitivities for selected elements and some of their characteristics energy peaks E_γ obtained with the PGAA installation at PSI with the cold neutron flux of $1.4 \cdot 10^8\,n/cm^2s$ at the end of the year 2001.

[1] Sensitivity is given for $1.4 \cdot 10^8\,n/cm^2s$ of a cold neutron flux

3.3.1 Examples of experiments at PSI

The variety of applications and samples measured at PSI was very large. We would like to continue this way also at FRM-II and introduce the capabilities of the PGAA technique also to other applied research groups and centres, because the PGAA method is still not very well known. For the analysis, we were using the comparative k_0 method. Therefore, our own interest was to measure 38 k_0 values of the most important elements and to compare the results to the well established k_0 values database measured by the Budapest PGAA group (Révay et al., 2000).

k_0 values at PSI, 2001 During the year 2001, we have performed measurement of 38 k_0 values of 26 most important elements for PGAA[6]. Since chlorine forms compounds with nearly all elements, it was chosen as the inner comparator. Samples with known and well defined stoichiometric ratio to chlorine were chosen and a set of 4 – 5 samples for each element of interest was analysed. Elements like Pb, which do not build compounds with Cl, were weighted and mixed carefully with chlorine containing compound (urea) to keep the samples in form of homogeneous mixtures. The obtained k_0 values were compared with the database of k_0 values of the Budapest PGAA group measured with thermal neutrons and with k_0 values of the PGAA group at JAERI in Japan, measured with a cold neutron beam (Matsue and Yonezawa, 2000, 2001). The comparison together with first applications of our k_0 values for the measurement of standard reference material (SRM) of NIST and for real geological samples was published in JRNC by Baechler, Kudejova et al. (2003). The determined k_0 values were then used for the analysis of the performed experiments and applications at PSI. A digest of them is briefly described here.

Applications For archaeometry, fifty-four selected pieces of brooches from Western Switzerland, representative with respect to chronology and typology, were analyzed by the PGAA method for the major components Cu, Zn, Sn and Pb. A composition of 18 brooches is displayed in Figure 3.6. Conclusions could be then made by the archaeologists about the preparation of the brass and the bronze alloys in relation to the place and time of origin of the brooches, as referred by Baechler, Kudejova et al. (2003). INAA cannot be used in this case because of the difficulties to detect Pb. PGAA is also less sensitive to detection of Pb, however, the amount of Pb in the brooches was much higher (units of percent) than the limit of detection for Pb of the PGAA instrument at PSI ($331\,\mu$g/g). As an example of a multi-elemental analysis, many different homogenized powder samples were measured, e.g. NIST Standard Reference Materials (SRM) to compare the composition of the samples measured by the PGAA method with the reference values given by NIST, see e.g. Table 4.1.

Hydrogen is also of great interest for the PGAA measurement because there are only few reliable techniques for its sensitive non-destructive measurement in a sample

---

[6] for some elements like, Fe, Co, Ni, Cu, Zn or Sm, k_0 values for more than one γ-ray were determined.

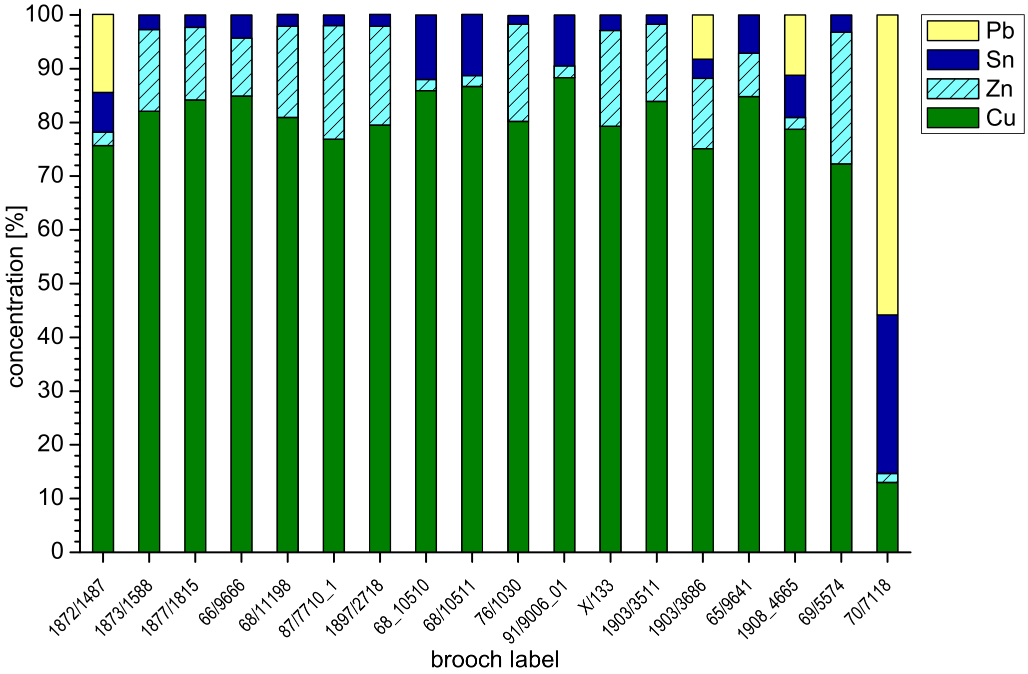

Figure 3.6: Matrix composition of 18 selected brooches, which were analysed at PSI in 2001.

bulk. Thus, the hydrogen content of Zr-alloys was determined as it was for YBCO superconducting crystal. Another useful application of the PGAA technique was found with respect to the storage of radioactive waste. A multi-elemental analysis of ashes, originating from burnable waste from Swiss nuclear power plants, medicine, industry and research, was performed (Baechler et al., 2001). Here, PGAA takes advantage of being a non-destructive method as well as of already mentioned no need of any special preparation of the sample in comparison to chemical methods (e.g. ICP-OES or ICP-MS). These methods usually require a total dissolution of the investigated material, which is in case of radioactive material always connected with the task of avoiding any contamination. Therefore, when possible, non-destructive methods with satisfactory sensitivity should be preferred.

Boron in samples Boron is an element which is difficult to determine by another non-destructive method. That is why many of experiments at PSI were connected with an analysis of a trace amount of boron in samples. For geological research, boron in mineral water was determined (Grimm, 2000). Amounts of boron in moderator rods of a graphite reactor as well as in Ni_3Al alloys was measured and determined. For medicine, the amount of boron taken up by cells in research of new treatment of rheumatoid arthritis was determined (Stritt, 2001).

For the proper analysis of the Doppler-broadened boron peak in solid samples

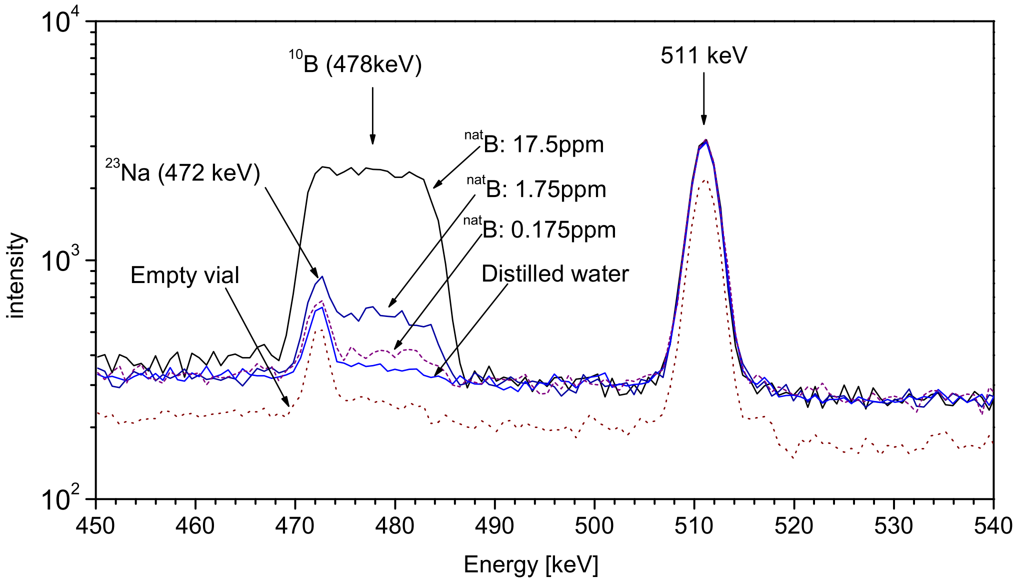

Figure 3.7: Doppler-broadened boron peaks of several concentrations of H_3BO_3 diluted in water, prepared and measured with the PGAA facility at PSI in 2001.

resp. in liquids, we have used the approach of Jolie et al. (1988) resp. of Magara and Yonezawa (1998) and formulas listed and explained in section 3.2.5.

In the particular case of boron in liquids, we have used the Origin© 6.0 for the Doppler-broadened boron peak analysis and we have implemented the fitting function F(E) described by the relation (3.13) into a nonlinear fitting procedure there. For the boron concentrations higher than ca. 5 ppm, the Doppler-broadened boron peak is large enough to allow one to neglect the F_{Li} part of the fitting function (3.15) since its influence starts to be insignificant in comparison to the boron peak. Indeed, then the contribution of the E_γ=477.6 keV from the ^{6}Li(n,γ)^{7}Li reaction, which has very low neutron capture cross-section of 0.038 barn, is comparable with the statistical fluctuation of the ^{10}B peak height. So, the ^{7}Li peak can be accordingly omitted from the fitting procedure of the F(E) evaluation.

To sketch the obtained accuracy of the boron concentration in water samples, the results published by Baechler, Kudejova et al. (2002) are drawn out here:

> *"The measured value for 17.5 ppm natural boron solution is determined with a statistical error of 1 % and for comparison: 0.175 ppm . . . 10 %; 1.75 ppm . . . 2.5 %; 175 ppm . . . 0.7 %."*

The surface of such Doppler-broadened boron peaks normalized to the same time unit is displayed in Figure 3.7.

3.4 Experiments with PGAA instrument at BNC

A long term project of a systematic elemental analysis of meteorites in cooperation with Prof. H. Palme from the Institute of Geochemistry and Mineralogy of the University of Cologne is planned for the PGAA facility at FRM-II (the PGAA at FRM-II will be discussed in section 3.5). Although the majority of the meteorites were already submitted to an accurate chemical analysis or INAA, precise analysis of some elements was difficult this way (e.g. already mentioned H, B, C, N, P, S). PGAA is able to determine amounts of these elements in the meteorite samples as well as concentrations of many other important elements for comparison and for a reliability check.

To demonstrate that the PGAA method is competent for such a meteorite analysis, first test measurements of small amounts (hundreds of mg) of meteorites and geological standards were performed at the well-established PGAA facility, operated at the Budapest Neutron Center (BNC), Hungary. The experiments in 2003 and 2004 in Budapest as well as the precise data analysis by the Hypermet-PC program, were accomplished in tight and fruitful cooperation with the local PGAA group, mainly Zsolt Kasztovszky, Zsolt Révay, Laszlo Szentmiklosi and Tamas Belgya.

First promising PGAA experiments and analysis of meteorites have already appeared in Japan by Latif et al. (1999) and Oura et al. (2002).

Selection of the samples

To show the reliability of the PGAA analysis, composition of international geological standards GSP-1 (Granodiorite) and G-2 (Granite) as well as a meteorite called Orgueil with known composition were determined. The results were compared with nominal values given by Gladney et al. (1992) for the geological standards and with values compiled by Palme and Jones (2003) for the meteoritic standard.

Then, three pieces of Allende meteorite were measured and compared to literature values included in a large compilation of meteorite compositions by Jarosewich (1990) and in an older work of Kallemeyn and Wasson (1981). An interesting point for the comparison of the PGAA analysis was, that the first two samples of the Allende meteorite (one of them was also studied by the PIXE analysis, see section 2.4.4) had very similar composition, but it was not in a good agreement with the literature values for all the elements (e.g the measured amount of sodium was 3 times lower, of sulphur 1.6 times lower, see Table 3.6). The result was surprising for us and at it lead us first to compare the analysing program Hypermet-PC developed and used in Budapest with PEGASE, which was developed and used by the Fribourg group for the PGAA installation at PSI. The difference between the results was maximally 27 % (for sodium it was 15 % and for sulphur only 1 %, see Table 3.13), which has verified the Hypermet-PC results in comparison to the very different literature values. Then, we have obtained another piece of Allende for the PGAA analysis to see, if the difference between the reference values and the PGAA results appears again.

A difference between the PGAA analysis of a homogeneous powder and a heterogeneous stony sample could be studied on the Dhurmsala meteorite. In case of the next sample – Morávka meteorite, the available amount was only 125 mg of homogeneous powder, though we were able to detect and quantify many elements in the sample. Recently, a detailed composition of Morávka was published by Borovička et al. (2003) so we could compare the PGAA results with results of their methods. Here, the competitive analytical methods used by the group of authors in the publication are presented for information.

Since the amount of boron in the examined samples of meteorites and geological standards is very low ($\leq 1\ \mu$g/g) and since the mass of the samples was also very small, we were not able to quantify the amount of boron in many cases. The limit of detection for boron with the PGAA facility at BNC is around 1 μg/g. Therefore, volcanic stones with sufficient mass were measured and the boron amount could be compared. The comparison was performed not only among different volcanic stones of the same origin but also with a volcanic stone from a neighbour place. Additionally, two common stones from Himalaya mountain region were analysed for boron concentration and compared with the volcanic samples.

The spectra were evaluated by the Hypermet-PC program (Révay et al., 2001), using the wide database of k_0 values measured and compiled by the same PGAA group, too (Révay et al., 2000). Thanks to the significantly higher neutron flux at the FRM-II in Garching, the time of measurement should be reasonably reduced even in case of smaller samples ($\leq$ 100 mg) and the expected limits of detection should be much better.

3.4.1 Experimental set-up at BNC

The detailed description of the PGAA instrument at the end of the 35 m long and curved cold neutron beam guide at the 10 MW research reactor of the Budapest Neutron Centre (BNC) can be found in publications dedicated to the PGAA instrument and the new cold neutron beam guide; e.g. (Révay et al., 2004; Belgya et al., 2003, 1997; Rosta, 2002). The prompt γ-rays are detected by a Compton-suppressed spectrometer, which consist of a central HPGe detector shielded by a BGO scintillator and connected in anticoincidence with it. The HPGe crystal is situated at the distance of 23.5 cm from the target position. Around the whole spectrometer, lead, ^{6}LiF and B_4C shielding is employed. The cold neutron flux at the target position was of $5 \cdot 10^7$ n/cm^{2}s thermal beam equivalent and the background count rate was as low as 4 cps in the full spectra. The neutron beam was collimated to 2×2 cm^2 and a set of exchangeable collimators could be used to reduce further its surface to avoid saturation of the detector and large dead time of the analogue acquisition system. Concerning boron, an interesting feature of the PGAA at BNC is, that although borofloat glass is used even for the last part of the beam guide and shielding containing B_4C is utilized around the Compton-suppressed spectrometer and around the beam guide from outside, the boron peak is not significant in the PGAA background spectrum.

Our intention was to measure very small amounts of samples and we wanted to quantify as many elements as possible. In order to improve the limits of detection and quantification, the measurements were carried out for longer time (10000 s – 52400 s), depending on the sample size and the input count rate.

3.4.2 Samples, Results and Discussion

Geological Standards

Homogeneous powders of GSP-1 (335 mg), G-2 (192 mg) and of Orgueil (232 mg) were measured for 12500 s, 27700 s and 16500 s, respectively. These measurements were performed with the aim to compare the results of the PGAA analysis with standard reference values and to show the reliability of the PGAA method. The comparison of GSP-1 Granodiorite to nominal values compiled by Gladney et al. (1992)[7] is presented in Table 3.3 and an overview is shown in Figure 3.8. The concentrations of some elements were recalculated to oxygen compounds for comparison. Elements like B, K, Mn, Sm and Eu do not agree within one combined standard deviation with the literature values. Elements H, B or Cl are determined with much better precision than the literature values, while V and Mg have much worse precision, the rest of the elements and compounds are determined with comparable accuracy.

The same procedure as for GPS-1 was applied also to G-2 Granite and the comparison with literature values of the same author Gladney et al. (1992) is listed in Table 3.4 and in Figure 3.9. The concentration of B, K and Sm determined by PGAA differs from the literature values, Mn and Fe are determined with better precision and Si with worse precision, the accuracy of the result of all the other elements is comparable with the literature values or, the literature values are given without any error. For some of the elements, the limit of quantification of the PGAA analysis was higher than the amount of the elements in the sample (B, Mg, V, Eu) and only maximal amount of those elements could be assessed. In case of boron the PGAA analysis shows discrepancy with the literature values, but, if the amount of boron in sample was indeed 2.4 ppm, we would definitely see and evaluate the boron amount. Therefore, we can make a statement, that there was much lower amount of boron in the G-2 sample than expected.

In case of Orgueil, the elemental composition is directly compared to the literature values presented by Palme and Jones (2003)[8]. Orgueil meteorite belongs to the rare CI group of carbonaceous chondrites, whose elemental composition is for many elements in very good agreement with the elemental abundances in the Sun, which were determined from the absorption lines by absorption spectroscopy. A part of the

---

[7] Gladney et al. (1992) use mostly ICP-MS (Inductively Coupled Plasma - Mass Spectrometry) combined with XRF (X-ray Fluorescence), INAA, OES (Optical Emission Spectroscopy) and variety of other analytical methods for a reliable and accurate determination of the composition of geological standard reference materials.

[8] Palme and Jones (2003) use INAA and RNAA for the determination of the elemental concentrations in Orgueil.

GSP-1 Compound	PGAA, Budapest [%]			US Geological Survey [%]		
H_2O	0.70	±	0.02	0.61	±	0.11
B	6.54E-05	±	0.13E-05	13.0E-05	±	5.0E-05
Na_2O	3.07	±	0.04	2.8	±	0.09
MgO	1.00	±	0.24	0.96	±	0.07
Al_2O_3	15.09	±	0.31	15.1	±	0.26
SiO_2	66.67	±	1.59	67.22	±	0.24
Cl	0.0349	±	0.0014	0.033	±	0.024
K_2O	6.08	±	0.11	5.51	±	0.08
CaO	2.03	±	0.07	2.07	±	0.04
TiO_2	0.69	±	0.07	0.65	±	0.03
V	7.72E-03	±	2.51E-03	5.30E-03	±	0.70E-03
MnO	0.0497	±	0.0023	0.040	±	0.0036
Fe_2O_3	4.528	±	0.089	4.29	±	0.14
Nd	0.0235	±	0.0024	0.0196	±	0.0017
Sm	18.63E-04	±	0.33E-04	26.3E-04	±	2.4E-04
Eu	3.25E-04	±	0.59E-04	2.33E-04	±	0.21E-04
Gd	12.12E-04	±	0.44E-04	12.10E-04	±	0.20E-04
Dy	5.41E-04	±	0.93E-04	5.50E-04	±	0.70E-04

Table 3.3: Homogeneous powder of GSP-1 Granodiorite (335 mg) was measured for 12500 s and then compared to the nominal values listed in US Geological Survey given by Gladney et al. (1992).

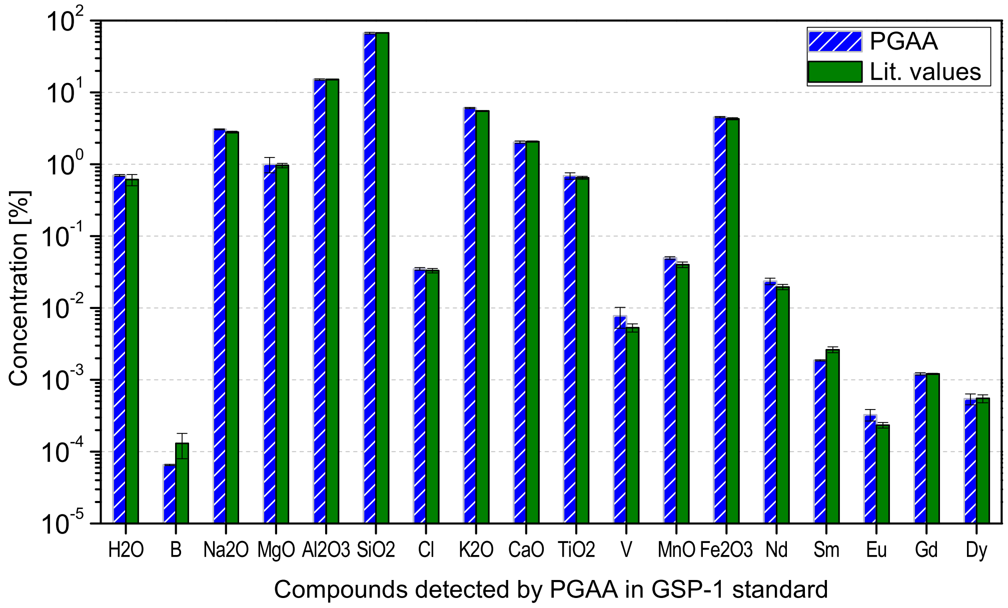

Figure 3.8: PGAA results of homogeneous powder of geological standard GSP-1 Granodiorite (335 mg), which was measured for 12500 s at the PGAA facility in Budapest in 2003.

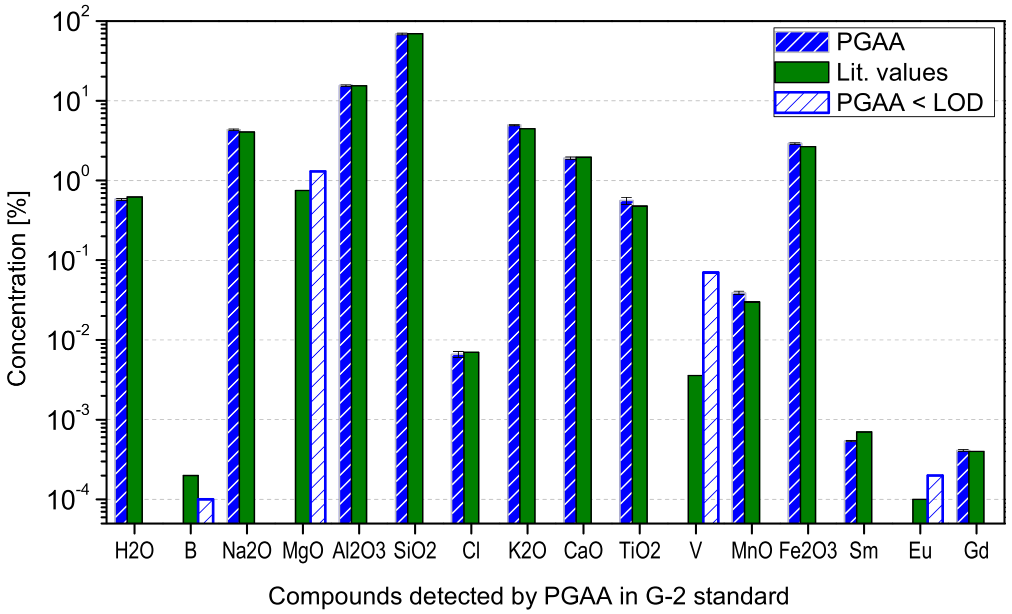

Figure 3.9: PGAA results of homogeneous powder of geological standard G-2 Granite measured at the PGAA facility in Budapest in 2003.

G-2 Compound	PGAA, Budapest[1] [%]			US Geological Survey[2] [%]		
H_2O	0.58	±	0.02	0.623		
B	$<$ 0.0001			0.00024		
Na_2O	4.34	±	0.10	4.08	±	0.13
MgO	$<$ 1.3			0.75	±	0.03
Al_2O_3	15.56	±	0.33	15.39	±	0.30
SiO_2	69.03	±	1.66	69.14	±	0.30
Cl	0.0066	±	0.0006	0.0070		
K_2O	4.94	±	0.09	4.48	±	0.13
CaO	1.91	±	0.07	1.96	±	0.08
TiO_2	0.56	±	0.06	0.48	±	0.03
V	$<$ 0.07			0.0036	±	0.0004
MnO	0.039	±	0.002	0.030	±	0.010
Fe_2O_3	2.91	±	0.05	2.66	±	0.17
Sm	0.00054	±	0.00001	0.00072	±	0.00007
Eu	$<$ 0.0002			0.00014	±	0.12
Gd	0.00041	±	0.00001	0.00043		

Table 3.4: G-2 Granite compared to nominal values given by US Geological Survey (Gladney et al., 1992).

[1] The values with “ $<$ ” sign present maximal possible amount of given compound in the sample, that can not be yet detected or quantified; it is below the limit of detection (LOD) or quantification (LOQ).

[2] The values without given error are non-certified values.

Orgueil Element	PGAA, Budapest [%]			Palme, Jones [%]		
H	1.845	±	0.021	2.02	±	0.20
B	10.83E-05	±	0.38E-05	8.70E-05	±	0.87E-05
C	3.10	±	1.30	3.22	±	0.32
O	47.90	±	5.50	46.50	±	4.65
Na	0.353	±	0.012	0.50	±	0.025
Mg	9.53	±	0.51	9.61	±	0.29
Al	0.863	±	0.037	0.849	±	0.026
Si	10.40	±	0.27	10.68	±	0.32
S	4.35	±	0.10	5.41	±	0.27
Cl	0.0386	±	0.0018	0.0698	±	0.0105
K	0.0475	±	0.0047	0.0544	±	0.0027
Ca	0.674	±	0.041	0.932	±	0.028
Ti	0.0440	±	0.0044	0.0458	±	0.0018
Cr	0.285	±	0.011	0.2646	±	0.0079
Mn	0.1979	±	0.0040	0.1933	±	0.0058
Fe	19.14	±	0.39	18.43	±	0.55
Co	0.0490	±	0.0012	0.0506	±	0.0015
Ni	1.135	±	0.023	1.077	±	0.032
Sm	42.8E-06	±	2.2E-06	15.40E-06	±	0.77E-06
Gd	20.9E-06	±	1.7E-06	20.4E-06	±	1.0E-06

Table 3.5: Homogeneous powder of Orgueil meteorite (232 mg) measured for 16500 s at the PGAA facility in Budapest in 2003 compared to nominal values given by Palme and Jones (2003). Orgueil belongs to the CI group of the carbonaceous chondrites and only this rare group of meteorites match by their composition and concentration very well the elemental abundances in the Sun, which were determined from the absorption lines by absorption spectroscopy of the Sun.

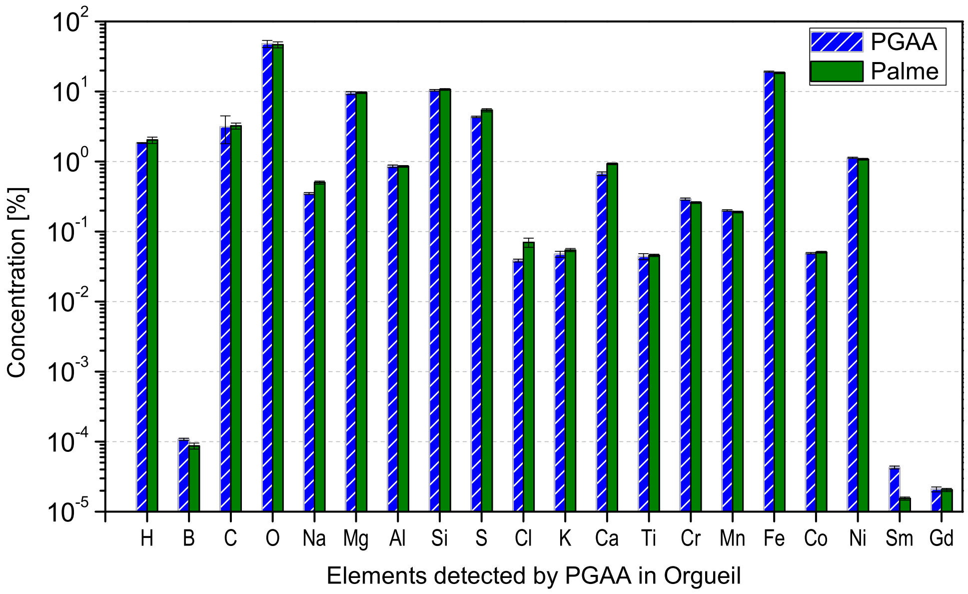

Figure 3.10: PGAA results of the Orgueil meteorite (232 mg) measured for 16500 s at the PGAA facility in Budapest in 2003 correspond very well to the literature values presented by Palme and Jones (2003).

Orgueil spectrum with the energy range between 300 keV and 3000 keV is presented in Figure 3.3. The PGAA results of the Orgueil meteorite match very well the expected literature values and the comparison is presented in Table 3.5 and in Figure 3.10. In case of the PGAA analysis of Orgueil, we can see discrepancy in concentration of these elements: Na, S, Cl, Ca and Sm. Elements Na, S and Cl show by the PGAA analysis lower concentration than expected. This might be caused by some evaporation of these elements, the amount of hydrogen was also found lower than expected. The precision of the PGAA analysis of the hydrogen amount in the sample is usually very good, because no other elements contribute strongly to the spectrum region of hydrogen peak (2223 keV) and also the continuous background is already at very low level. The discrepancy of the boron concentration could be caused by not sufficiently good fitting of the peak. The amount of 1 ppm of boron is close to the limit of quantification, what could explain the worse Doppler-broadened peak fit.

Systematic error in Sm analysis The amount of Sm differs from the literature values in all three cases. This would indicate, that the used k_0 value is very probably not reflecting properly the sensitivity and neutron capture cross-section of the PGAA facility in Budapest. When we check up all tables in this section 3.4, we will find out (with one exception) a systematic underestimation of the Sm amount in the samples by 25 – 40 %. The reason could be explained by the present use of a cold neutron beam

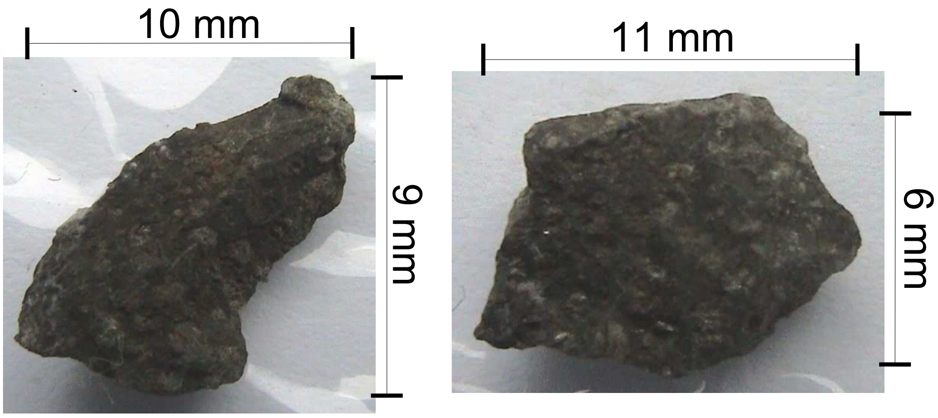

Figure 3.11: Allende 1 (left, 220 mg) and Allende 2 (252 mg) meteorites.

at the PGAA facility at BNC, however with k_0 values determined with a thermal neutron beam, which was used before at the same place. As discussed in sections 3.2.1 and 3.2.4, Sm is a strong non-$1/v$ element and therefore the k_0 value of Sm is dependent on the neutron energy distribution (particularly on the epithermal part of the nearly Maxwellian neutron distribution). When changing from the thermal beam to the cold neutron beam, the average neutron energy will shift to lower energies and the epithermal contribution in the neutron spectrum will decrease too. So, the neutron capture cross-section σ_c will on one side increase by the $1/v$ law, on the other side, it will decrease because of a weaker effect of the Sm resonances in the epithermal neutron energy region. This effect should be studied in greater detail for each PGAA facility as it was done in the work of Sun et al. (2003).

The Sm concentration in Allende 1 analysed with the help of the k_0 values of Budapest PGAA group with Hypermet-PC was later reanalysed by PEGASE with the k_0 values for cold neutrons of the PSI PGAA group. The difference of the Sm amount can be seen in Figure 3.13. The analysis of PEGASE gives of about 1.27 times higher concentration of Sm compared to the Hypermet-PC, which agrees very well with the literature value of Jarosewich (1990), see Table 3.6. This agreement let us assume, that the k_0 value for Sm determined at PSI is more accurate than the one determined at BNC.

There are two more elements, with more often shifted concentration analysed by the Hypermet-PC when compared to the literature values: Mn, with overestimated results by about 10 – 30 % and Ca, with underestimated results by about 25 – 40 %. However, we would need to have more data for comparison to make some conclusions about the correctness of the k_0 values for these elements.

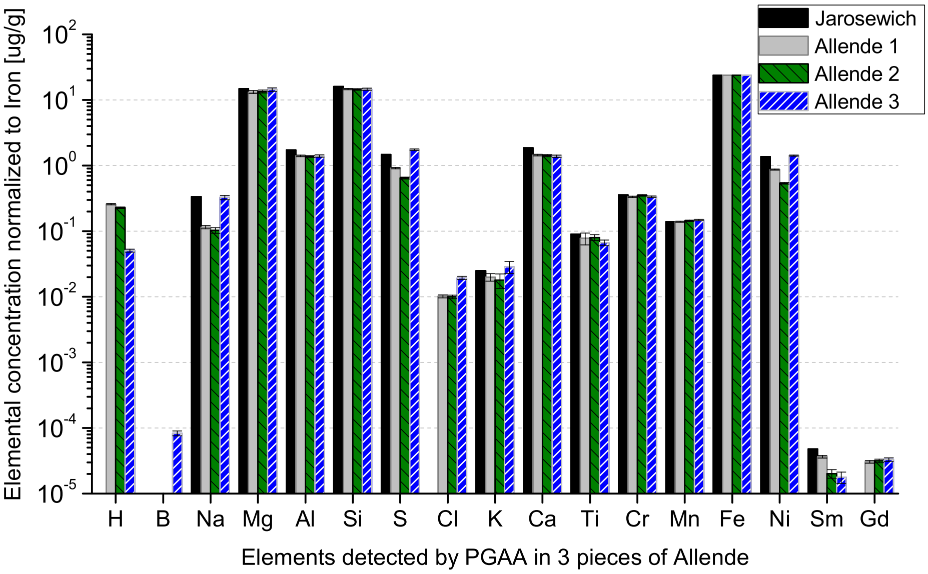

Figure 3.12: PGAA results of Allende 1 (220 mg; 51137 s), Allende 2 (252 mg; 10323 s) and Allende 3 (186 mg; 54571 s) measured at the PGAA facility in Budapest in 2003. The results of the analysis are compared to literature values presented by Jarosewich (1990).

Allende meteorite

The Allende meteorite belongs to a group of stony carbonaceous chondrites CV3. The meteorite is very inhomogeneous, the grains can be seen by naked eye, see picture in Figure 3.11.

In total three pieces of Allende meteorite were measured in Budapest in 2003. They are called Allende 1, Allende 2 and Allende 3. Allende 1 and Allende 2 originate from another part of the inhomogeneous meteorite than Allende 3 and that explains why the concentrations can differ substantially for elements like Na, S, Cl and K. The determined concentrations of the elements by the Hypermet-PC are presented in Table 3.6 and in Figure 3.12. They are compared to the literature values compiled by Jarosewich (1990)[9] and Kallemeyn and Wasson (1981)[10], which are listed in the last two columns of the table. All values are normalized to iron concentration given by Jarosewich. Iron was preferred before silicon, because it has the highest concentration and because we intended to compare the PGAA values also with a PIXE analysis of the Allende surface. Those PIXE results are listed in section 2.4.4 in Table 2.14.

We can see in Table 3.6, that the first two of the meteorite samples – Allende 1

---

[9] Jarosewich (1990) uses mostly chemical methods – including grinding, sieving, separating and dissolution as a part of the sample analysis.

[10] Kallemeyn and Wasson (1981) use INAA and RNAA for the determination of the elemental concentration in meteorites.

Z	Allende 1 [%]	Allende 2 [%]	Allende 3 [%]	Jaros. [%]	Kall. [%]
H	0.2572 ± 0.0060	0.2267 ± 0.0064	0.0505 ± 0.0028	-	-
B			8.3E-5 ± 0.7E-5	-	-
Na	0.1155 ± 0.0067	0.103 ± 0.010	0.327 ± 0.024	0.334	0.329
Mg	13.20 ± 0.69	13.45 ± 0.71	14.39 ± 0.84	14.85	14.80
Al	1.406 ± 0.036	1.377 ± 0.047	1.396 ± 0.056	1.731	1.760
Si	14.68 ± 0.34	14.43 ± 0.39	14.60 ± 0.51	16.00	-
S	0.913 ± 0.021	0.645 ± 0.020	1.748 ± 0.044	1.470	-
Cl	0.01016 ± 0.00057	0.01000 ± 0.00062	0.0194 ± 0.0011	-	-
K	0.0199 ± 0.0026	0.0179 ± 0.0045	0.0285 ± 0.0058	0.0249	0.0294
Ca	1.444 ± 0.045	1.415 ± 0.054	1.385 ± 0.059	1.865	1.880
Ti	0.078 ± 0.016	0.0801 ± 0.0080	0.0668 ± 0.0067	0.0899	-
Cr	0.3339 ± 0.0079	0.352 ± 0.010	0.334 ± 0.010	0.356	0.363
Mn	0.1396 ± 0.0026	0.1438 ± 0.0030	0.1483 ± 0.0038	0.1394	0.1450
Fe	23.85	23.85	23.85	23.85	23.70
Co	0.03908 ± 0.00076	0.0319 ± 0.0010	0.0621 ± 0.0014	0.01-0.02	0.0662
Ni	0.868 ± 0.015	0.535 ± 0.015	1.421 ± 0.030	0.36-0.85	1.33
Sm	36.5E-6 ± 1.74E-6	20.1E-6 ± 3.04E-6	17.8E-6 ± 3.54E-6	47.8E-6	29.8E-6
Gd	30.5E-6 ± 1.37E-6	31.6E-6 ± 2.01E-6	33.1E-6 ± 2.06E-6	-	-

Table 3.6: Allende 1 (220 mg; 51137 s), Allende 2 (252 mg; 10323 s) and Allende 3 (186 mg; 54571 s) were measured at the PGAA facility in Budapest in 2003. The determined concentrations of the elements are compared to the literature values, compiled by Jarosewich (1990) and Kallemeyn and Wasson (1981), which are listed in the last two columns.
[1] All values are normalized to the iron concentration given by Jarosewich.

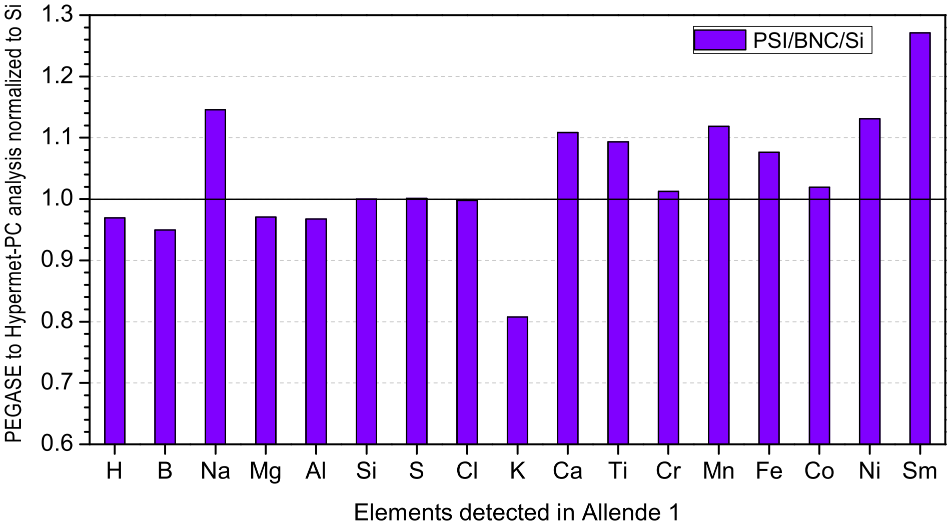

Figure 3.13: Results of the comparison between Hypermet-PC analysis (standard program for PGAA analysis in Budapest) and PEGASE analysis (program used for the PGAA data analysis at PSI) of the PGAA data of Allende 1 sample measured at the PGAA facility in Budapest, 2003. The parameters characterizing the Budapest PGAA facility were used for both programs and the results of the sample concentration were normalized to silicon concentration first. Then, ratio between such normalized results for each element is presented in the figure and it is expected to be close to one for each element.

and Allende 2 – have very similar composition, but the composition is not in good agreement with the literature values for all elements, namely for Na, Al, S, Si, Cl, K, Ca, Co and Sm. Since we were convinced about the correctness of the PGAA results, we wanted to validate them by the mean of another analysing program, which uses another calibration curve and other k_0 values. The results of such a comparison are listed in the following paragraph. Allende 3 better agrees with the literature values for Na, Mg, S, K, Co and Ni and gives worse result for Sm. The results were discussed with Prof. Palme (2005). The differences in H, Na, Al, S, Si, Cl, K and Ca between the 3 pieces of Allende are possible because of the strong inhomogeneity. For comparison of Co and Ni, the reference values of Kallemeyn and Wasson (1981) should be taken (Palme, 2005). It was never measured such difference between Co and Ni in Allende samples, these elements should be therefore either reanalysed or the Allende 1 and 2 should be remeasured. This task is planned for the new PGAA facility at FRM-II, which will be described in the next part 3.5 of this chapter.

Hypermet-PC and PEGASE analysis of Allende

To convince the geochemists about correctness of the PGAA analysis of Allende 1 and Allende 2 with the Hypermet-PC, we have re-analysed Allende 1 and 2 with the PEGASE program, which was used for the PGAA data analysis at PSI during 1999-2001. First, we have obtained the calibration values for the Compton-suppressed detector of the Budapest PGAA group, we have fitted the data by a calibration function used by PEGASE (Genilloud, 2000) and inputed those parameters to the virtual data headers, which is required by PEGASE. The results of the comparison between the Hypermet-PC and PEGASE analysis are presented in Figure 3.13 on data of the Allende 1 meteorite. We can see good agreement between the results of both analysing programs for many elements (agreement between H, B, Mg, Al, Si, S, Cl, Ti, Cr, Fe and Co is within 10 %), which confirms the correctness of the PGAA analysis even though it does not agree with the literature values of Jarosewich. Some discrepancies between Hypermet-PC and PEGASE (Na, K, Ca, Mn, Ni and Sm) can be understood from the fact, that behind Hypermet-PC, a large database of many γ-ray energies for each particular element (if they produce many γ-ray energies) is available and many peaks are weighted for the final decision of the element presence and intensity, while the PEGASE program had used mostly only few main peaks for each element to decide about its presence and intensity. Also, the k_0 values differ for some elements and e.g. the amount of Sm and its k_0 value is discussed in this section on page 97. In case of Sm, the k_0 value of PSI is more correct than the one from BNC. For the other elements and their k_0 values, we do not have enough convincing data for similar conclusions.

Dhurmsala meteorite

Dhurmsala (fell in 1860 in Himchal Pradesh, India) is a meteorite of LL6 group, so-called amphoterites. The content of iron usually between 19 – 22 % is characteristic for the LL groups. Also, the LL groups tend to be more composed of fragmented rocks than the other groups of stony meteorites. On the example of the Dhurmsala meteorite, the difference of the PGAA analysis between homogeneous powdered sample and between a piece of Dhurmsala stone with visible grains can be demonstrated. The results were also published by our group (Kudějová et al., 2005b) and they are listed in Table 3.7. They are also displayed for overview in Figure 3.14. Selected elements are compared with literature values compiled by Englert et al. (1986)[11] and by Michaelis et al. (1969)[12]; for other elements, the literature values are not known. The results are normalized to silicon amount in the sample for better comparison with the literature values. The relative uncertainties of the PGAA results are higher because of lower statistics and recalculation of all values to ratio with Si. This procedure also increases

---

[11] Englert et al. (1986) use AMS (Atomic Mass Spectrometry) and both INAA and RNAA for the sample analysis.

[12] Michaelis et al. (1969) use XRF (X-Ray Fluorescence) and atomic absorption for the determination of the elemental concentration in samples.

Z	Dhu Powder (305 mg)			Dhu Rock (855 mg)			Englert			Michaelis
H	0.00398	±	0.0002	0.00401	±	0.0002		-		-
B	<5.9E-06	±	0.23E-06	5.16E-06	±	0.23E-06		-		-
Na	0.041	±	0.002	0.041	±	0.001	0.054	±	0.002	-
Mg	0.83	±	0.06	0.83	±	0.05		-		0.81
Al	0.061	±	0.003	0.053	±	0.003	0.076	±	0.004	0.062
Si	1.00	±	0.04	1.00	±	0.03	1.0	±	0.03	1.0
S	0.130	±	0.008	0.104	±	0.005		-		-
Cl	4.6E-04	±	0.4E-04	2.01E-04	±	0.2E-04		-		-
K	0.0049	±	0.0004	0.0051	±	0.0003		-		0.0048
Ca	0.073	±	0.004	0.072	±	0.003		-		0.070
Ti	0.0038	±	0.0004	0.0037	±	0.0004		-		0.0035
Cr	0.022	±	0.001	0.025	±	0.001		-		-
Mn	0.0152	±	0.0007	0.0150	±	0.0005	0.0138	±	0.0021	0.0136
Fe	0.98	±	0.05	1.03	±	0.04	0.90	±	0.05	1.03
Co	0.0012	±	0.0001	0.0028	±	0.0001		-		-
Ni	0.026	±	0.002	0.060	±	0.003		-		-
Sm	0.8E-06	±	0.2E-06	1.53E-06	±	0.2E-06		-		-
Gd	1.8E-06	±	0.1E-06	2.65E-06	±	0.2E-06		-		-

Table 3.7: Meteorite Dhurmsala homogeneous powder (305 mg, 10284 s) and Dhurmsala grainy stone (855 mg, 6553 s) measured at the PGAA facility in Budapest. The results of the analysis are normalized to Si amount in the sample and compared to the literature values presented by Englert et al. (1986) and by Michaelis et al. (1969).

the uncertainties, but still, they are as good as the literature values. The results generally agree with the literature values, only in case of Na we have detected less than what is given by Englert and the PGAA results in case of Mn are a little larger. The comparison of the powder and rock analysis brings also good agreement except of the elements: S, Cl, Co, Ni, Sm and Gd. Sm and Gd, which are strong absorbers (their non-$1/v$ behaviour was discussed in case of geological standards analysis, see page 97) and the inhomogeneity of the sample could affect correctness of the analysis. The Ni and Co are probably somehow connected within the grains because their amount in the Dhurmsala rock is about 2.3 times higher than for the Dhurmsala powder. To study those effects in detail, more diverse samples would be necessary.

Morávka meteorite

At the time of the Budapest experiment with small amounts of meteorites, in 2003, bulk composition of the Morávka meteorite was not yet known so we did not have any data for comparison. However, in the same year, very interesting and comprehen-

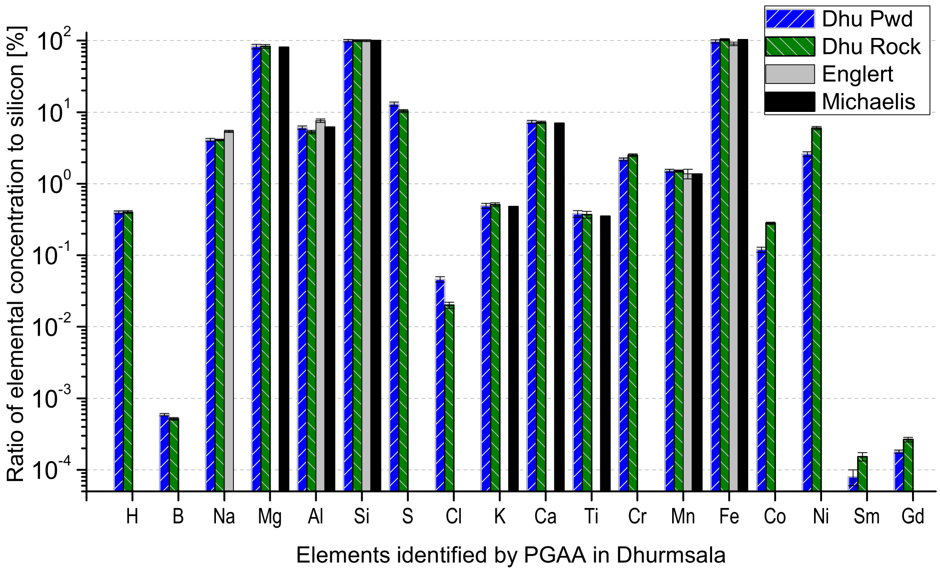

Figure 3.14: PGAA results of Dhurmsala homogeneous powder (305 mg, measured for 10284 s) and Dhurmsala grainy stone (855 mg, 6553 s) measured at the PGAA facility in Budapest in 2003.

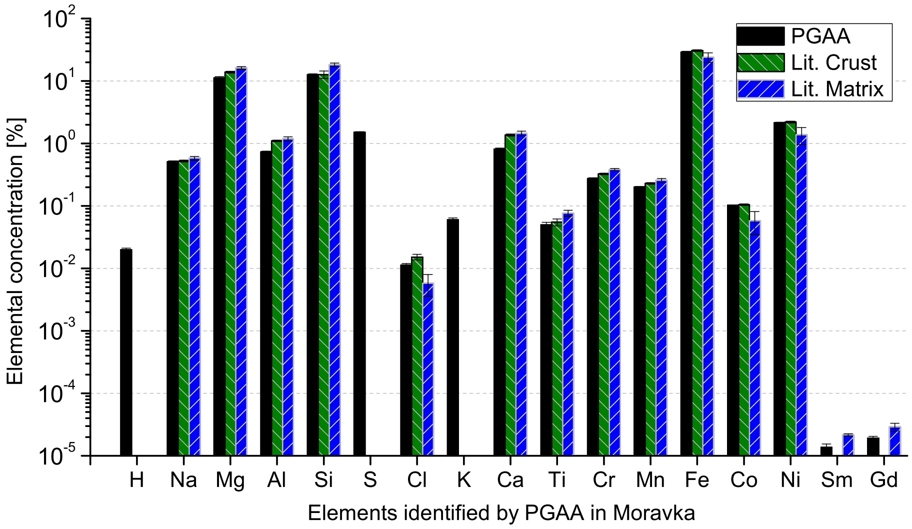

Figure 3.15: PGAA results of the homogeneous powder of Morávka meteorite (125 mg, 40000 s), measured at the PGAA facility in Budapest in 2003. The results of the analysis are compared to the literature values presented by Borovička et al. (2003). The concentrations of the majority of elements analysed by the PGAA technique correspond better to the Ablation Crust than to the meteorite bulk analysis (matrix).

Elm	Morávka PGAA [%]	Borovička: Crust [%]	Borovička: Bulk [%]	Anal. Meth.[1]
H	0.020 ± 0.001	-	-	
B	<0.0001	-	-	
Na	0.511 ± 0.013	0.523 ± 0.016	0.582 ± 0.038	1
Mg	11.20 ± 0.59	13.86 ± 0.42	16.17 ± 0.81	1, 2
Al	0.729 ± 0.025	1.100 ± 0.033	1.189 ± 0.089	1
Si	12.66 ± 0.31	12.7 ± 1.7	18.1 ± 1.2	3
S	1.51 ± 0.036	-	-	
Cl	0.0113 ± 0.0007	0.0152 ± 0.0016	0.0058 ± 0.0022	1
K	0.0598 ± 0.0046	-	-	
Ca	0.810 ± 0.035	1.364 ± 0.050	1.45 ± 0.12	1, 2
Ti	0.0497 ± 0.0050	0.055 ± 0.007	0.0770 ± 0.0083	1, 2
Cr	0.2732 ± 0.0085	0.325 ± 0.010	0.383 ± 0.015	1
Mn	0.2008 ± 0.0038	0.229 ± 0.007	0.256 ± 0.019	1, 2
Fe	29.13 ± 0.68	30.680 ± 0.940	24.0 ± 4.2	1
Co	0.1025 ± 0.0017	0.105 ± 0.003	0.058 ± 0.023	1
Ni	2.151 ± 0.037	2.200 ± 0.070	1.38 ± 0.42	1, 2
Sm	13.6E-06 ± 1.9E-06	N.A.[2]	21.7E-06 ± 0.9E-06	4
Gd	19.1E-06 ± 1.3E-06	N.A.	29.0E-06 ± 4E-06	4

Table 3.8: Homogeneous powder of Morávka meteorite (125 mg) was measured for 40000 s at the PGAA facility in Budapest in 2003. The concentration determined by PGAA was then compared to comprehensive literature values published by Borovička et al. (2003). The authors give a precise analysis of the meteorite Ablation Crust (middle column) and meteorite Bulk composition (right column). In the last column, the method of a particular analysis for the literature values is listed. The PGAA analysis gives results very similar to the ablation crust composition.

[1] 1=INAA (Instrumental Neutron Activation Analysis); 2=IPAA (Instrumental Photon Activation Analysis); 3=IFNAA (Instrumental Fast Neutron Activation Analysis); 4=RNAA (Radiochemical Neutron Activation Analysis)

[2] N.A. = not analysed

sive description and a precise analysis of the meteorite was published in Meteoritics & Planetary Science 38, by Borovička et al. (2003). The authors have used 4 methods based on Activation Analysis to determine the Morávka meteorite composition of its bulk, crust and metallic grains: INAA (Instrumental Neutron Activation Analysis), IFNAA (Instrumental Fast Neutron Activation Analysis), RNAA (Radiochemical Neutron Activation Analysis), and IPAA (Instrumental Photon Activation Analysis). For the analysis of the meteorite bulk, samples of masses between 13 and 500 mg were used. For the determination of the meteorite ablation crust, only 13.1 mg were used, therefore many trace elements were not analysed when compared to the sample bulk.

For the PGAA measurement, we had available only 125 mg of the Morávka sample homogenized powder, so we have measured the sample for longer time: 40000 s. The amount of 125 mg was too low for detection of boron in the sample, we could only deduce, that it was less than $1\,\mu$g/g. Our results are listed in Table 3.8 and they are compared to the analysis of the Morávka crust and bulk by the authors Borovička et al. (2003). We found also interesting to name in the Table 3.8 particular methods, which were used for the elemental analysis by the authors. Since the silicon amount of the PGAA analysis and the INAA analysis of the sample ablation crust were identical, we have not recalculated the elemental concentration to the amount of silicon in the sample. In the Table 3.8, we can see, that the PGAA analysis of the Morávka sample gives very similar results with the composition of the meteorite ablation crust, so we can deduce, that our sample consisted mostly from this part of the meteorite. The results are also graphically represented in Figure 3.15. For many elements, we have determined lower concentration than given by Borovička et al. (2003): Mg, Al, Ca, Cr, Mn, Sm and Gd. Sm and Gd must be treated separately as the non-$1/v$ elements, but to have some explanation for the disagreement for the rest of the listed elements, another measurement would be necessary[13].

Boron in volcanic samples

The determination of boron content in volcanic rocks is an important application in geochemistry. Among all elements, boron is a very good candidate for studies and evaluation of the mass transport at the subduction zones. The advantages of the PGAA analysis with the fast and accurate determination of boron concentration in volcanic rocks are presented by Sano et al. (1999).

Therefore, the last example of the measurement at the PGAA facility at BNC was focused to the boron amount in geological samples – volcanic materials and stones. Three volcanic stones different by their structure and density were collected in the crater of the same long time inactive and extinct volcano Kalem in the Eifel region close to Cologne. The boron content was determined and compared within each other in Table 3.9. One volcanic stone was collected in the neighbour inactive and extinct volcano Rother Kopf and the question was, how much differ the amount of boron in

---

[13] This is the advantage of PGAA: if we need to remeasure exactly the same sample, we can do it. With chemical methods we do not have this possibility.

Figure 3.16: 4 volcanic stones from extinct volcano Kalem and Rother Kopf in Eifel region and 2 coloured stones collected from river bed in Himalaya.

this sample with those from Kalem. For curiosity, two coloured stones from Himalayan region were analysed and the concentration of boron was determined. These results are listed in Table 3.10.

The amount of boron in the volcanic samples was about 2 – 3 times higher in the porous material than in the firm material and both porous samples Kalem 2 and Rother Kopf contained similar amount of boron. Quite a large amount of boron was found in Green Stone (Table 3.10), and also higher amount of boron in red stone when compared to volcanic samples. All six samples are shown on picture in Figure 3.16. For comparison, some of the other analysed elements are included in Tables 3.9 and 3.10.

Element		Kalem 1 [%]			Kalem 2 [%]			Kalem 3 [%]		
H		0.430	±	0.007	0.473	±	0.007	0.318	±	0.006
B	[$\mu g/g$]	1.39	±	0.02	3.70	±	0.06	1.81	±	0.03
Na		1.03	±	0.02	0.83	±	0.02	1.12	±	0.03
Mg		5.8	±	0.3	6.5	±	0.4	4.5	±	0.3
Al		5.4	±	0.2	5.8	±	0.1	4.3	±	0.1
Si		13.9	±	0.4	15.9	±	0.6	12.2	±	0.3
Cl	[$\mu g/g$]	50	±	7	221	±	10	164	±	9
K		0.83	±	0.02	0.87	±	0.02	1.10	±	0.03
Ca		7.9	±	0.2	9.2	±	0.3	6.6	±	0.2
Ti		1.5	±	0.2	1.63	±	0.08	1.19	±	0.06
Mn	[$\mu g/g$]	1300	±	30	1512	±	40	926	±	20
Fe		6.6	±	0.1	7.4	±	0.2	5.7	±	0.1
Sm	[$\mu g/g$]	6.6	±	0.2	7.0	±	0.2	4.9	±	0.1
Gd	[$\mu g/g$]	6.6	±	0.3	6.8	±	0.3	4.3	±	0.2

Table 3.9: Volcano stones from Eifel region analysed by PGAA in Budapest, 2003 in intercomparison. All three stones were collected at the same volcano Kalem, their pictures are presented in Figure 3.16. Porous material contains higher concentration of boron.

Element		Rother-Kopf [%]			Green Stone [%]			Red Stone [%]		
H		0.119	±	0.002	0.113	±	0.002	0.056	±	0.001
B	[$\mu g/g$]	3.30	±	0.04	14.8	±	0.1	5.22	±	0.06
Na		0.87	±	0.02	0.64	±	0.01	<0.033	±	
Mg		3.1	±	0.2	0.30	±	0.05	0.29	±	0.08
Al		3.11	±	0.07	2.88	±	0.06	0.54	±	0.03
Si		10.0	±	0.2	16.2	±	0.4	1.06	±	0.04
Cl	[$\mu g/g$]	56	±	3	17	±	2	37	±	3
K		1.50	±	0.03	1.48	±	0.03	0.21	±	0.01
Ca		5.1	±	0.1	0.10	±	0.01	9.4	±	0.3
Ti		0.97	±	0.10	0.17	±	0.02	0.034	±	0.003
Mn	[$\mu g/g$]	921	±	20	44	±	6	530	±	20
Fe		4.56	±	0.09	1.50	±	0.03	8.6	±	0.2
Sm	[$\mu g/g$]	4.17	±	0.09	2.22	±	0.04	3.51	±	0.07
Gd	[$\mu g/g$]	4.2	±	0.2	2.15	±	0.08	5.5	±	0.2

Table 3.10: One volcanic stone also from the Eifel region from Rother-Kopf can be compared to the three samples collected at the volcano Kalem nearby. This material was again very porous and it contained larger amount of boron as in the case of Kalem 2 sample. The other two stones, green stone and red stone were collected in dried river-bed in Himalaya region.

3.5 PGAA instrumentation at FRM-II

The research reactor II (FRM-II) in Garching by Munich offers a great opportunity for building there one of the best PGAA instruments world-wide. The PGAA facility will be built in the neutron-guide hall (NL-hall) at the end of the NL4b cold neutron guide about 50 m far from the reactor core. The start of the PGAA measurements is planned for the beginning of the year 2006. Because the lowest possible γ-ray background during the measurements with the PGAA installation is essential for the best achievable limits of detection, the whole PGAA facility will be shielded from the surrounding instruments by a concrete bunker. Of course, at the same time the intensive gamma-rays from the PGAA (n,γ) capture reactions will be shielded from inside and so, together with a proper lead shielding around the detection system, the bunker will help to keep low the overall background in the NL-hall, what is also an essential task to be fulfilled.

The PGAA instrument has been moved to the FRM-II together with a cold neutron tomography set-up and with complete shielding including a concrete bunker of ca. $6 \times 3.25\,\mathrm{m}^2$ from PSI, Switzerland, where the PGAA facility was successfully operating during the years 1997 – 2002. The PGAA instrument is now being re-designed for different conditions in the neutron guide hall (NL-hall) at the FRM-II. As well, the definite space inside of the concrete bunker is being essentially re-arranged for four different experimental set-ups that we want to operate in interchange there: 1. standard PGAA instrument with a beam size of about $2 \times 2\,\mathrm{cm}^2$, 2. cold neutron tomography set-up with homogenized and parallelized neutron beam (with dimensions of about $4 \times 3\,\mathrm{cm}^2$), 3. position sensitive PGAA and 4. a new compact four HPGe-array with Compton suppression for nuclear structure experiments – both 3. and 4. with the use a focused and collimated neutron beam with a size of $1 \times 1\,\mathrm{mm}^2$. The choice of the inner coating of the neutron guide and especially the design of the neutron guide has been extensively studied with the help of the neutron ray-trace simulation package McSTAS (Willendrup et al., 2004). The most important and comparative results the simulation will be demonstrated and discussed in this chapter, the best common solution for all four instruments will be proposed. Following the simulations, we can draw some particular expected parameters: We expect to have at least 20 times higher cold neutron flux – $3 \cdot 10^9\,\mathrm{n/cm^2s}$ at FRM-II than at PSI and therefore at least about 4 times better limits of detection than we had with the PGAA instrument at PSI. Additionally, we want to design the most convenient method to focus the neutrons to a spot of about $1 \times 1\,\mathrm{mm}^2$ and to develop a position sensitive PGAA and PGAI (PGAA - Imaging). Many general details about the research reactor II and the instrumentation at the FRM-II can be found on the web page of FRM-II (2005).

3.5.1 PGAA station at FRM-II

The PGAA station is well defined by the concrete bunker with 3.25 m outer width and 5.94 m maximal outer length. It will be placed at the end of the NL4b beam

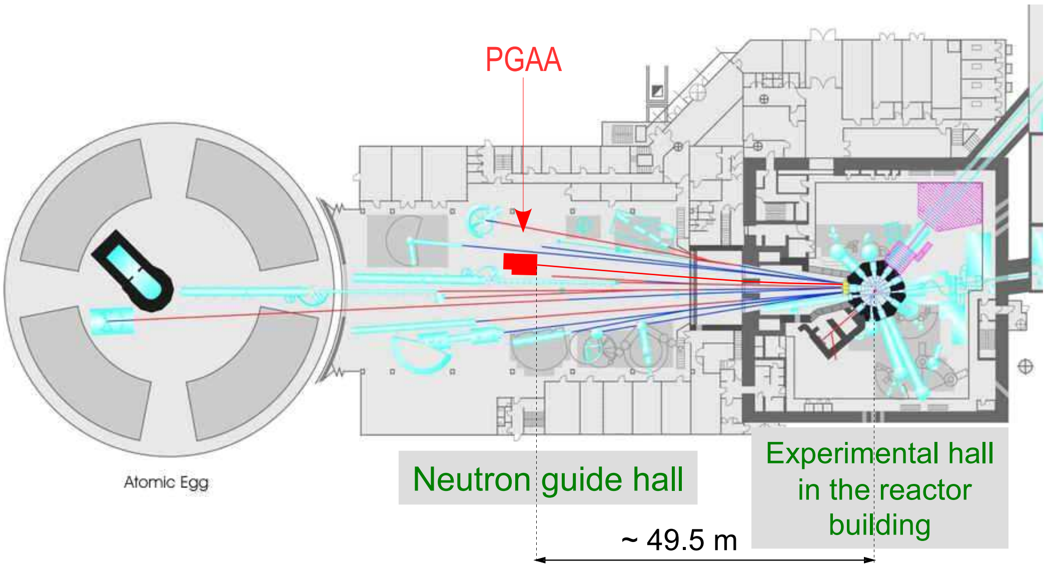

Figure 3.17: Schematic drawing of the neutron guide hall (NL Hall) at the FRM-II research reactor. The space reserved for the PGAA bunker is shown in the middle.

guide (see Figure 3.17). NL4b part of the NL4 beam guide splits from the NL4a to the right about 4.5 m from the Cold Source of neutrons, it is at the beginning of its curved part. NL4a continues straight way from the Cold Source, with its middle axis on the so-called zero-line, which is also used as a reference direction for the NL4b calculations. The NL4 beam guide begins at the zero line by a SR1 conical guide looking with its nose at the Cold Source.

3.5.2 NL4b cold neutron beam guide

The space reserved for the PGAA bunker in the neutron-guide hall is very limited and the NL4b neutron guide had to be designed so, that it enters the PGAA bunker wall close to its middle (see Figure 3.17). To use the space most profitably, the long wall of the bunker will be parallel and stuck to the neighbour beam guide NL5 (beam guide to the right from the direction of incoming neutrons). The consequence is that the NL4b does not enter the bunker at 90 °, but at ca. 88 °.

Bender

To bring the beam guide to the middle position of the space reserved for the PGAA bunker, quite a strong curvature of the bent part, so-called bender, had to be chosen: the radius of curvature R is 390 m. The bender will be 41.29 m long and followed by a straight neutron guide about 5 m long. The profile of the NL4b guide is 110 mm high and 50 mm wide. The inner walls of the bender will be supermirrors with Ni-Ti

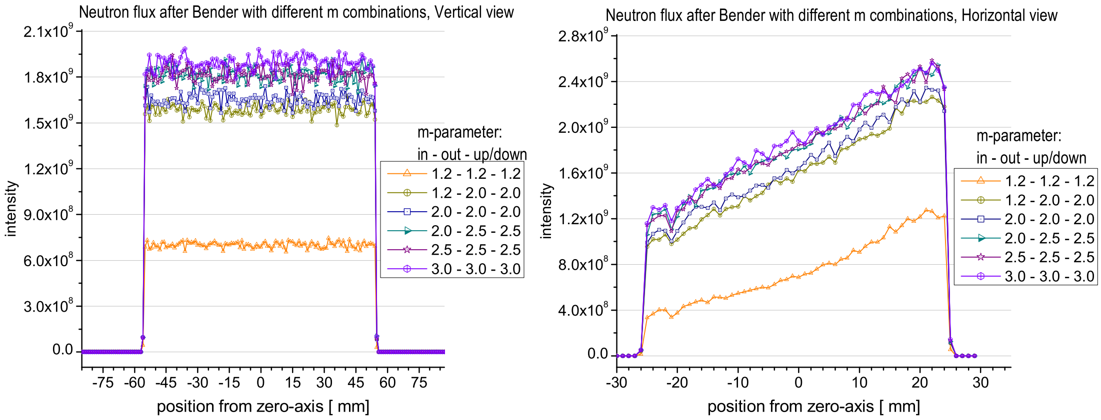

Figure 3.18: Comparison of the neutron flux after leaving the 41 m long Bender with the radius of curvature R=390 m in vertical and horizontal view. The legend in the boxes means a combination of m values, which were used for each curve: e.g. 1.2 – 2.0 – 2.0 means supermirror coating with parameter m=1.2 at inner wall, m=2.0 at outer wall, m=2.0 at upper and down walls. The use of 1.2 – 2.0 – 2.0 in comparison to 1.2 – 1.2 – 1.2 brings a yield of 125 %, the use of 2.0 – 2.5 – 2.5 instead of 1.2 – 2.0 – 2.0 would bring additional 14 % yield.

coating. The supermirror coating has the parameter m=2.0[14] for upper, outer and bottom surface and m=1.2 for the inner surface of the guide. In was not needed to use here m=2.0, since this parameter does not increase the neutron flux at the target position according to our simulations (Materna, 2004) with the Monte Carlo simulating program McSTAS (Willendrup et al., 2004). The simulated neutron flux intensity at the end of the bender in dependence on the combination of m values, which rise with the total-reflecting angle of the supermirror coating is shown in Figure 3.18.

We can draw important conclusions from the results presented in Figure 3.18: The coating of the inner wall of the bender is of lower importance and can stay m=1.2[15] while all the other walls are coated with supermirror coating with m=2.0. This increases considerably the neutron flux at the end of the bender when compared to m=1.2 at all walls of the bender: the gain in the neutron flux at the end of the bender is 125 %. The same comparison can be applied for higher m values, only the increase of the neutron flux is not so large from the point of view of PGAA

---

[14] The parameter m is determined by the material of the total-reflecting layers, their sequence and their number. The parameter m gives the multiplication of the critical angle of total-reflection when compared to a single-layered Ni-one, when m=1. For m=0, the reflectivity of the material is zero.

[15] this result was to some extend expected, because the neutrons hit the inner wall always under smaller angles than the other walls and the probability of being reflected is thus higher also without increasing the m of the coating.

experiments, about 14 %[16] when we compare the combination of m=1.2 on inner wall, m=2.0 at outer, upper and down wall with m=2.0 at inner wall, m=2.5 at the outer, up and down. The absolute intensity of these simulations can not be compared with the intensity of Figures 3.23 to 3.27 because the Cold Source distribution for present calculations of the bender was an expected distribution, while for the Figures 3.23 to 3.27 the Cold Source distribution was already measured and described and it should better correspond to the expected neutron flux in the NL4b neutron guide.

The bender is once interrupted after 16.25 m by the so-called fast shutter with 13 mm thickness and second time after next 6 m by the instrument shutter with a thickness of 8 cm.

Instrument shutter

We will control remotely this shutter and use it for closing and opening the neutron beam. Therefore, the instrument shutter must stop all the neutrons and produced γ-rays so we can work safely in the PGAA bunker. To determine the thickness and composition of the shutter, the intensity and energy distribution of the neutron flux at its position must have been simulated. For reliable simulation of the requested parameters, the Cold Source neutron distribution and intensity must be well defined. After first real experiments at the FRM-II in summer 2004, the expected parameters of the Cold Source were replaced with parameters describing properly the real Cold Source. The Cold Source definition was created and prepared for McSTAS simulation by Andreas Ostermann (2005) and we have obtained those data available for our own simulations of NL4b guide. Since we suppose, that the NL4a has very similar neutron spectrum at the length equal to the position of the NL4b instrument shutter, we have compared in cooperation with A. Ostermann the neutron intensity at the NL4a and NL4b beam guide. We have obtained the same resulting intensity of $3.1 \cdot 10^9$ n/cm^{2}s with only 3 % difference caused by different geometrical conditions of both neighbouring beam guides.

The simulated neutron intensity and energy distribution at the position of the instrument shutter helped to design its shielding material and thickness necessary to stop all the neutrons and to reduce the intensity of the created γ-rays below the safety level, so we can work in the PGAA bunker when the instrument shutter is closed.

3.5.3 Simulations for the PGAA station at FRM-II

The most interesting and challenging part of the work on the PGAA station[17] design at FRM-II is the proposal of the final arrangement and location of all four experimental set-ups which we want to run in interchange and sometimes as experiments with complementary information about the measured sample. In fact, the requirements for

---

[16] 14 % increase of neutron flux is not so substantial for the PGAA experiments, but it is already important gain e.g. for neutron scattering experiments.

[17] By the term PGAA station is meant the space occupied by the PGAA bunker including all four instrumental set-ups, which we want to place inside of the bunker.

the best experimental conditions for all four set-ups can contradict each other:

1. **Standard PGAA:** Approximate beam size $2 \times 2\,\mathrm{cm}^2$; divergence of the beam is not of high importance.
2. **Position Sensitive PGAA:** Approximate beam size $1 \times 1\,\mathrm{mm}^2$; divergence of the beam should be reduced by e.g. ^{6}LiF collimator to define well the volume of the measured point in the sample. The intensity of the neutron flux should be maximal possible.
3. **Ge Array:** Approximate beam size $1 \times 1\,\mathrm{mm}^2$; divergence of the beam is not of high importance. The intensity of the neutron flux should be maximal possible.
4. **Cold Neutron Tomography:** Approximate beam size $6 \times 4\,\mathrm{cm}^2$; divergence of the beam is very important. It must be reduced to the possible minimum, at the costs of the loss in the neutron flux intensity because the ideal case for the reconstruction of any 3D tomography data is either a parallel beam with $0\,^\circ$ divergence or a point like source of the radiation with isotropic emission in space. Only in these two cases mathematical models for the reconstruction of the 3D sample images have an analytical solution.

One common conclusion can be drawn out from these four requests: the beam size of NL4b, 110 mm × 50 mm, is too large for our needs and therefore, the area can be either 1) reduced by a ^{6}LiF collimator to the requested area or 2) the neutron beam guide can be someway tapered to the requested dimensions. To evaluate all possible solutions, we have used the Monte-Carlo simulation program McSTAS (Willendrup et al., 2004).

Parameters of interest Based on the request of the 4 different experiments listed above, we were interested in:

- resulting beam area of interest **V×H** in [mm^2]: Vertical × Horizontal size at the target position
- The neutron flux **n-flux** in [n/cm^{2}s] of the beam area of interest (Vertical × Horizontal) at the target position and at varied distances **Z** in [cm] from the neutron-guide exit. Neutron-guide exit gives zero distance reference Z=0 cm.
- Total number of neutrons **n-total** in [n/s] at the target position
- Divergence of the neutron beam **Div H** and **Div V** in both horizontal and vertical directions at varied distances Z from the neutron-guide exit

beam divergence

In the special case of neutron guides, the divergence Θ_C of the neutron beam is determined by the critical angle for total reflection γ_C by a simple relation: $\Theta_C = 2{\cdot}\gamma_C$. The γ_C is dependent on the neutron wavelength λ and the parameter m, describing the supermirror surface. Approximately, the following relation is valid: $\gamma_C = m{\cdot}0.1°{\cdot}\lambda\,[\text{Å}]$. The average wavelength of our cold neutron spectrum is 4.5 Å, the longest part of our neutron guide is covered by m=2 supermirror, therefore we expect divergence Θ_C of about 1.8 ° at the end of the beam guide. For any kind of tomography, this is an unacceptably high value and we have to decrease it to an acceptable divergence angle of about 0.9 ° by putting our tomography set-up far from the neutron beam guide exit. Other parameters of the neutron flux are important to make the tomography possible but their discussion is outside of the scope of this thesis. Generally, we do not expect in any case to have a competitive cold neutron tomography set-up and so the priority for optimisation was put on the neutron beam focusing. Nevertheless, the cold neutron tomography should be possible, since we want to have complementary information about the PGAA samples to decide, which parts of their volumes are interesting for the position sensitive PS-PGAA.

choice of the beam guide

The recent rapid development in technologies of supermirrors (Böni, 2000) and of the sputtering processes of the Ti-Ni total-reflecting layers allows the parameter m to be more than 3 even on non-linear surfaces. This fact gave us the opportunity to think about several solutions of a tapered beam guide at the end of the NL4b. The "Taper" focuses the neutrons onto a smaller beam-size area, which then depends on the exit dimensions of the Taper and on its geometry. Very interesting contributions to this topic were recently published by Schanzer et al. (2004) and by Hils et al. (2004). The results of those articles and fruitful consultations with Prof. P. Böni during 2004 and 2005, made us interested in comparing different solutions for the NL4b straight end part. They include elliptical and parabolic tapering, which could fulfill the complex requirements of the four different experimental set-ups: An extensive simulation study was performed with very different parameters, set-ups and target positions of the four instruments at the end of the NL4b and with different geometry of the beam guide, (see Kudějová et al. (2005b)). During the analysis of many possible sets of parameters, we have gathered good experience and understanding of the solutions and of their feasibility. Some solutions were put aside because of the disadvantageous results of the simulations, some were rejected because they were nonproductive. In the comparison between elliptical and parabolic taper, the elliptical one gave better results in neutron flux intensity under the same conditions than the parabolic one. Therefore, for the next simulations, only elliptical guides are compared.

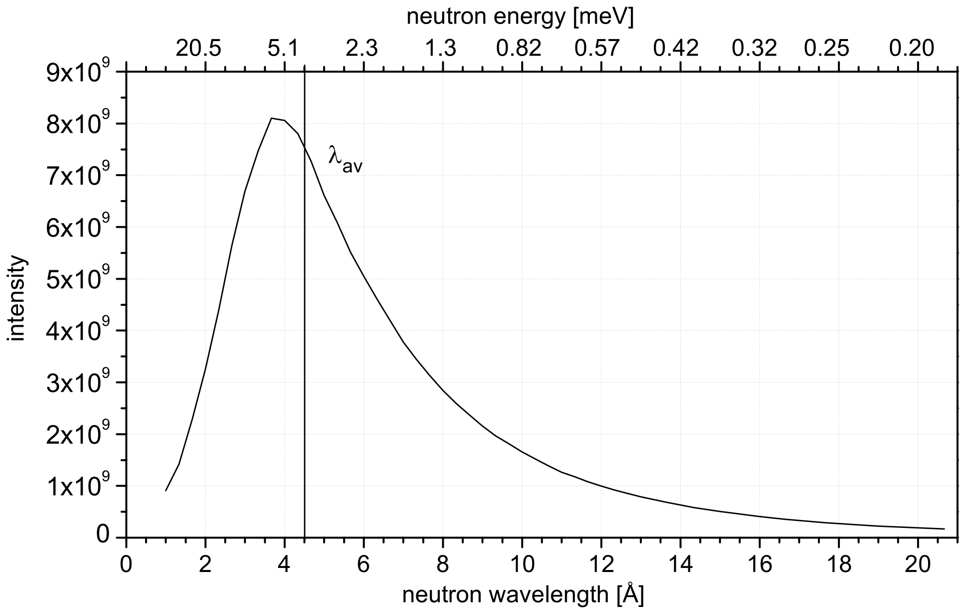

Figure 3.19: The neutron wavelength distribution at the end of the NL4b with the elliptical taper 4400 mm long and m=3. The neutron average wavelength is 4.5 Å which corresponds to the average neutron energy of 4 meV.

3.5.4 Results of the McSTAS simulations

To see the advantages and disadvantages of the elliptical taper, we have compared it with a simple linear taper, which has the same output dimensions and with a not tapered beam guide of the same length. After several simulations, three possibilities for the last 5 – 6 m of the straight end part of the NL4b beam guide were chosen for comparison and they will be discussed here:

1. Common, not tapered guide with m=2.0, 2.5, 3.0 as a “standard” for comparison of gain in neutron flux intensity and for the loose in divergence of the neutron beam when using other solution than this simplest one.
2. Elliptically tapered guide with m=2.0, 2.5, 3.0 with such geometry to focus the neutrons to a very small spot for the applications with $1 \times 1\,\mathrm{mm}^2$ beam size – PS-PGAA and Ge Array.
3. Linearly tapered guide with m=2.5, 3.0 with the same taper exit dimensions as the elliptical taper for direct comparison.

Neutron distribution at the target position As one result of the McSTAS simulation, Figure 3.19 gives the expected neutron wavelength distribution at the exit of NL4b with the 4400 mm long elliptical taper. The neutron energy – or wavelength

– distribution is important for the knowledge of the neutron capture cross-section σ_c. This distribution does not differ substantially for different tapers and distances Z from the taper exit, because the neutron distribution at the end of NL4b is mainly influenced 1) by the neutron distribution of the Cold Source entering the NL4 beam guide and 2) by the curvature of the bender, R=390 m. The most probable wavelength λ_p according to the latest simulations is 4.0 Å, so the average wavelength λ_{av} is 4.5 Å, which corresponds to the average neutron energy of 4 meV.

Elliptical vs. Linear and No Taper

The proposed Elliptical Taper from the McSTAS simulations is sketched in Figure 3.20.

The Elliptical Taper is parametrized by the taper length TL, the input dimensions $110 \times 50\,\mathrm{mm}^2$ and by a focal point at the taper end F2 (focal point F1 is set far away, because more precisely we use only half of the ellipse). This set of parameters determines also the output dimensions of the elliptical taper (for TL = 5650 mm, we have chosen F2=50 mm, which means that the neutrons should be best focused at Z=5 cm from the taper exit. The calculated exit dimensions of the taper, following the analytical formula for ellipse, give size of $14.6 \times 6.6\,\mathrm{mm}^2$ at TL = 5650 mm). As illustrated in Figure 3.20, the Elliptical Taper will be interrupted after 4.40 m or 4.65 m and the standard PGAA target position will be placed in the focus of the neutron beam leaving the taper, Z is ca. 30 – 40 cm from the taper exit window. For cold neutron tomography, this tapered end will be also utilized and the Tomography set-up will be placed ca. 2 – 3 m after the exit. Then, for PS-PGAA and Ge Array, a removable elliptical taper part will be added to the existing taper, well adjusted and the neutrons will be so focused to a spot smaller than 1 cm^2. With a ^{6}LiF collimator, neutron beam of $1 \times 1\,\mathrm{mm}^2$ will be selected. To prove or disprove the competency of the solution with such an elliptical taper, selected results of the McSTAS simulations follow in Tables 3.11 and 3.12.

The Linear Taper with the same exit window dimensions of $14.6 \times 6.6\,\mathrm{mm}^2$ as for Elliptical Taper to obtain good comparison with the elliptical solution is presented in Figure 3.21. The Linear Taper will be interrupted after 4.40 m or 4.65 m to check the conditions of the n-flux in comparison to the elliptical one. The conditions, which offers the Linear Taper for the cold neutron tomography instrument will be compared with the Elliptical Taper and with No Taper. Parameters outlined in both Figures 3.20 and 3.21 are used.

Selected results of all performed simulations for the three solutions of the NL4b are summarized in Table 3.11 (No Taper and Linear Taper) and in Table 3.12 (Elliptical Taper). For the case of the Linear and the Elliptical Taper, the taper length **TL** of 4400 mm or 4650 mm for standard PGAA and 5650 mm for PS-PGAA or Ge Array, was used; for the case of No Taper, a length TL = 4400 mm was chosen. The parameter of total-reflection **m** was varied for the simulations among m=2.0, m=2.5 and m=3.0 as listed above. The beam-size at the exit window $\mathbf{H}_0 \times \mathbf{V}_0$ (at Z=0 cm

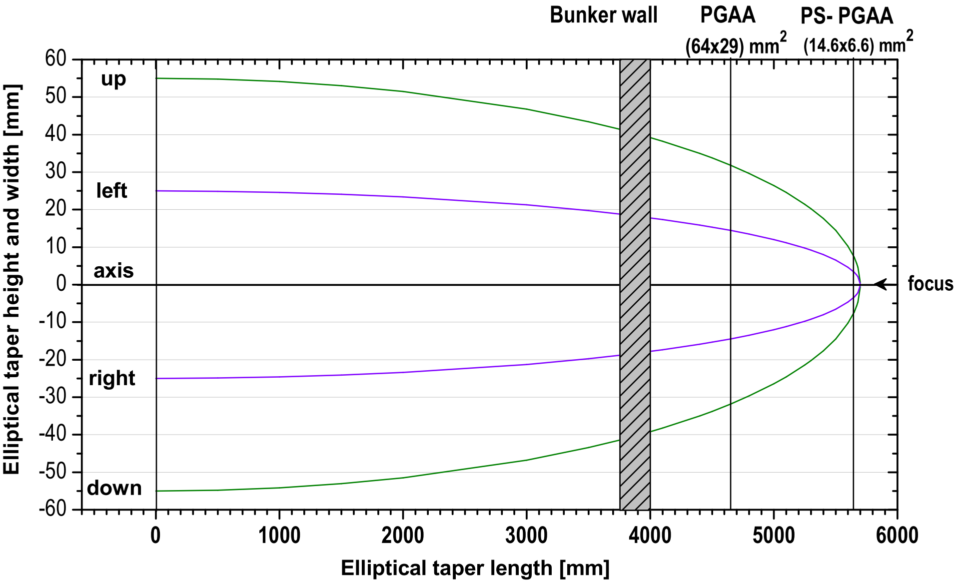

Figure 3.20: Proposal of the elliptically tapered beam guide end of the NL4b for the latest McSTAS simulations with a geometry corresponding to the taper length TL = 5650 mm with the focal point F2=50 mm after the taper exit window.

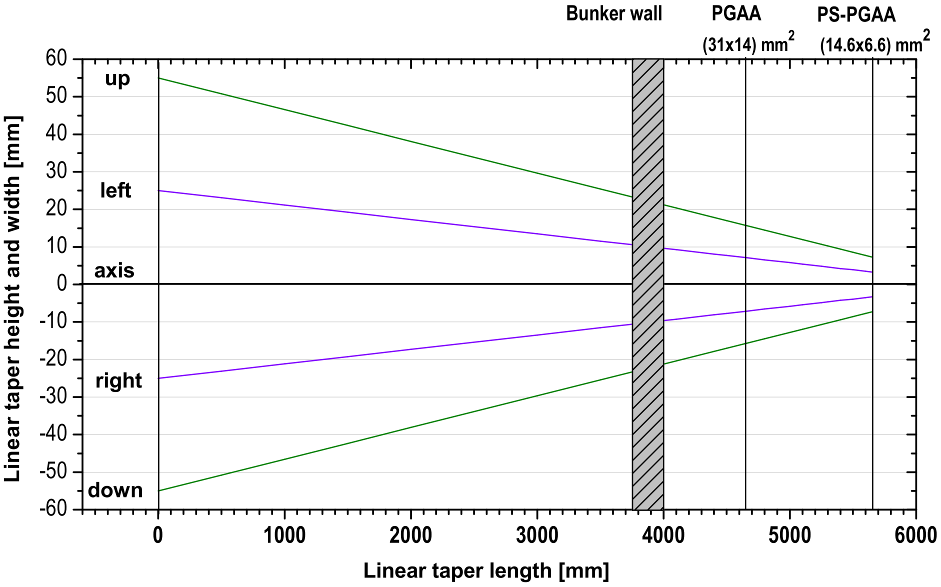

Figure 3.21: Linearly tapered beam guide end of the NL4b for the latest McSTAS simulations with a geometry corresponding to the proposed elliptical taper with the length TL = 5650 mm and with the focal point F2=50 mm after the taper exit window, see Figure 3.20 for comparison.

No Taper input: 55 cm^2	TL [mm]	Z [cm]	Out [V×H] [mm×mm]	n - flux [n/cm^2/s]	n - total [n/s]	div H [deg]	div V [deg]
m=2.0	4400	0	110×50	2.80E+09	1.54E+11	(-0.8; 0.2)	±0.9
exit: 55 cm^2		**100**	**70×28**	**2.90E+09**	1.44E+11	(-0.8; 0.2)	±0.9
m=2.5	4400	0	110×50	2.80E+09	1.54E+11		
m=3.0	4400	0	110×50	2.79E+09	1.53E+11		
Linear taper input: 55 cm^2							
m=2.5	4400	0	35.7×16.2	1.11E+10	6.39E+10		
exit: 5.78 cm^2		**10**	**20×9**	**1.10E+10**	6.39E+10		
		15	20×9	1.10E+10	6.39E+10		
		100	40×30	2.00E+09	5.55E+10	(-1.3; 1.3)	±1.8
		200	60 x40	7.00E+07	3.45E+10	(-0.8; 0.8)	±1.2
m=2.5	5650	0	14.6×6.6	1.26E+10	1.20E+10		
exit: 0.96 cm^2		2	7×4	1.20E+10	1.20E+10		
		3.5	**7×4**	**1.20E+10**	1.20E+10		
		10	7×4	1.05E+10	1.20E+10	large	large
		50	30×20	1.50E+09	1.19E+10		
m=3.0	4400	0	35.7×16.2	1.31E+10	7.59E+10		
exit: 5.78 cm^2		10	20×9	1.33E+10	7.59E+10		
		15	**20×9**	**1.30E+10**	7.59E+10		
		100	40×30	2.10E+09	6.32E+10	(-1.3; 1.3)	±1.8
		200	60×40	6.20E+08	3.72E+10	(-0.8; 0.8)	±1.2
m=3.0	5650	0	14.6×6.6	1.53E+10	1.47E+10		
exit: 0.96 cm^2		**2**	**8×5**	**1.50E+10**	1.47E+10		
		3.5	8×5	1.45E+10	1.47E+10		
		50	20×20	1.50E+09	1.47E+10	large	large

Table 3.11: No Taper and Linear Taper: selection from the McSTAS results. TL is the taper length; Z is the distance of the monitored neutron-flux (n-flux) from the taper exit; Out [V×H] is an acceptable surface area of the neutron beam (Vertical×Horizontal) at the distance Z if the target position of (PS)-PGAA or CN-Tomography was there – the values are obtained from graphical results; n-total is the total number of neutrons monitored – the values are obtained from the McSTAS output file and they depend on the monitor surface, which is strictly kept the same; div H resp. div V is divergence in horizontal resp. vertical direction. The emphasized values of neutron flux correspond to the best conditions from each set of distances Z. ±1.2 means interval of divergence (-1.2; 1.2).

Elliptical t. input: 55 cm^2	TL [mm]	Z [cm]	Out [V×H] [mm×mm]	n - flux [n/cm^2/s]	n - total [n/s]	div H [deg]	div V [deg]
m=2.0	4400	0	69.9×31.8	5.22E+09	1.16E+11		
exit: 22.2 cm^2		25	38×15	7.05E+09	1.16E+11		
F2: 1300 mm		**30**	**38×15**	**7.10E+09**	1.16E+11		
		40	38×15	7.20E+09	1.16E+11		
		200	60×50	1.67E+09	7.81E+10	(-0.8; 0.1)	±1.0
m=2.0	5650	0	14.6×6.6	1.38E+10	1.33E+10		
exit 0.96 cm^2		**7**	**7×4**	**1.70E+10**	1.31E+10		
F2: 50 mm							
m=2.5	4400	0	69.9×31.8	6.01E+09	1.34E+11		
exit: 22.2 cm^2		25	32×15	8.20E+09	1.34E+11		
F2: 1300 mm		**30**	**32×15**	**8.40E+09**	1.34E+11		
		40	32×15	8.40E+09	1.34E+11		
		100	32×30	5.00E+09	1.24E+11	(-0.9; 0.2)	±1.3
		200	60×50	2.00E+09	8.69E+10	(-0.9; 0.2)	±1.2
m=2.5	4650	0	63.6×28.9	6.83E+09	1.26E+11		
exit: 18.4 cm^2		**25**	**32×15**	**9.60E+09**	1.26E+11		
F2: 1050 mm		30	32×15	9.60E+09	1.26E+11		
		100	40×30	4.60E+09	1.15E+11	(-0.9; 0.2)	±1.3
		200	60×50	1.50E+09	7.73E+10	(-0.9; 0.2)	±1.2
m=2.5	5650	0	14.6×6.6	1.91E+10	1.83E+10		
exit: 0.96 cm^2		5	7×4	2.35E+10	1.83E+10		
F2: 50 mm		**7**	**7×4**	**2.30E+10**	1.83E+10		
m=3.0	4400	0	69.9×31.8	6.33E+09	1.41E+11		
exit: 22.2cm^2		30	32×15	9.10E+09	1.41E+11		
F2: 1300 mm		**40**	**32×15**	**9.20E+09**	1.41E+11		
		200	60×50	1.90E+09	9.09E+10	(-0.9; 0.2)	±1.2
m=3.0	4650	0	63.6×28.9	7.33E+09	1.35E+11		
exit: 18.4 cm^2		25	36×15	1.06E+10	1.35E+11		
F2: 1050 mm		**30**	**36×15**	**1.07E+10**	1.35E+11		
		40	36×15	1.07E+10	1.35E+11		
		200	60×50	1.70E+09	8.15E+10	(-0.9; 0.2)	±1.2
m=3.0	5650	0	14.6×6.6	2.45E+10	2.35E+10		
exit: 0.96 cm^2		**5**	**7×4**	**2.85E+10**	2.35E+10		
F2: 50 mm		7	7×4	2.70E+10	2.35E+10		
		50	40×20	1.10E+09	2.22E+10	large	large

Table 3.12: Elliptical taper: selection from the McSTAS results. The meaning of the columns is explained in Table 3.11 above

from taper exit) was dependent on the given geometry of the chosen taper. The effective beam-size at the target position **H×V** was influenced by the area of the exit window, distance from the taper exit **Z** and by the taper geometry. By the "effective beam-size" is meant the part of the neutron beam area, where the neutron intensity cross-section in both vertical and horizontal direction is still constantly high without fall down on the sides (see e.g. Figure 3.25 for explanation). The total number of neutrons monitored at any particular distance Z from taper exit is marked as **n-total**. In case of Z=0 cm, the neutron flux **n-flux** was obtained by dividing the n-total by the exit area of the taper, for Z>0 cm, the n-flux was obtained from reading the graphical plots.

The vertical and horizontal divergence **div V** and **div H** were monitored by two monitors with different surfaces: from distance Z=0 cm up to Z=30 cm from the taper exit, the monitor had surface of $180 \times 60\,\text{mm}^2$ to see all the neutrons, however, starting Z=50 cm, divergence of neutrons in smaller window of interest was monitored: $54 \times 36\,\text{mm}^2$, what should be enough for cold-neutron tomography of standard PGAA samples. Neutrons outside of this area are also out of our interest. The cold neutron tomography will be performed about 1.5 m – 2.5 m from the taper exit.

3.5.5 Discussion and proposals

When we compare all the results of not tapered end guide, linearly tapered and elliptically tapered guide, we can draw out these statements:

- If **No Taper** was used and the beam guide length was 4400 mm, then it makes no difference, if we use for the supermirror coatings m=2.0, m=2.5 or m=3.0. In all three cases, the neutron flux intensity will be about $2.9 \cdot 10^9\,\text{n/cm}^2\text{s}$ from Z=0 cm up to 100 cm distance from the taper exit with beam dimensions of $110 \times 50\,\text{mm}^2$, see Figure 3.22. In this simplest case, a ^{6}LiF collimator[18] with different central holes would be used to delimit the neutron beam area hitting the target (from $20 \times 20\,\text{mm}^2$ for standard PGAA to $1 \times 1\,\text{mm}^2$ for PS-PGAA and Ge Array). The rest of the beam would be stopped by the collimator while creating minimum background. According to the results, the divergence of the beam is in both directions good, in vertical direction in interval (-0.9°; 0.9°), in horizontal asymmetrically in interval (-0.8°; 0.2°), see Figure 3.23. This asymmetry comes from the very strong horizontal curvature of the bender part of the NL4b and it is intensified by the distribution of the neutrons coming from the Cold Source. Parameters of the not tapered guide give us reference values for comparison with more demanding solutions like linear and elliptical taper.

  The No Taper solution is very simple to make, no tapering part must be added or removed to choose between the standard PGAA and PS-PGAA, so the length

---

[18] The ^{6}LiF polymer collimator will be used in any case between the taper end and the target, to determine exactly the needed beam-size area (smaller than the effective beam-size) and to stop all the other neutrons from the not-used beam part.

of the straight part can stay 4400 mm long for each experimental set-up. The divergence is in both directions very good for tomography, the m parameter can stay m=2.0, and the costs are accordingly minimal possible to finish the PGAA neutron beam guide.

- If **Linear Taper** was used, the difference of neutron flux yielded by m=2.5 or m=3.0 does not differ markedly. For the taper length of 4400 mm, the neutron flux at the distance of Z=15 cm from the taper exit with dimensions of $35.7 \times 16.2\,\mathrm{mm}^2$ would be $1.10 \cdot 10^{10}\,\mathrm{n/cm^2s}$ for m=2.5 or $1.30 \cdot 10^{10}\,\mathrm{n/cm^2s}$ for m=3.0. This means already a gain of 4.5 compared to the No Taper. Further away at Z>15 cm, the intensity of the neutron flux decreases rapidly. The weak point of this solution is the neutron effective beam-size of only about $20\times9\,\mathrm{mm}^2$, as shown in Figure 3.25. This area could be sometimes less than for particular samples needed. The divergence of the neutron flux is also degradated: at Z=100 cm the horizontal divergence is in interval of (-1.3°; 1.3°) and vertical is even within (-1.8°; 1.8°). On the other hand already at the distance of 200 cm with the neutron flux of only $6.2 \cdot 10^8\,\mathrm{n/cm^2s}$, the divergence at the area of interest is only (-0.8°; 0.8°) in horizontal and (-1.2°; 1.2°) in vertical direction, see Figure 3.29. The area of the effective beam-size for tomography samples would be about $60 \times 40\,\mathrm{mm}^2$, what is more than sufficient.

  The Linear Taper solution already needs the removable part of the taper, the m can be chosen m=2.5 without drastic decrease of the neutron flux, the taper is still easy to manufacture with higher costs than the No Taper due to its length and better surface with m=2.5. However, the focal point for the 5650 mm is too close to the taper exit window ($Z \leq 3.5$ cm) and the effective beam-size at 4400 mm is not enough large ($20 \times 9\,\mathrm{mm}^2$), therefore there is no argument strong enough to prefer the Linear Taper solution when compared to the No Taper beam guide straight end.

- In case of the **Elliptical Taper**, the neutron flux at 4400 mm with m=3 would be lower than in case of Linear Taper: $9.20\cdot10^9\,\mathrm{n/cm^2s}$ for m=3.0 at a preferable distance of Z=40 cm from the taper exit. Here the difference between m=2.5 and m=3.0 is more pronounced than in case of the Linear Taper: with m=2.5, the neutron flux at the same position would be only $8.4 \cdot 10^9\,\mathrm{n/cm^2s}$. For the taper length chosen only of 25 cm more to TL=4650 mm, the neutron flux increases to $1.07 \cdot 10^{10}\,\mathrm{n/cm^2s}$ for m=3.0 and for a focus at Z=40 cm. The larger distance Z=40 cm from the taper exit of the best focused neutron-flux is not the only advantage of the elliptical solution. Also the effective beam-size of the Elliptical Taper is favorable compared to the one of the Linear Taper: about $32 \times 15\,\mathrm{mm}^2$, as can be seen in Figure 3.24. The reason is easy: the taper exit dimensions are here much larger than in case of the Linear Taper: $69.9 \times 31.8\,\mathrm{mm}^2$. The divergence of the neutron flux at about Z=200 cm is also good: (-0.9°; 0.2°) in horizontal and (-1.2°; 1.2°) in vertical direction. The divergence in horizontal direction is not symmetrical (see Figure 3.28), better distributed than by the Linear Taper at close distances Z, however at Z=200 cm, the divergence is comparable with the one of the Linear Taper. The neutron flux at Z=200 cm is about three times higher than the Linear Taper gives, only 1.5 times less than by the No Taper solution and ten times more than we had at PSI in 2001. The area of the effective beam-size for Tomography samples would be about $60 \times 50\,\mathrm{mm}^2$, that is more than needed for standard samples.

If we add the last part of the taper and obtain a taper of TL=5650 mm length, the gain of the Elliptical Taper would be $2.85 \cdot 10^{10}\,\mathrm{n/cm^2 s}$ for m=3.0 at the focal point of Z=5 cm or at a technically preferable distance of Z=7 cm without a significant loose of the neutron flux: $2.70 \cdot 10^{10}\,\mathrm{n/cm^2 s}$ for m=3.0. This value is about two times higher than with the Linear Taper at Z=3.5 cm. It is even technically difficult to arrange such a close distance of the target to the taper exit and it is preferred to have a focal point at Z=7 cm with the Elliptical Taper. The gain at the focal point would be also about ten times higher than with the No Taper solution. The effective beam-size area would be $7 \times 4\,\mathrm{mm}^2$ and could be used for small samples like the meteorites of tens of milligram weight, or utilizing the ^{6}LiF collimator with a $1 \times 1\,\mathrm{mm}^2$ opening for the PS-PGAA and Ge Array set-ups.

Except of the worsened vertical divergence for cold-neutron tomography, which is in addition restricted to a minimal distance of Z=200 cm from the taper exit, the Elliptical solution enhance the neutron flux ten times for the PS-PGAA and more than three times for the standard PGAA when compared to the No Taper solution. The elliptical shape, surface of the supermirrors with m=3.0 and the additional removable part of the taper will increase the costs when compared to both previous solutions. On the other hand, the neutron flux could be increased up to 200 times comparing to PSI conditions, so elements like Carbon, Nitrogen, Oxygen, Lead, Bismuth and other elements with low neutron capture cross-section, could be detected with much better sensitivity and thus bring a great advantage of the PGAA method e.g. for biological samples. Further, the measuring time will decrease notably and small amounts of samples ($\leq$100 mg) can be measured. This feature is especially important, when doing experiments on rare isotopes for nuclear physics studies.

Question of detector saturation When discussing the advantages and disadvantages of the proposed end of the NL4b, we were not taking into account another limiting constrain: the saturation of the HPGe detector at about 10 000 cps or the saturation of the acquisition system by large dead time. This means, that an endless gain in neutron flux intensity brings at one moment no benefit if we have no chance, how to improve this constrain. At present, HPGe detectors do not seem to be improved from the point of view of saturation by input count rate. Nevertheless, we feel one should always try to increase the primary beam intensity, since reducing is easier than increasing it.

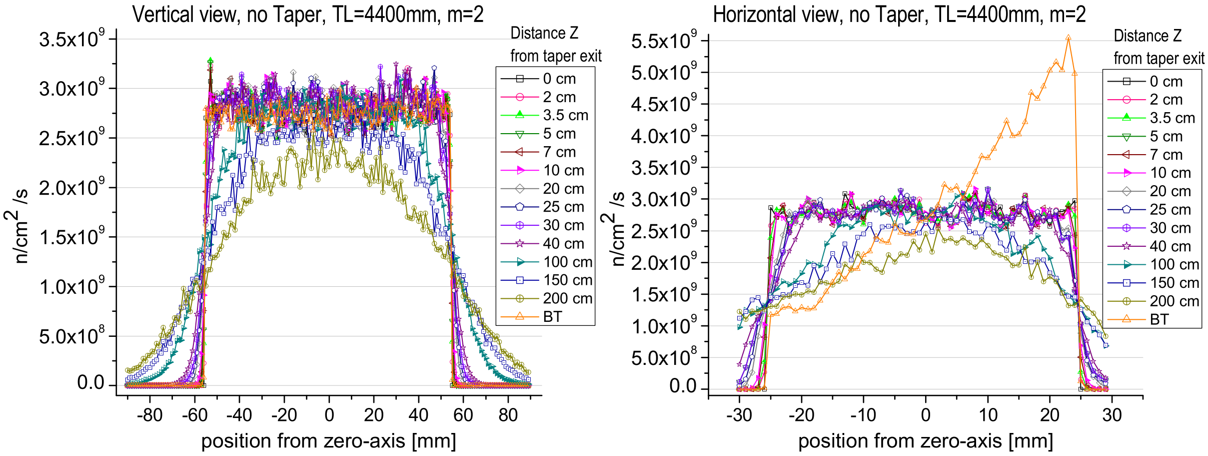

Figure 3.22: No Taper TL=4400 mm, m=2, exit dimensions: 110 × 50 mm^2, vertical and horizontal cut. BT in description box means n-flux before taper.

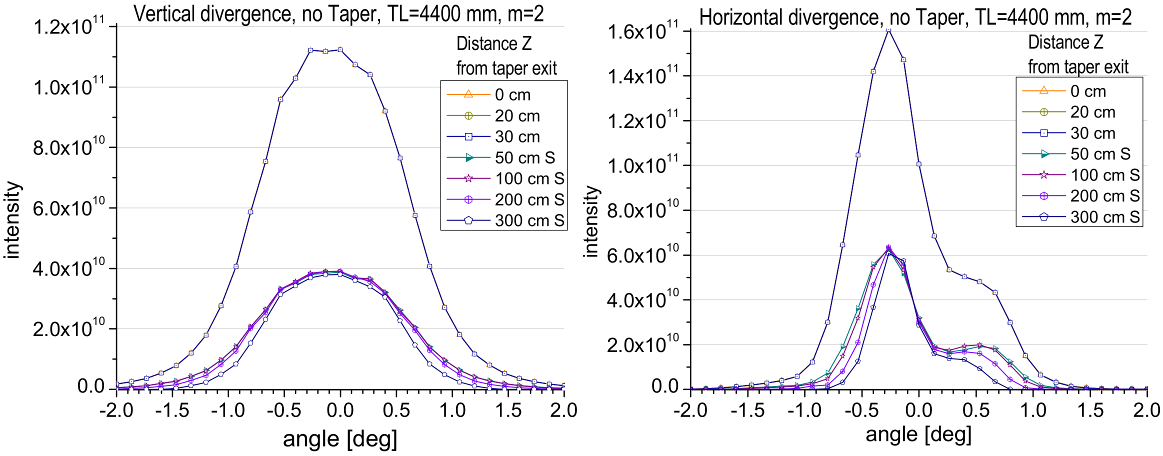

Figure 3.23: No Taper TL=4400 mm, m=2, exit dimensions: 110 × 50 mm^2, vertical and horizontal divergence.

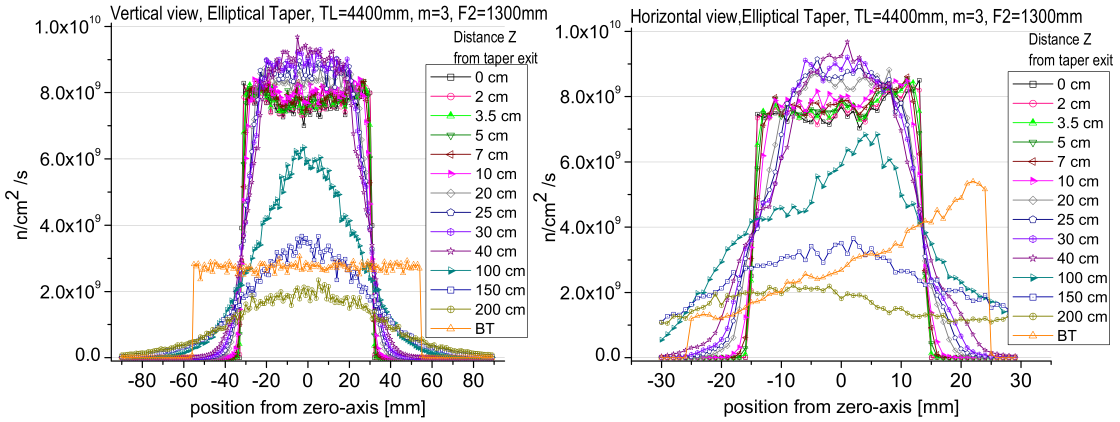

Figure 3.24: Elliptical Taper TL=4400 mm, m=3, F2=1300 mm, exit dimensions: $69.9 \times 31.8\,\mathrm{mm}^2$, vertical and horizontal cut.

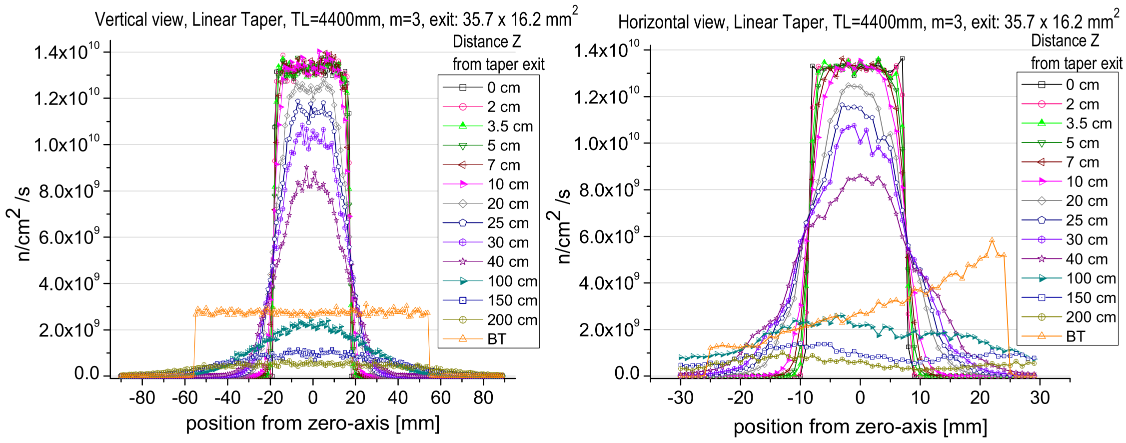

Figure 3.25: Linear Taper TL=4400 mm, m=3, exit dimensions: $35.7 \times 16.2\,\mathrm{mm}^2$, vertical and horizontal cut.

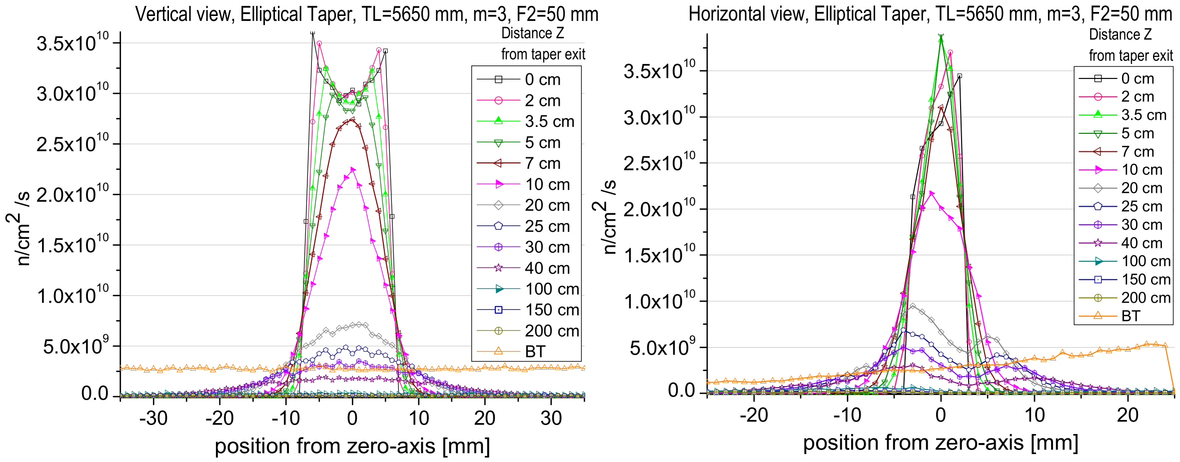

Figure 3.26: Elliptical Taper TL=5650 mm, m=3, F2=50 mm, exit dimensions: $14.6 \times 6.6\,\mathrm{mm}^2$, vertical and horizontal cut.

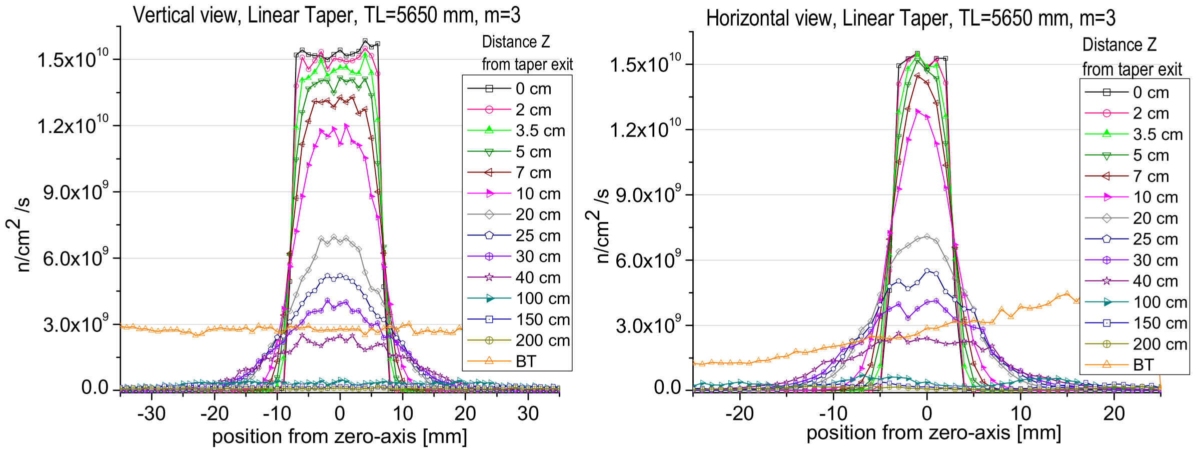

Figure 3.27: Linear Taper TL=5650 mm, m=3, exit dimensions: $14.6 \times 6.6\,\mathrm{mm}^2$, vertical and horizontal cut.

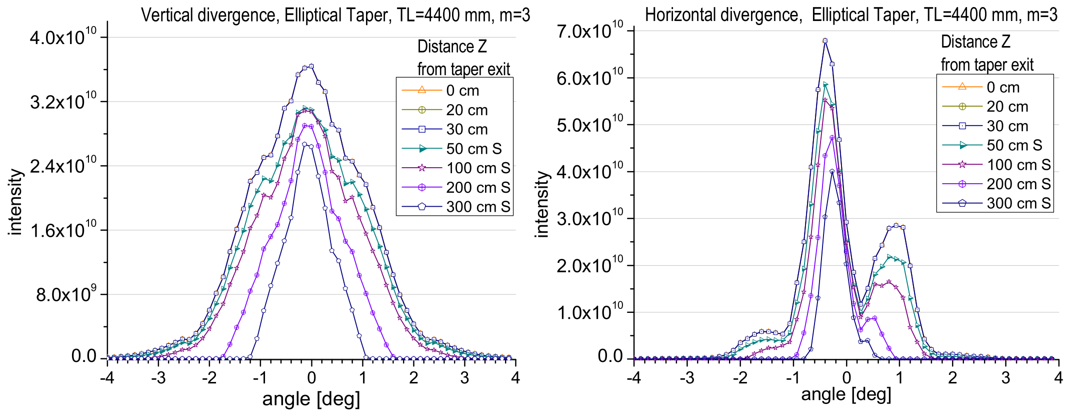

Figure 3.28: Elliptical Taper TL=4400 mm, m=3, exit dimensions: $69.9 \times 31.8\,\text{mm}^2$, vertical and horizontal divergence.

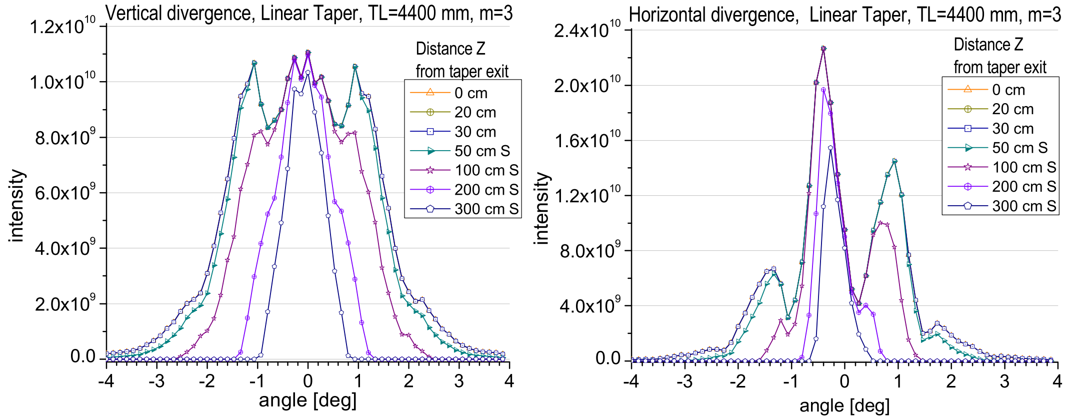

Figure 3.29: Linear Taper TL=4400 mm, m=3, exit dimensions: $35.7 \times 16.2\,\text{mm}^2$, vertical and horizontal divergence.

Question of increased background Another question in comparison between No Taper and Taper is the height of the created background. It is not easy to decide, if the background is substantially higher, when the Taper is used instead of No Taper, in which case the neutrons of the not-used beam area are absorbed directly in a ^{6}LiF collimator and thus creating minimum γ-ray background. We can expect, that more neutrons are absorbed in the tapered neutron guide, e.g. in the thin Ni–Ti supermirror layers, which can produce high-energy γ-rays: ^{48}Ti captures thermal neutrons with $\sigma_0 = 5.2$ barn while emitting γ-ray with $E_\gamma = 1382$ keV; but ^{48}Ti also emits high energy γ-rays: $E_\gamma = 6760$ keV with $\sigma_0 = 3.0$ barn and $E_\gamma = 6418$ keV with $\sigma_0 = 2.0$ barn. Nickel ^{58}Ni produces also many high-energetic γ-lines after neutron capture: e.g. $E_\gamma = 8993$ keV with $\sigma_0 = 1.5$ barn and $E_\gamma = 8533$ keV with $\sigma_0 = 0.72$ barn. Such energetic γ-rays can easily penetrate to the measuring chamber, but not through a very thick lead shielding around the Compton-suppressed detector. The Ni–Ti layers are also very thin (about 0.9 μm) so the intensity of created γ-rays might be reasonably low. The not reflected and not absorbed neutrons in the inner parts of the tapered beam guide could be stopped by plates of ^{6}LiF polymer distributed along the taper the way to shield the direction of the measuring chamber and detectors.

For the last removable part of the Taper some feasible solution of shielding the neutrons and γ-rays should be found not to make it too heavy and large on one side and to reduce the created background to possible minimum.

3.6 PGAA Conclusions

PGAA is a nuclear analytical technique convenient for a major and trace multi-elemental analysis with limits of detection between 0.001 μg/g (B, Gd, Cd) up to units of percent (C, N, O). It gives an average composition of the irradiated sample volume and the PGAA technique can be therefore used among others to complement a surface analysis of PIXE by a bulk sample analysis. Comparison of the PGAA and PIXE results can offer this way valuable additional information about the sample. The great advantage of PGAA is that it is non-destructive method – there are even no problems with heating and charging the sample compared with charged-particle methods. Another quality of PGAA is that solid, liquid and gas samples (in Teflon vials) can be measured without any special preparation (unlike in case of surface methods, where the quality of the surface is usually essential for the analysis). PGAA can be also helpful for PIXE samples with high content of e.g. Ca and Fe, where some L-lines of trace elements overlap with the matrix elements and PIXE analysis is then less reliable. On the other hand, if the sample is homogeneous with a suitable surface, PIXE measurement can be performed with much smaller sample mass and gives much more sensitive and accurate analysis for majority of trace elements with Z $\geq$14 (exception can be Cd, Sm, Gd, when PGAA is very sensitive, too). It was already discussed that PGAA is a complementary resp. competitive method with regard to INAA for elements like H, B, C, N, Pb, Bi resp. Cd, Gd. Interest in these mentioned elements is the case, when PGAA should be used instead of INAA (assuming no need of an ultra-trace analysis). PGAA can be also considered in cases, when long term activation by INAA does not allow direct or quick sample manipulation. The summary of PGAA applicability can be found e.g. in Molnár et al. (2004) and Alfassi (2001). Taking advantage of the experience gained at PSI and Budapest, we are designing and building a new PGAA facility at the FRM-II research reactor in Garching by Munich. With this facility and a minimal cold neutron flux of $3 \cdot 10^9\,\mathrm{n/cm^2s}$ we expect to improve five times the limits of detection compared with those at PSI and to obtain the best detection limit worldwide for non-destructive measurement of boron. The challenging task will be to keep the background during the measurement at the lowest possible limit to achieve our objective – competitive limits of detection and quantification.

Chapter
4

Conclusions

The objective of this thesis was:

1. To co-operate on design, construction, control, calibration, data acquisition and analysis of the new PIXE instrument at the 10 MV Pelletron Accelerator of the IKP, University of Cologne. Therefore many different experimental configurations were tested and very different samples were measured. The samples were chosen from diverse fields on purpose to understand particular behavior of the measurement and possible biases by the analysis of samples from geology, archaeology, material industry or for thin environmental samples. Experiments with the PIXE instrument allows now a reliable analysis for major components and for many trace elements, although, for some of them, the accuracy of the analysis is still not satisfactory. Solutions solving the problems are proposed here. The PIXE instrument is reliable for analysis not only of thin targets, but also of thick samples with flat surface and for macro-scanning of samples, which results in a 2D map of the element distribution on their surface.

2. The second part of my dissertation was dedicated to the PGAA experiments performed at PSI and BNC, and to the design of a new PGAA instrument, which will be installed at the FRM-II at the beginning of 2006. Since PGAA is an unique technique for the determination of boron in the sample bulk, a special approach to the determination of a boron content in solid and liquid samples was explained and the limit of detection for the boron in liquids was determined for the PGAA facility at PSI. The advantages of the relative approach of the k_0 method for the PGAA analysis were discussed. The reliability of the PGAA method for small amounts of meteorite specimens was manifested by the PGAA measurement at the Budapest PGAA facility. The samples were either heterogeneous stones or homogeneous powders, with a mass between $(100 - 300\,\mathrm{mg})$. The results were compared to the literature values, which were results of analysis by various techniques, like ICP-MS, NAA, XRF or chemical analysis.

   The design, plans and simulations for the best possible set-up of the PGAA instrument in the NL-hall of the FRM-II are under development at the period of writing this thesis. Care must be taken not only to get the best parameters for the PGAA instrument, but at the same time, well acceptable conditions for cold-neutron tomography as well as for nuclear experiments with a Ge Array and with a well focused neutron beam must be taken into account. Last but not least, position sensitive PS-PGAA or PGAI-imaging with a neutron beam focused to $1\,\mathrm{mm}^2$ is a challenging task to be incorporated. Some solutions for operating all the instruments at the end of the PGAA neutron beam guide are proposed and verified by extensive simulations with the McSTAS program.

4.1 PIXE Installation at IKP

The PIXE set-up at the IKP is successfully operating and can be used for an analysis of thin targets, thick targets as well as for macro-scanning of larger objects with a proton beam focused below $1 \times 1\,\mathrm{mm}^2$. The task of normalization of the proton beam was solved by sweeping the proton beam on a collimator with a central opening of $3\,\mathrm{mm}^2$ in diameter. Within one run, up to 24 small samples fixed on a rotating wheel can be measured. For the detection of X-rays, mainly a small Peltier-cooled XFlash detector is used and brings the advantage of its capability to acquire up to 300 kcps. Its shaping time of $0.5 - 1.0\,\mu$s is in comparison with the common Si(Li) detector $(10 - 24\,\mu\mathrm{s})$ of a great advantage for an acquisition by high count rates. The data acquisition is performed by digital electronics with a system based on DGF-4C modules from X-ray Instrumentation Associates (XIA) and with an in-house developed acquisition software. For the analysis of the PIXE spectra, the GUPIX program is used. The calibration of our PIXE installation was done with thin MicroMatter standards and some effort was dedicated to find the best set of H values describing well the PIXE set-up. The dependence of the H values on distance was studied and the stability of the H values curve was confirmed. Then, homogeneous powders of Standard Reference Materials (SRM) were measured to check the reliability of the sample analysis. Next, thick samples were analysed. From the analysis it turned out, that care must be taken by the quality of the sample surface to obtain true elemental concentrations. The macro-scanning with the PIXE instrument is also very reliable, as the example of the Green Glass confirmed. The elemental distributions of Cu and Cr correspond to the dark-green colour distribution in the sample.

The PIXE part of the thesis was written in great detail with the aim to make the PIXE set-up familiar for successors to overcome easier the first, introductory phase with the installation, data acquisition and data analysis.

4.2 PGAA Experiments at BNC

The PGAA results of GSP-1, G-2 geological standards as well as of Orgueil meteorite (all of them homogeneous powders) have proved the reliability of the PGAA analysis for small amounts of samples (less than 300 mg). Since in all three cases the amount of Sm was in disagreement with the nominal values, we expect the k_0 value of Sm not to be correct due to the resonances in the epithermal neutron region. We have compared 3 pieces of Allende meteorite, two of them originating from one part, the third one from a different part of the meteorite. The Allende is very inhomogeneous with visible grains. The comparison of all three results have shown, that the Allende 1 and 2 have very similar composition, while Allende 3 has different composition for H, Na, S, Cl, K, Co and Ni. The variability of concentration of the mentioned elements in Allende is possible with exception of Co and Ni (Palme, 2005). Therefore, more measurements should be performed to reanalyse the amount of Co and Ni. This is planned for the PGAA facility at FRM-II. In case of Dhurmsala homogeneous powder compared to heterogeneous grainy stone piece we could see, that concentration of most of the elements in both cases was the same. However, disagreement was found in case of S, Cl, Co and Ni as well as Sm and Gd and the granularity could be the reason for this result. In case of Morávka meteorite, the reliability of the PGAA analysis for only 125 mg of a sample amount was demonstrated. For the comparison of elemental concentrations, results of competitive methods based on activation analysis (INAA, IFNAA, RNAA, IPAA) for a sample analysis were employed. Finally, volcanic material of distinct structure of the same origin was analysed for determination of boron concentration. It was also of high interest to compare both analysing programs Hypermet-PC of Budapest PGAA group and PEGASE used at PSI. The advantage of PEGASE is the fact, that after the calibration, the analysis can be fully automatic, while the analysis with Hypermet-PC requests more time spent with each spectrum analysis. Depending on the results of such an experiment, PEGASE could be used for a really fast analysis of major and minor components and Hypermet-PC could be applied for a more detailed trace analysis, where the information about all possible detected peaks for particular isotope are of importance, or, if the main peaks are convoluted with some other γ-ray energies of other elements, the interactive analysis is preferred. The general agreement between both analysing programs for most of the elements within 10 % was demonstrated on the Allende 1 sample in section 3.4.2. The large difference between the Sm concentration determined in most of the analysed samples in comparison with literature values was discussed with a conclusion that the k_0 value of PSI is better evaluating the Sm concentration than the Budapest k_0 value, which underestimates the Sm concentration. To make similar conclusion for e.g. Ca, which also tends to be underestimated by the Hypermet-PC analysis, or for Na, K, Mn and Ni, which did not show good agreement with the PEGASE analysis, we would need to compare more data.

4.3 PGAA Instrument at FRM-II

A new PGAA station will be installed and operated at the FRM-II reactor in Garching at the beginning of 2006. The PGAA station has been moved from the Paul Scherrer Institute (PSI), Villigen, Switzerland where it was in operation during the years 1997 – 2002. The facility is now being re-designed for four different experimental applications at FRM-II: standard PGAA instrument, position-sensitive PGAA set-up, cold neutron tomography set-up, a new compact Ge Array, all with respect to the new neutron beam guide dimensions, parameters and characteristics. We expect to have at least 20 times higher cold neutron flux at FRM-II (without any tapering) and thus about

5 times better limits of detection than we had with this PGAA instrument at PSI. Our endeavour is to design for the PGAA at FRM-II the most convenient method to focus the neutrons to a spot of about $1\,\mathrm{mm}^2$ and to develop a position sensitive PGAA. According to the McSTAS simulations and compared to PSI, we could obtain more than 70 times higher neutron flux at the target position of the standard PGAA at the distance of 40 cm far from the 4650 mm long part of the elliptical taper proposed in section 3.5.4. With the 1 m removable extension of the elliptical taper to the length of 5650 mm, we could have even 200 times higher neutron flux with a surface of $7 \times 4\,\mathrm{mm}^2$, which would be collimated to the requested $1 \times 1\,\mathrm{mm}^2$ for PS-PGAA. We could then expect to improve the limits of detection more than 10 times!

We will use the same Compton suppressed spectrometer with a central detector, a coaxial HPGe crystal of $168\,\mathrm{cm}^3$ volume, which is surrounded by a NaI(Tl)/BGO scintillator and is irradiated from the side. Such a set-up allows the Compton shielding to be places in forward direction, which decreases considerably the number of background gamma-rays. Only with very low background we can reach satisfactory sensitivity and the encouraging limits of detection discussed above. The saturation of the HPGe detector by 10 000 cps denotes the present upper limit of utilisable neutron flux intensity by the set up.

We have gained a great experience at PSI and later at BNC and we will use it for the development of the scientific program at the PGAA facility at FRM-II. This will involve many fields of applications including physics, chemistry, medicine, geology, environmental science, engineering, and archeology. As a new sphere of activity, a project in cosmochemistry has been opened. It will be possible to make a systematic analysis of very small amounts and pieces of meteorites (≤ 100 mg) for H, B, S, Ti and other interesting elements (from the point of view of cosmochemists) using the high neutron flux at FRM-II. The PGAA method could also be preferred over destructive methods of analysis when a composition of radioactive waste should be qualified and quantified not only for active elements but also for other compounds.

Currently, about twenty PGAA installations exist world-wide, but only few of those have intense cold neutron beams available. If comparing PGAA with the chemical methods, ICP-MS or ICP-OES can reach definitely much lower limits of detection in many cases. However, PGAA has an advantage as a non-destructive analytical tool and as a method without need of elaborate and lengthy preparation of the samples before their analysis. Further, the results of the PGAA analysis are available within one day, in particular cases, e.g. for Boron Neutron Capture Therapy – BNCT, the concentration of boron in blood of the patient can be determined within 15 minutes only (IAEA, 2001).

4.4 Comparison of the PGAA and PIXE methods

The comparison of PGAA and PIXE is discussed to some content already in section 3.2.6 on page 84 and in section 3.6 on page 128. The comparative and complementary results of the PIXE analysis from section 2.4.3 and the PGAA analysis measured at PSI in 2001 (Baechler et al., 2003) are demonstrated in Table 4.1 on the example of SRM 1633b. The PIXE results in Table 4.1 were obtained from a measurement of a thin target and they were recalculated from $[\mu g/cm^2]$ to the SRM nominal values in $[\mu g/g]$ with the use of the K concentration, which is therefore given without any standard deviation. Thus, with the help of the NIST SRM 1633b Coal Fly Ash, we can compare both techniques. PIXE is much more sensitive method already for very small amounts of many elements, like e.g. Ni, Cu or Zn; on the other hand our PIXE instrument is not reliable for elements like Al, Si, S or P because of the protecting foil, which stops more than 90 % of X-rays with energy lower than 2.5 keV. PGAA can be used for low Z elements and for elements with high neutron capture cross-section like Cd, Sm or Gd. For other elements, whose concentration was for the PGAA measurement not far below the limit of detection or quantification, we would either have to measure for longer time or to use the higher flux available at the FRM-II to obtain their concentrations.

If the composition of a sample bulk and not only of its surface needs to be analyzed non-destructively, (i.e. when surface methods like the PIXE analysis and other methods using charged particles beams and reaching sometimes better limits of detection cannot be used), PGAA is among the best possible multi-elemental analytical methods (together with NAA) for an analysis up to trace amounts (up to ng/g) (Kudějová et al., 2005a).

A good example of a case when PGAA was the best non-destructive method to choose can be given: Fifty-four selected pieces of brooches from Western Switzerland, representative with respect to chronology and typology, were analyzed by the PGAA method for the major components Cu, Zn, Sn and Pb (Baechler et al., 2003; Kudějová et al., 2004). INAA cannot be used in this case because it does not detect Pb at all. PGAA is also less sensitive to Pb, but the amount of Pb in the brooches was much higher (units of percent) than the limit of detection (331 μg/g). One brooch contained a much higher concentration of Pb than the others coming from the same period; the Pb was very likely contained mainly in the decoration on the surface. For this purpose, PIXE as a surface analytical technique is the adequate method to determine, if the concentration of Pb in the surface layer was indeed higher than the average concentration of Pb in the sample bulk determined by PGAA.

Both PIXE and PGAA methods are reliable and give good results up to the trace amounts of elements, however, they are not suitable for an ultra-trace analysis of thick samples. Their great advantage is the relatively short timespan between the sample irradiation and having the results of the data analysis. Both methods are able to give an answer for the composition of an unknown sample within one day. In case of PIXE, the sample can be given back to the owner at the same day together with the results, since PIXE causes no activation. In case of PGAA, the sample can be given

Z	Element	PIXE[1] $[\mu g/g]$			PGAA[2] $[\mu g/g]$			SRM 1633b[3] $[\mu g/g]$		
1	H	-			1240	±	1000	-		
5	B	-			76.7	±	2.3	-		
13	Al	-			146800	±	2600	150500	±	3010
14	Si	232300	±	17800	237200	±	4400	230200	±	0
16	S	1900	±	150	1990	±	280	2075	±	21
19	K	19500			19500			19500	±	390
20	Ca	15110	±	760	14550	±	140	15100	±	600
22	Ti	9190	±	460	8150	±	60	7910	±	160
23	V	500	±	40	-			295.7	±	3.0
24	Cr	257	±	17	-			198.2	±	4.0
25	Mn	131	±	14	280	±	110	131.8	±	1.3
26	Fe	75990	±	3810	74700	±	2300	77800	±	2300
28	Ni	135	±	9	-			120.6	±	1.2
29	Cu	132	±	11	-			112.8	±	2.3
30	Zn	260	±	16	-			210		
33	As	122	±	16	-			136.2	±	2.7
34	Se	16	±	10	-			10.26	±	0.21
37	Rb	268	±	35	-			140		
38	Sr	1440	±	90	-			1041	±	10
48	Cd	-			0.82	±	0.32	0.784	±	0.008
56	Ba	1110	±	340	-			709	±	28
58	Ce	213	±	89	-			190		
60	Nd	102	±	32	-			85		
62	Sm	36	±	31	14.93	±	0.27	20		
64	Gd	-			18.1	±	2.0	13		

Table 4.1: SRM 1633b Coal Fly Ash measured both with PIXE at IKP, Cologne and PGAA at PSI, Switzerland.

[1] The PIXE and PGAA results were normalized to the SRM nominal value for K concentration, therefore those values are for both given without standard deviation.The PIXE results for thin target are calculated in $[\mu g \cdot cm^{-2}]$, while the SRM nominal values are in $[\mu g/g]$ and for comparison recalculation is needed

[2] The amount of the elements not detected by PGAA are below limit of detection or quantification (for 0.5 g sample, irradiated for 6 hours by cold neutron flux of $1.4 \cdot 10^8$ n/cm^{2}s, (Baechler et al., 2003)).

[3] The SRM nominal values with given standard deviation are certified values, while those without any error are non-certified values

back usually within few days.

When we compare PGAA with the Instrumental Neutron Activation Analysis (INAA), PGAA is an eligible complementary method to INAA for detection of light elements like H, Li, Be, B, C, N, O, F or P and competitive technique for e.g. S, Cd, Gd, Tl, Pb and Bi.

4.5 Outlook

PIXE

What should we concentrate on now in case of the PIXE instrument? It is important to open some long term cooperation with institutes and institutions, which could bring some interesting research cooperation. For example, there are possibilities in geology, archaeology, environmental and material research or food industry. In the last case, the concentration of not-allowed heavy elements in food and water is of high interest and automated multi-elemental method can save time considerably when compared to a chemical analysis. Pre-concentration of the samples by ashing would enhance the sensitivity and limits of detection. For the archaeological research, combination of PIXE and PGAA could be of high interest.

To enhance the PIXE instrument at IKP, following improvements and modifications could be accomplished:

- We could try once again to get a better description of the XFlash detector parameters needed for the GUPIX analysis. On the other hand, the XFlash detector has a different construction from a common Si(Li) detector and therefore it is very likely not possible to obtain an ideal description of the PIXE instrument which would be characterized only by one H value instead of set of H values dependent on the X-ray energy.

- If we want to get better accuracy for the trace analysis of elements whose peaks occur close to strong peaks of matrix elements, a better description of peak-tailing effects should be used for the description of the XFlash detector. To do this, spectra of pure elements are fitted by Voigt functions together with appropriate exponentials, which describe the left-tailing and other effects. The required derived parameters can be then used for the GUPIX fitting procedure.

- The description of the Makrofol protecting foil for the X-ray transmission calculations is not yet implemented in GUPIX (in a form of molecules), the effect is replaced by the transmission of individual layers of involved elements H, C and O.

- If we do not succeed with the implementation of Makrofol into GUPIX, we could think to exchange the foil with some other, which is already described for GUPIX. This would also allow us to use such a foil, which stops protons totally but its transmission for low Z elements (Al, Si, P and S) would be better than of Makrofol, e.g. proposed Marlex.

- It would be also interesting to use a so-called funny filter[1] for samples which contain major elements like S, Cl, K, Ca or Fe to increase the sensitivity for trace elements.
- We should try another way of proton current normalization: a very thin carbon foil of known thickness placed about 1 – 2 cm in front of the thick sample. Protons back-scattered from the foil would be detected by a surface barrier detector and used for normalization purposes. This set-up brings along the advantage of compensation of the proton charge deposited to the sample surface for insulating or poorly conducting samples by striping sufficient electrons from the carbon foil. These electrons follow the protons to the sample surface and helps to compensate the charge deposited by the protons.
- Not only normalization of the proton current and protection against burning the sample is solved by the carbon foil in front of the sample. Sudden discharging of the insulated samples causes increased continuous background in the PIXE spectrum and thus lowers the sensitivity of the analysis. Continuous discharging of the not-conducting samples can be solved either with the carbon foil as discussed before or also with the help of an e-gun = hot-wire element.
- We have to avoid materials like Teflon in the PIXE chamber, or cover it by a carbon foil. This is once again a way, how to reduce the background of the PIXE spectrum.

PGAA

In case of our plans and intentions for the PGAA instrumentation at the FRM-II our way is very clearly directed: we have to first finish the design and then the PGAA station itself, including all other experimental set-ups which will be run at the beginning with the standard PGAA instrument from PSI. The experiments in Budapest have validated, that even very small amounts of geological samples – ca. 100 mg, can be reliably measured and analysed at least for major and minor elements. For trace elements, the limits of detection resp. quantification were sometimes higher than the amount of particular trace elements in the sample and therefore they could not be detected resp. they were detected but could not be quantified. This will not be the case of the PGAA at FRM-II, since we intend to measure such small amounts of samples ≤ 100 mg with a focused neutron beam that brings along neutron flux higher by orders of magnitudes than we had in Budapest. Thus, we expect also much

---

[1] Funny filter is a protecting foil, which is thick and allows only X-rays of higher energy to reach the detector. In its middle, a small opening with a much thinner foil is used, which still stops the protons, but lets pass some small and well defined percentage of X-rays of low-Z elements like Cl, K, Ca, ...

better limits of detection as well as much shorter times of measurement. Anyway, we must not underestimate the background level in the acquired spectrum, which can be increased in the case of a focused neutron beam considerably and therewith the limits of detection could be worse than expected.

Accuracy of the measurement For both PGAA and PIXE analysis, we want to pay more attention to the achievable accuracy and precision of the results and dedicate more effort to the error analysis. We want to systematically recognize all sources of errors and evaluate them, find possible systematic errors and uncertainty of the measurement. So, we want to enhance the accuracy of the measurement and evaluate the results with better knowledge about its precision. How important is the unavoidable error evaluation, is discussed e.g. by Lindstrom and Greenberg (2001).

References

Acharya, R. N., Sudarshan, K., Nair, A. G. C., Scindia, Y. M., Goswami, A., Reddy, A. V. R., and Manohar, S. B. (2001). The use of element ratios to eliminate analytical bias in cold neutron prompt gamma-ray activation analysis. *Journal of Radioanalytical and Nuclear Chemistry*, 250(2):303–307.

Alfassi, Z. B., editor (2001). *Non-destructive Elemental Analysis.* Blackwell Science (UK), London, United Kingdom.

Baechler, S., Jolie, J., Beer, H.-F., Rüthi, M., Bajo, S., Egloff, M., Patorski, M., Aebersold, H.-U., Lehmann, E., and Zimmermann, H.-P. (2001). Prompt gamma-ray activation analysis of ashes from the PSI-incinerator, Labor für Radio- und Umweltchemie der Universität Bern und des Paul Scherrer Instituts. *Annual Report des Paul Scherrer Instituts*, 1:33.

Baechler, S., Kudejova, P., Jolie, J., and Schenker, J.-L. (2003). The k_0-method in cold-neutron prompt gamma-ray activation analysis. *Journal of Radioanalytical and Nuclear Chemistry*, 256(2):239–245.

Baechler, S., Kudejova, P., Jolie, J., Schenker, J.-L., and Stritt, N. (2002a). Prompt gamma-ray activation analysis for determination of boron in aqueous solutions. *Nuclear Instruments and Methods in Physics Research A*, 488:410–418.

Baechler, S., Masschaele, B., Cauwels, P., Dierick, M., Jolie, J., Materna, T., and Mondelaers, W. (2002b). The new cold neutron tomography set-up at SINQ. *Nuclear Instruments and Methods in Physics Research A*, 481:397–405.

Belgya, T., Révay, Z., Ember, P. P., Weil, J., and Molnár, G. L. (2003). The cold neutron PGAA-NIPS facility at the Budapest Research Reactor. In *Proceedings of the Eleventh International Symposium Capture Gamma-ray Spectroscopy and Related Topics, Pruhonice near Prague, Czech Republic, September 2-6, 2002*, pages 562–568.

Belgya, T., Révay, Z., Fazekas, B., Héjja, I., Dabolczi, L., Molnár, G. L., Kis, Z., Östör, J., and Kaszásand, G. (1997). The New Budapest Capture Gamma-Ray Facility. In *Proceedings of the Ninth International Symposium Capture Gamma-ray Spectroscopy and Related Topics*, page 826.

Berger, M. J., Hubbell, J. H., Seltzer, S. M., Coursey, J. S., and Zucker, D. S. (2004). XCOM: Photon Cross Sections Database. http://physics.nist.gov/PhysRefData/Xcom/Text/XCOM.html.

Blaauw, M. and Mackey, E. A. (1997). Neutron self-shielding in hydrogenous samples. *Journal of Radioanalytical and Nuclear Chemistry*, 216(1):65–68.

Böni, P. (2000). Novel concepts in neutron instrumentation. *Physica B*, 276–278:6–11.

Borovička, J., Weber, H. W., Jopek, T., Jakeš, P., Randa, Z., Brown, P. G., Revelle, D. O., Kalenda, P., Schultz, L., Kučera, J., Haloda, J., Týcová, P., Frýda, J., and Brandstätter, F. (2003). The Morávka meteorite fall: 3. Meteoroid initial size, history, structure, and composition. *Meteoritics and Planetary Science*, 38(7):1005–1021.

Byrne, J. (1995). *Neutrons, Nuclei and Matter: An Exploration of the Physics of Slow Neutrons.* IOP Publishing Ltd, Bristol, United Kingdom.

Campbell, J. L. (1996). Si(Li) detector response and PIXE spectrum fitting. *Nuclear Instruments and Methods in Physics Research B*, 109/110:71–78.

Campbell, J. L., Higuchi, D., Maxwell, J. A., and Teesdale, W. J. (1993). Quantitative PIXE microanalysis of thick specimens. *Nuclear Instruments and Methods in Physics Research B*, 77:95–109.

Campbell, J. L., Maxwell, J. A., and Teesdale, W. J. (2004). GUELPH PIXE SOFTWARE PACKAGE. http://www.physics.uoguelph.ca/PIXE/gupix/.

Campbell, J. L. and McGhee, P. L. (1986). State-of-the-art efficiency determination for a Si(Li) X-ray detector in the 3-40 keV energy range. *Nuclear Instruments and Methods in Physics Research A*, 248:393–404.

Campbell, J. L. and McNelles, L. A. (1975). An inter-comparison of efficiency-calibration techniques for semiconductor X-ray detectors. *Nuclear Instruments and Methods in Physics Research*, 125:205–223.

Copley, J. R. D. (1991). Scattering effects within an absorbing sphere immersed in a field of neutrons. *Nuclear Instruments and Methods in Physics Research A*, 307:389–397.

Copley, J. R. D. and Stone, C. A. (1989). Neutron scattering and its effect on reaction rates in neutron absorption experiments. *Nuclear Instruments and Methods in Physics Research A*, 281:593–604.

Crittin, M., Kern, J., and Schenker, J.-L. (2000a). First results from the new prompt gamma-ray activation facility at PSI. *Journal of Radioanalytical and Nuclear Chemistry*, 244(2):399–404.

Crittin, M., Kern, J., and Schenker, J.-L. (2000b). The new prompt gamma-ray activation facility at the Paul Scherrer Institute, Switzerland. *Nuclear Instruments and Methods in Physics Research A*, 449:221–236.

CRYTUR (2005). CRYTUR, Ltd: Scintillation materials and detectors. http://www.crytur.cz/.

Englert, P., Herpers, U., Sarafin, R., Padia, J. T., and Rao, M. N. (1986). Cosmic-ray records in the LL-chondrite Dhurmsala. *Geochimica et Cosmochimica Acta*, 50:1593–1598.

Fleming, R. F. (1982). Neutron Self-shielding Factors for Simple Geometries. *International Journal of Applied Radiation and Isotopes*, 33(11):1263–1268.

FRM-II (2005). Forschungsneutronenquelle Heinz Maier-Leibnitz (FRM-II). http://www.frm2.tum.de/index_en.shtml.

Genilloud, L. (2000). PEGASE. Program evaluating gamma-ray spectra for the determination of elemental compositions. Internal Report IFP-PAN, University of Fribourg, Switzerland.

Gladney, E. S., Jones, E. A., Nickell, E. J., and Roelandts, I. (1992). Compilation of Elemental Concentration Data for USGS AGV-1, GSP-1 and G-2. *Geostandards Newsletter*, 16:111–300.

Grimm, J. (2000). Studien zur Bestimmung von Bor und Analyse der Isotopenverhältnisse in geochemischen Proben. Diplomarbeit Universität Bern.

Harling, O. (2005). The Basics of Boron Neutron Capture Therapy. http://web.mit.edu/nrl/www/bnct/info/description/description.html.

Hils, T., Böni, P., and Stahn, J. (2004). Focusing parabolic guide for very small samples. *Physica B*, 350:166–168.

IAEA (2001). Iaea-tecdoc-1223: Current status of neutron capture therapy. Technical report, International Atomic Energy Agency, Vienna.

Ishii, K. and Morita, S. (1984). Continuum x rays produced by light-ion-atom collisions. *Physical Review A*, 30(5):2278–2286.

Ishii, K. and Morita, S. (1987). Scaling law for a continuum of X-rays produced by light-ion-atom collisions. *Nuclear Instruments and Methods in Physics Research B*, 22(1-3):68–71.

Jarosewich, E. (1990). Chemical analysis of meteorites: A compilation of stony and iron meteorite analysis. *Meteoritics*, 25:323–337.

Johansson, S. A. E. and Campbell, J. L. (1988). *PIXE: A Novel Technique for Elemental Analysis.* John Wiley & Sons, Chichester, UK.

Johansson, S. A. E., Campbell, J. L., and Malmqvist, K. G., editors (1970a). *Particle-Induced X-Ray Emission Spectrometry (PIXE).* John Wiley & Sons, Inc., Chichester, UK.

Johansson, T. B., Akselsson, K. R., and Johansson, S. A. E. (1970b). X-ray analysis: elemental trace analysis at the 10-12g level. *Nuclear Instruments and Methods in Physics Research*, 84:141.

Jolie, J., Börner, H. G., Hoyler, F., Robinson, S., and Dewey, M. S. (1988). Extraction of lifetimes from Doppler broadened lineshapes of nuclear transitions. In *Proceedings of the Sixth International Symposium on Capture Gamma-ray Spectroscopy, Leuven, Belgium, 1987*, pages 586–589.

Jolie, J., Schieck, H. P. G., Eberth, J., and Dewald, A. (2002). The Institute for Nuclear Physics of the University of Cologne: laboratory portrait. *Nuclear Physics News*, 12(1):4–12.

Kallemeyn, G. W. and Wasson, J. T. (1981). The compositional classification of chondrites – i. the carbonaceous chondrite groups. *Geochimica et Cosmochimica Acta*, 45:1217–1230.

Král, J. (2004). Calibration of the pixe set-up with the use of h values and application of the pixe analysis for biological samples. Private communication.

Kubo, M. K. and Sakai, Y. (2000). A Simple Derivation of the Formula of the Doppler Broadened 478 keV γ-Ray Lineshape from ^{7*}Li and Its Analytical Application. *Journal of Radioanalytical and Nuclear Chemistry*, 1(2):83–85.

Kudějová, P., Baechler, S., Materna, T., and Jolie, J. (2004). Prompt Gamma-Ray Activation Analysis and Neutron Tomography with cold neutrons - latest results from PSI and future projects for the FRM-II in Munich. In Plompen, A. J. M., editor, *Proceedings of the enlargement workshop on Neutron Measurements and Evaluations for Applications NEMEA, 5-8 November 2003, Budapest, Hungary*, pages 1–5.

Kudějová, P., Materna, T., Jolie, J., and Pascovici, G. (2005a). The new PGAA facility at the FRM II, Garching: comparison with the PIXE results obtained at the new IBA setup at Cologne. *X-Ray Spectrometry*, 34(4):350–354.

Kudějová, P., Materna, T., Jolie, J., Türler, A., Wilk, P., Baechler, S., Kasztovszky, Z., Révay, Z., and Belgya, T. (2005b). On the construction of a new instrument for cold-neutron prompt gamma-ray activation analysis at the FRM II. *Journal of Radioanalytical and Nuclear Chemistry*, 265(2):221–227.

Latif, S. A., Oura, Y., Ebihara, M., Kallemeyn, G. W., Nakahara, H., Yonezawa, C., Matsue, T., and Sawahata, H. (1999). Prompt gamma-ray analysis (PGA) of meteorite samples, with emphasis on the determination of Si. *Journal of Radioanalytical and Nuclear Chemistry*, 239(3):577–580.

Lechner, P., Eckbauer, S., Hartmann, R., Krisch, S., Hauff, D., Richter, R., Soltau, H., Strüder, L., Fiorini, C., Gatti, E., Longoni, A., and Sampietro, M. (1996). Silicon drift detectors for high resolution room temperature X-ray spectroscopy. *Nuclear Instruments and Methods in Physics Research A*, 377:346–351.

Lin, X. (2005). INAA and analysis of Phosphorus. Private communication.

Lindstrom, R. M., Fleming, R., Paul, R. L., and Mackey, E. A. (1992). The k_0 approach in cold-neutron prompt-gamma activation analysis. In *Proceedings of the International k_0 Users Workshop, Astene, Belgium, 1992*, pages 125–128.

Lindstrom, R. M. and Greenberg, R. R. (2001). Accuracy and Uncertainty in Radiochemical Measurements: Learning from Errors in Nuclear Analytical Chemistry. *Journal of Nuclear and Radiochemical Sciences*, 2(1-2):R1–R4.

Mackey, E. A., Gordon, G. E., Lindstrom, R. M., and Anderson, D. L. (1991). Effects of target shape and neutron scattering on element sensitivities for neutron-capture prompt gamma-ray activation analysis. *Analytical Chemistry*, 63(3):288–292.

Mackey, E. A., Gordon, G. E., Lindstrom, R. M., and Anderson, D. L. (1992). Use of spherical targets to minimize effects of neutron scattering by hydrogen in neutron capture prompt gamma-ray activation analysis. *Analytical Chemistry*, 64(20):2366–2371.

Magara, M. and Yonezawa, C. (1998). Decomposition of Prompt Gamma-ray Spectra Including the Doppler-broadned Peak for Boron Determination. *Nuclear Instruments and Methods in Physics Research A*, 411:130–136.

Materna, T. (2001). Pixe_analogue_spectrum: An analogue acquisition software for the pixe installation at ikp. Private communication.

Materna, T. (2002). Pixe_acquisition_spectrum: A digital acquisition software for the pixe installation at ikp. Private communication.

Materna, T. (2004). Simulations with the mcstas program. Private communication.

Matsue, H. and Yonezawa, C. (2000). k_0 Standardization Approach in Neutron-Induced Prompt Gamma-Ray Analysis at JAERI. *Journal of Radioanalytical and Nuclear Chemistry*, 245(1):189–194.

Matsue, H. and Yonezawa, C. (2001). Multielement determination of typical diet reference materials by neutron-induced prompt gamma-ray analysis using k_0 standardization. *Journal of Radioanalytical and Nuclear Chemistry*, 249(1):11–14.

Michaelis, H. V., Ahrens, L. H., and Willis, J. P. (1969). The composition of stony meteorites II. The analytical data and an assessment of their quality. *Earth and Planetary Science Letters*, 5:387–394.

MicroMatter (2002). MicroMatter thin targets. MicroMatter Co., 491 Harborview Lane, P.O.Box 123, Deer Harbor, WA 98243 USA, jheagney micromatter.com.

Molnár, G. L., Firestone, R. B., Révay, Z., Paul, R. L., and Lindstrom, R. M. (2004). *Handbook of Prompt Gamma Activation Analysis with Neutron Beams.* Kluwer Academic Publishers, Netherlands.

Molnár, G. L., Révay, Z., Paul, R. L., and Lindstrom, R. M. (1998). Prompt-gamma activation analysis using the k_0 approach. *Journal of Radioanalytical and Nuclear Chemistry*, 234:21–26.

Mughabghab, S. F., Divadeenam, M., and Holden, N. E., editors (1981). *Neutron Cross Sections Vol. 1: Resonance Parameters and Thermal Cross Sections, Part A: Z = 1-60.* Academic Press (UK), New York, USA.

Mughabghab, S. F., Divadeenam, M., and Holden, N. E., editors (1984). *Neutron Cross Sections Vol. 1: Resonance Parameters and Thermal Cross Sections, Part B: Z = 61-100.* Academic Press (UK), New York, USA.

National Electrostatics Corporation (2004). Pelletron Tutorials. http://www.pelletron.com/tutor.htm.

Ostermann, A. (2004-2005). Mcstas simulations with the new Cold Source parametrization and detailed description of the nl4b neutron beam guide. Private communication.

Oura, T., Ebihara, M., Yoneda, S., and Nakamura, N. (2002). Chemical composition of the Kobe meteorite; Neutron-induced prompt gamma ray analysis study. *Geochemical Journal*, 36:295–307.

Palme, H. (2005). Differences in the elemental concentrations of the inhomogeneous Allende meteorite. Private communication.

Palme, H. and Jones, A. (2003). Solar System Abundances of the Elements. In Holland, H. D. and Turekian, K. K., editors, *Treatise On Geochemistry*, volume 1, book chapter 3. Elsevier, Burlington, USA.

Pappalardo, L., Romano, F. P., Garraffo, S., Sanoit, J. D., Marchetta, C., and Pappalardo, G. (2003). The Improved LNS PIXE-ALPHA Portable System: Archaeometric Applications. *Archaeometry*, 45(2):333–339.

Paul, R. L. (1995). The use of element ratios to eliminate analytical bias in cold neutron prompt gamma-ray activation analysis. *Journal of Radioanalytical and Nuclear Chemistry*, 191(2):245–256.

Paul, R. L. and Mackey, E. A. (1994). Neutron scattering by hydrogen in cold neutron prompt gamma-activation analysis. *Journal of Radioanalytical and Nuclear Chemistry*, 181(2):321–333.

PONTECH (2001). STP100 Stepper Motor Controller. http://www.pontech.com/products/stp100/.

Räisänen, J. (2001). Charged particle-induced γ-ray emission. In Alfassi, Z. B., editor, *Non-destructive Elemental Analysis*, book chapter 8, pages 276–307. Blackwell Science (UK), London, United Kingdom.

Révay, Z. (2004). Complete analysis of the PGAA samples. Private communication.

Révay, Z., Belgya, T., Ember, P. P., and Molnár, G. L. (2001). Recent developments in HYPERMET PC. *Journal of Radioanalytical and Nuclear Chemistry*, 248(2):401–405.

Révay, Z., Belgya, T., Kasztovszky, Z., Weil, J., and Molnár, G. L. (2004). Cold neutron PGAA facility at Budapest. *Nuclear Instruments and Methods in Physics Research B*, 213:385–388.

Révay, Z., Molnár, G. L., Belgya, T., Kasztovszky, Z., and Firestone, R. B. (2000). A new gamma-ray spectrum catalog for PGAA. *Journal of Radioanalytical and Nuclear Chemistry*, 244(2):383–389.

Röntec (2001). Röntec Holding AG: XFlash Series 2001. http://www.rontec.com/en/3/4/1/2.

Rosta, L. (2002). Cold neutron research facility at the Budapest Neutron Centre. *Applied Physics A*, 74:S52–S54.

Sampietro, M. (2005). On-board electronics for X-ray detectors. http://www.elet.polimi.it/upload/sampietr/Ratex/RATEX1.html.

Sano, T., Futuoka, T., Hasenaka, T., Yonezawa, C., Matsue, H., and Sawahata, H. (1999). Accurate and efficient determination of boron content in volcanic rocks by neutron induced prompt gamma-ray analysis. *Journal of Radioanalytical and Nuclear Chemistry*, 239(3):613–617.

Sauerwein, W. and Garbe, S. (2005). Introduction to BNCT. http://www.uni-essen.de/strahlentherapie/bnct/english/introE.html.

Schanzer, C., Böni, P., Filges, U., and Hils, T. (2004). Advanced geometries for ballistic neutron guides. *Nuclear Instruments and Methods in Physics Research A*, 529:63–68.

Stritt, N. (2001). Boron uptake in cells: A study about the kinetics of boron uptake in cells, neutron-induced cell death (apoptosis) and neutron-induced cell cycle arrest. Diploma-Thesis, NDS Medizin Physik ETHZ, Zürich.

Strüder, L., Meidinger, N., Stötter, D., Kemmer, J., Lechner, P., Leutenegger, P., Soltau, H., Eggert, F., Rohde, M., and Schülein, T. (1998). High-Resolution X-ray Spectroscopy Close to Room Temperature. *Microscopy and Microanalysis*, 6(4):622–631.

Sun, G. M., Byun, S. H., and Choi, H. D. (2003). Prompt k_0-factors and relative gamma-emission intensities for the strong non-1/v absorbers ^{113}Cd, ^{149}Sm, ^{151}Eu and ^{155,157}Gd. *Journal of Radioanalytical and Nuclear Chemistry*, 256(3):541–552.

Voltr, J., Král, J., Černý, J., and Švejda, J. (2002). On-demand beam deflection system for PIXE milliprobe. *Nuclear Instruments and Methods in Physics Research B*, 189:62–65.

Warr, N. (2003). A digital acquisition software for the miniball instrument at ikp. Private communication.

Warr, N. (2004). Digital electronics for gamma ray spectroscopy. Technical report, Institut für Kernphysik der Universität zu Köln.

Willendrup, P. K., Lefmann, K., Farhi, E., and Lieutenant, K. (2004). McStas - A neutron ray-trace simulation package. http://neutron.risoe.dk/mcstas.

Williams, A.-M. M., Donlon, D. A., and Siegele, R. (2002). Strontium in 19th century Australian children's teeth. *Nuclear Instruments and Methods in Physics Research B*, 190:453–457.

XIA (2004). User's Manual: Digital Gamma Finder DGF-4C, Version 3.04. http://www.xia.com/Manuals/DGF4C_user304.pdf.

Yanch, J. C., Shortkroff, S., Shefer, R. E., Johnson, S., Binello, E., Gierga, D., Jones, A. G., Young, G., Vivieros, C., Davison, A., and Sledge, C. (1999). Boron Neutron Capture Synovectomy: Treatment of Rheumatoid Arthritis Based on the ^{10}B(n,α)^{7}Li Nuclear Reaction. *Medical Physics*, 26(3):364–375.

Yonezawa, C. and Matsue, H. (2000). Usefulness of prompt gamma-ray analysis with guided neutron beams compared to NAA. *Journal of Radioanalytical and Nuclear Chemistry*, 244(2):373–378.

Ziegler, J. F. (2004). The Stopping and Range of Ions in Matter. http://www.srim.org/.

Acknowledgement

This work would not have been possible without the help of several people. I would like to give my special thanks to:

Prof. Dr. Jan Jolie for his supervision of my PhD work and for his support, fruitful discussions and careful reading of my manuscripts.

Dr. Thomas Materna, for many fruitful discussions on the PIXE and PGAA projects. My thanks to him also for the introduction and help with the analogue and digital electronics and programming in Labview.

Dr. Sébastien Baechler, who helped me with the PGAA experiments at PSI.

Prof. Dr. Herbert Palme for providing the meteorite samples and geological standards and for very interesting discussions about the composition of meteorites.

Dr. Ulrich Herpers for providing meteorite samples.

Prof. Dr. Peter Böni for very interesting and fruitful discussion and suggestions concerning neutron optics and characteristics and neutron beam guides.

I give special gratitude to the members of the PGAA group at BNC in Budapest: Dr. Zsolt Révay, Dr. Zsolt Kasztovszky, Dr. Tamás Belgya, Laszlo Szentmiklosi, Katy Gméling and last but not least to Prof. Gábor Molnár for the support of my PGAA measurements at BNC. I have performed very interesting experiments with them and I have learned a good piece of knowledge about the PGAA technique and its characteristics. Additionally, I would like to thank them all for a very nice time and very friendly atmosphere during my stays in Budapest. Köszi.

I am grateful to Prof. Ing. Jaroslav Král, Ing. Josef Voltr and Dr. Jan Proška – the PIXE group of the Czech Technical University in Prague – for a valuable help and many pieces of advice concerning the PIXE set-up and PIXE samples. I am also indebted for the possibility to take part at a PIXE experiment with them and to gain valuable experience.

My great thanks go to Prof. Dr. Andreas Türler, Dr. habil. Ralph Gilles and Ing. Bernhard Krimmer for their constructive support of the planned PGAA facility at FRM-II.

I want to thank to all members of the IKP, specially to Dr. Irina Stefanescu, Dr. Andreas Schmidt, Dr. Nigel Warr, Dr. George Pascovici, Lothar Steinert, Sandra Christen, Oliver Möller, Dr. Alfred Dewald, Dr. Oskar Zell, Stefan Thiel, Detlef Schieweck and Michael Albers.

Milá maminko a tatínku, moc dobře vím, že bez vaší celoživotní podpory by tato práce těžko mohla vzniknout. Moc si toho vážím a děkuji.

My unceasing thank belongs to my best good friend Jirka Čížek.

Erklärung

Ich versichere, daß ich die von mir vorgelegte Dissertation selbständig angefertigt, die benutzten Quellen und Hilfsmittel vollständig angegeben und die Stellen der Arbeit - einschließlich Tabellen, Karten und Abbildungen -, die anderen Werken im Wortlaut oder dem Sinn nach entnommen sind, in jedem Einzelfall als Entlehnung kenntlich gemacht habe; daß diese Dissertation noch keiner anderen Fakultät oder Universität zur Prüfung vorgelegen hat; daß sie - abgesehen von unten angegebenen Teilpublikationen - noch nicht veröffentlicht worden ist sowie, daß ich eine solche Veröffentlichung vor Abschluß des Promotionsverfahrens nicht vornehmen werde. Die Bestimmungen dieser Promotionsordnung sind mir bekannt. Die von mir vorgelegte Dissertation ist von Prof. Dr. Jan Jolie betreut worden.

Kudějová Petra

Teilpublikationen

Baechler, S., Kudejova, P., Jolie, J., Schenker, J.-L., and Stritt, N. (2002), *Prompt gamma-ray activation analysis for determination of boron in aqueous solutions*, NIM-A, 488:410–418

Baechler, S., Kudejova, P., Jolie, J., and Schenker, J.-L., (2003), *The* k_0*-method in cold-neutron prompt gamma-ray activation analysis*, JRNC, 256(2):239–245

Kudějová, P., Materna, Th., Jolie, J., and Pascovici, G., (2005), *The new PGAA facility at the FRM II, Garching: comparison with the PIXE results obtained at the new IBA setup at Cologne*, XRS, 34(4):350–354

Kudějová, P., Materna, Th., Jolie, J., Türler, A., Wilk, P., Baechler, S., Kasztovszky, Zs., Révay, Zs., and Belgya, T., (2005), *On the construction of a new instrument for cold-neutron prompt gamma-ray activation analysis at the FRM II*, JRNC, 265(2):221–227